Theranostic of rhabdomyosarcoma with functionalized nanoparticles

Sofia Dominguez-Gil

THÈSE POUR OBTENIR LE GRADE DE DOCTEUR
DE L'UNIVERSITÉ DE MONTPELLIER

En Chimie et Physico-Chimie des Matériaux

École doctorale
Sciences Chimie Balard

Unité de recherche
Institut Charles Gerhardt Montpellier UMR 5253

Nanoparticules fonctionnalisées pour la théranostique du rhabdomyosarcome

Présentée par Sofia DOMINGUEZ-GIL

Le 24 septembre 2021

Sous la direction de Frédérique CUNIN et Jean-Olivier DURAND

Emilie GENIN, Maître de conférences, ISM - UMR CNRS 5255 (Talence, France)	Rapporteur
Yannick COFFINIER, Directeur de recherche, IEMN – UMR CNRS 8520 (Lille, France)	Rapporteur
Jochen ROSSLER, Professeur Head of Division of Pediatric Hematology/Oncology University Hospital, (Bern, Switzerland)	Examinateur
Lluis F. MARSAL, Academia Professor, Universitat Rovira i Virgili (Tarragone, Spain)	Examinateur
Magali GARY-BOBO, Chargée de Recherche, IBMM – UMR CNRS 5247 (Montpellier, France)	Examinateur
Véronique ROSILIO, Professeur, Institut Galien Paris-Saclay – UMR CNRS 8612 (Châtenay-Malabry, France)	Président du jury
Frédérique CUNIN, Directrice de recherche, ICGM – UMR CNRS 5253 (Montpellier, France)	Directeur de Thèse
Jean-Olivier DURAND, Directeur de recherche, ICGM – UMR CNRS 5253 (Montpellier, France)	Directeur de Thèse

UNIVERSITÉ DE MONTPELLIER

Summary

Abbreviations

ALL: Acute lymphoblastic leukemia

AML: Acute myeloid leukemia

APTES: (3-Aminopropyl)triethoxysilane

ARMS: Alveolar rhabdomyosarcoma

BC: Bone cancer

BL: Burkitt's lymphoma

BT: Brain tumor

CAM: Chicken chorioallantoic membrane

CI-M6PR: Cation-independent mannose 6-phosphate receptor

CNST: Central nervous system tumor

CTAB: Cetyltrimethylammonium bromide

DLCL: Diffuse large cell lymphoma

DLS: Dynamic Light Scattering

DRX: Doxorubicin

dsRNA: double-stranded RNA

EMRS: Embryonal rhabdomyosarcoma

EPR effect: Enhanced permeability and retention

ES: Ewing sarcoma

fAChR: fetal acetylcholine receptor

FTIR: Fourier transform infrared spectroscopy

GBM: Glioblastoma multiforme

GCT: Germ cell tumors

GD2: Disialoganglioside

HF: Fluorhydric acid

HGBL: High-grade B-cell lymphoma

HT: Hepatic tumor

ICPES: 3-Isocyanopropyltriethoxysilane

KT: Kidney tumor

LC: Liver cancer

MCF-7: Breast cancer cells

MPS: Mononuclear phagocyte system

mRNA: messenger RNA

NB: Neuroblastoma

NHL: Non-Hodgkin's lymphoma

OS: Osteosarcoma

PCI: Photochemical internalization

PDX: patient-derived xenografts

PEG: Polyethylene Glycol

PMOsPOR-NPs: Porphyrin-based organosilica nanoparticles

PS: Photosensitizer

pSiNPs: Porous silicon nanoparticles

RES: Reticuloendothelial system

RISC: RNA-induced silencing complex

RMS: Rhabdomyosarcoma

ROS: Reactive Oxygen Species

RT: Room temperature

siRNA: Small interfering RNA

ST: Solid tumor

STS: Soft tissue sarcomas

TFA: Trifluoroacetic acid

TfRs: Transferrin receptors

THF: Tetrahydrofuran

TPE-PDT: Two-photon excitation photodynamic therapy

WT: Wilms tumor

Introduction

The World Health Organization defines cancer as a "large group of diseases that can start in almost any organ or tissue of the body, being the abnormal and uncontrolled cellular growing their main characteristic. The last stage of the illness is metastasis, when abnormal cells can invade adjoining parts of the body and/or spread to other organs, being the main cause of death".[1] The last available data show around 10 million deaths and almost 20 million new cases in 2020 in the world.[2] According to The Global Cancer Observatory, the number of new cases will be estimated at 28.4 million in 2040.[3]

In this work, we focused our attention on childhood cancer, which is a major cause of infant mortality worldwide. Around 400 000 children and adolescents of 0 – 19 years old are diagnosed with cancer each year in the world.[4] The probability of survival in high-income countries is encouraging, around 80 % of children are cured, but long-term treatment-related effects are observed. Nevertheless, in low and middle-income countries only 15-45% of them survive, therefore it is necessary to continue working to improve these survival rates.[5]

The objective pursued in this thesis work is to develop a more personalized way of treating the RMS. A treatment that responds to the needs of pediatric patients, taking into account the differences between children and adults, and particularly intended to children. In order to do accomplished this goal, we have developed two different and complementary materials, namely porphyrin-based mesoporous organosilica nanoparticles (PMOsPOR-NPs) and porous silicon nanoparticles (pSiNPs). Both materials have been characterized and functionalized with several target molecules to test them *in vitro* on cancer cell lines.

- In chapter 1, we present a literature review about the role of the nanomedicine and the targeted therapies in cancer treatment, more specifically in RMS.

- In chapter 2, we describe the use of PMOsPOR-NPs in the theranostic of rhabdomyosarcoma. The first part of the chapter focuses on the modification of these nanoparticles for their use in active targeting. The TPE imaging as well as their TPE-PDT efficiency was tested *in vitro* on RMS cells and is presented. In the second part, TPE-induced siRNA delivery is presented.

- In chapter 3, we present the synthesis of pSiNPS and their employment in several biological tests. In the first part of the chapter, the functionalization of pSiNPs with a specific peptide capable of targeting membrane receptors of RMS is described. The internalization of these nanoparticles was tested *in vitro* on RMS cells and is presented.

In the second part, the functionalization of pSiNPs with a photosensitizer to enhance their ROS generation, and with a target molecule is detailed. Their efficacy in TPE-PDT on RMS cells is presented. In the last part of the chapter, photo-assisted gene transfection (siRNA) triggered by bi-photonic excitation light was studied.

CHAPTER 1: Nanomedicine for cancer treatment

1. Pediatric cancers

Among pediatric cancers, the most commons types are leukemia (28%), brain and central nervous system tumors (27%), lymphomas (12%), and neuroblastomas (6%).[6] As they represent only 1-2% of total cancers, identification and research in cancer-causing factors is still limited and complicated. Environmental factors do not seem to be the principal cause as it is difficult to link lifestyle-related risk habits such as tobacco, unhealthy diet, and alcohol, overweight or sedentary life with childhood. Some studies have suggested the genetic predisposition; up to 10% of all cancers are caused by heritable mutations, but it is not determining, and usually, these genetic mutations occur randomly.[7-8] Consequently, it is essential to continue exploring this field to elucidate the possible causes.

In this thesis work, the discussion is centered on the rhabdomyosarcoma (RMS), which is a rare case of tumor (4.5 cases per 1 million children) belonging to the pediatric sarcomas.[9] Sarcomas are tumors that develop from bones, e.g. Osteosarcomas and Ewing's sarcomas, connective tissues, or soft tissues where rhabdomyosarcoma is included. Rhabdomyosarcoma develops from normal skeletal muscle tissue and thus can arise in any part of the human body. However, some localizations are more frequent, such as the neck and the head, the groin, the abdomen, the pelvis, and the upper and lower limbs.[10-11]

Despite RMS occurrence seems to be random, it may however be related to familial cancer syndromes such as:

- Li-Fraumeni syndrome (LFS), which is associated with a mutation in the gene p53.[12-13]
- Neurofibromatosis, which affects the development and growth of nerve cells.
- Beckwith-Wiedemann syndrome, which is characterized by a fetal overgrowth and multiple congenital malformations, associates with abnormalities on chromosome 11p15.5.[14-15]

There are two major RMS subtypes according to the histology of the tumors, also considering the molecular characteristics: [9, 16-18]

- Alveolar rhabdomyosarcoma (ARMS, 20-30%), is the most aggressive one, normally giving rise to metastasis or recurrence, and whose preferential localizations are limb area and perineum area. ARMS presents one of two common translocations t(2;13)(q35;q14) or t(1;13)(p36;q14) which induces a gene fusion between PAX3

(chromosome 1) or PAX7 (chromosome 2) and FOXO1a (chromosome 13), respectively. Translation products of these gene fusions lead to the increased expression of several oncogenes and are responsible for the aggressive phenotype of ARMS.[19-20] 60% of patients express PAX3-FOXO1a and have an overall survival of around 61%, but only 20% express PAX7-FOXO1a having an overall survival of 82%. This is why, more research about these genes is crucial to improve medical prognosis in case of more aggressive ARMS, those presenting PAX3-FOXO1a fusion transcription factor.

- Embryonal rhabdomyosarcoma (ERMS, 60-70%) presents a better prognosis and belongs to a more heterogeneous group compared to Alveolar rhabdomyosarcoma (ARMS). It affects children before 5 years old and appears preferentially nearby the head and neck, and in the genitourinary system. This tumor is characterized by a loss of heterozygosity at chromosome 11 in the 15 loci (11p15.5), where the gene coding for IGF-II and the tumor suppressor gene H19 are present. In abnormal conditions, IGF-II expresses a copy of the gene that is usually silenced and H19 becomes inactive. This means an overexpression of IGF-II, and consequently a constant signal of proliferation that is no longer regulated by H19, allowing tumor development.[21]

1.1. Current treatments

The current treatments are surgical resection, chemotherapy, and/or radiotherapy, and they are chosen according to different criteria such as cancer localization, type, and stage or risk group.

1.1.1. Surgery

This is the first step in the treatment of RMS. There are two types of surgery in RMS patients:[22-23]

- Biopsy that is the extraction of sample cells or tissues to confirm the presence of cancer. The biopsy is useful to find out the suitable treatment for the patient.

- Wide local excision, a surgery to remove the tumor and some of the tissue around it. It can be combined with chemotherapy or radiotherapy to ensure the entire tumor removal.

Different criteria must be considered before doing surgery, such as the tumor localization, the tumor answer to the chemotherapy and radiotherapy, and the surgery's effect on the child's body functions and appearance.

1.1.2.Chemotherapy

Chemotherapy consists of the intravenous administration of cytotoxic drugs, allowing them to enter the bloodstream and diffuse throughout the body. Among chemotherapy drugs, the most commonly used are vincristine, ifosfamide, actinomycin D, and/or doxorubicin. More specifically, a multi-drug regime called IVA (isofasfamide, vincristine, and actinomycin D) is the most commonly used in RMS patients.[17]

Chemotherapy is administered in order to:[22-23]

- Destroy residual cancer cells after initial surgery to reduce the risk of cancer recurrence (adjuvant chemotherapy).
- Shrink tumor size to facilitate surgery or radiotherapy (neoadjuvant chemotherapy).
- Relieve pain and control the symptoms of advanced RMS (palliative chemotherapy).

Usually, it is administered in cycles with some days off to allow the patient body to recover. The total length of treatment ranges from 6 months to a year. However, chemotherapeutic drugs can also affect healthy cells, leading to severe side effects.

1.1.3.Radiotherapy

Radiotherapy uses high-energy radiation to damage cancer cells' DNA, stopping cellular division and, provoking cellular death. Unfortunately, this technique is not specific to tumor cells and radiations can also generate important damage on healthy tissues. It can be supplied along with chemotherapy to treat RMS when surgery is not possible (e.g. a tumor that has grown into the skull bones, into the brain itself, or into the spinal cord). It is not usually needed for treating ERMS that can be removed with surgery.[22-23]

The employment of all of these treatments has helped to increase the survival rate of children and adolescents. According to the IRS (Intergroup Rhabdomyosarcoma Study) clinical trials, 5-years overall survival has improved from 55% to 73% for non-metastatic RMS over the last 30 years.[24] On the other hand, only a 20% of survival rate is observed in the case of

RMS in stage 4.[25] Despite these encouraging results in the case of non-metastatic RMS, there are still some challenges concerning current treatments:

- Many RMS survivors experience side effects along with the therapy, e.g. hair loss, nausea and vomiting, mouth sores, fatigue, loss of appetite, and increased chance of infections.
- They can also experience long-term effects that can manifest months to years after finalizing the treatment.[26]

Consequently, therapies must be adapted to minimize short and long-term side effects but also to allow better survival rates especially for more aggressive forms of cancers.

1.2. Clinical needs: developing personalized medicine for RMS

There is an urgent necessity to implement more tailored and innovative treatments for the pediatric population to increase its survival rates, but also to limit the inherent and acquired resistance of cancer cells to chemotherapies, which is a common drawback in RMS treatment.[26] Instead of a direct adjustment of the dose to bodyweight/surface from adults' prescription, the treatments should be adapted to the biological and/or metabolic development of children.[27-28] It is important to highlight how difficult it is to practice clinical trials in children due to different issues in terms of scientific, clinical, ethical, technical, and logistical challenges.[29] This is the main reason for having much fewer therapies approved for children compared to adults. According to the FDA, only 11 drugs have been approved for anticancer therapy in children from 1980 to 2017.[30] The novel therapeutic approaches should be based on targeted therapies. Molecular and genomic studies of ARMS and ERMS would allow specifically identifying target molecules involved in the growth and the proliferation of cancer cells. Receptors tyrosine kinases (RTKs) [31-33], such as ALK, IGF-1, FGFR4, MET, EGFR, and HER2, have been found overexpressed in RMS, and they are involved in the proliferation, differentiation, and survival of RMS cells. In addition, some of them such as ALK, IGF-1, and FGFR4 are direct targets of PAX3-FOXO1a [34-35] which, as mentioned, is a fusion protein involved in the tumorigenesis of RMS and is expressed in 80% of tissues with ARMS but not in the normal tissues, being a potential therapeutic target and biomarker.[36] Single-agent targeted therapies will not be sufficient to reach clinical efficacy. Combination therapy, which uses more than one drug or modality, can boost clinical effectiveness and/or decrease treatment-associated toxicities. In this sense, cancer progression is usually regulated by an ample variety of different processes;

[31, 35] therefore, the strategy that we seek to develop in this work is a triple targeting approach: the use of different nanoparticles combined with targeting molecules and photodynamic therapy (PDT) and/or gene delivery.

2. Nanomedicine & targeted therapies

Nanomedicine is the application of nanotechnology in the field of health, aiming to improve the way of doing medical diagnosis, prevention, and the treatment of different illnesses employing nano-sized tools.[37-38] Currently, nanomedicine is applied in cardiovascular or neurodegenerative diseases, but also for cancer treatment, because it allows overcoming common limitations of therapeutic molecules, such as low specificity, rapid drug clearance and biodegradation, which sometimes require drug administration in large quantities, and/or limit the targeting.[39]

Therefore, the encapsulation of the active ingredient inside a vehicle, in this case, the nanomaterial, makes it possible to deliver the drug in a stable and controlled way in the organ to be treated, crossing biological barriers while protecting the active molecule to deliver in an active form. With this approach, the therapeutic efficacy is expected to be improved, while reducing the doses administered and the side effects of some active ingredients.

2.1. Nanoparticles

Among the different vectors described in the bibliography, this work is focused on the use of nanoparticles for cancer treatment and/or diagnostic (theranostics).

2.1.1. Generalities

According to the IUPAC, nanoparticles are generally defined as materials ranging from 1 to 100 nm. They have unique properties compared to bulk materials such as their nanoscale size, their high surface-to-volume ratio, their possibility of loading and releasing different cargoes, and the opportunity they offer for surface functionalization.[37, 40] Designed at the nanometer scale, some of them also display intrinsic physical properties (magnetism, optical and electronical properties, etc.).

To use these materials as vectors in medical applications, they must meet very precise specifications: [41-42]

- To be stable, biocompatible, and biodegradable.
- To be able to transport a sufficient amount of chemotherapeutic drug without affecting its stability and its activity. They can help in the improvement of solubility of hydrophobic chemotherapeutic drugs such as camptothecin, doxorubicin, and paclitaxel.
- To deliver the chemotherapeutic drug in a stable and controlled way in the area to be treated.
- To be chemically modifiable in order to graft targeting molecules.
- To offer adjustable size and surface charge to allow a prolonged circulation time in the bloodstream, diffusion through the physiological barriers, and subsequent distribution to tissues. Highly anionic particles tend to evade clearance from the circulatory system better than highly cationic particles.

According to several studies, the ideal size is nearby 100 nm. They exhibit increased cellular uptake, due to their ability to bind receptors and effectively induce the membrane-wrapping process. NPs smaller than 5 nm are going to be filtered out by the kidneys, so they leave the systemic circulation very early without being able to reach the tumor, and on the other hand, NPs bigger than 200 nm in size have been shown to accumulate in the liver and spleen.[43-44] Despite these numbers, first attempts using NPs bigger than 200 nm have shown their potential as a promising tool in cancer therapy.[45-46]

The mononuclear phagocyte system (MPS) and reticuloendothelial system (RES) are responsible for nanoparticle elimination from the bloodstream, avoiding their accumulation in the target tissues.[47-48] Surface modification is one strategy to prevent immune system recognition and extend the circulation time, avoiding elimination by MPS and RES. According to the level of surface chemical functionalization, it is possible to distinguish among 1st, 2nd, and 3rd generation nanoparticles (Figure 1).

- 1st generation nanoparticles.

This group includes the nanoparticles, which only encapsulate the active ingredient. They are not surface-modified and have no specific affinity for tumors. The main drawback of 1st generation nanoparticles is that they are recognized by the plasmatic proteins forming a complex. The complex between NPs and plasmatic proteins is likely to be identified as a foreign

body in the bloodstream by the macrophages from the liver, and subsequently, destroyed the nanoparticles, releasing the active ingredient.

- 2nd generation nanoparticles.

These nanoparticles have been developed to evade the opsonization process and to increase the circulation time in the bloodstream. They are usually functionalized with hydrophilic polymers such as polyethylene glycols (PEGs). This strategy prevents opsonin fixation, giving rise to stealth nanoparticles (invisible for MPS), and potentially able to reach the tissues by the enhanced permeability and retention effect (EPR effect).[49-51] The EPR effect will be presented in more details in part 2.1.3.

- 3rd generation nanoparticles.

The second-generation nanoparticles have been improved to recognize specific receptors overexpressed onto tumors, by grafting targeting molecules (sugars, antibodies, peptides, etc.) on their surfaces. This way, 3rd generation nanoparticles can target a specific tumor and deliver a larger amount of active ingredient. This strategy is termed active targeting.

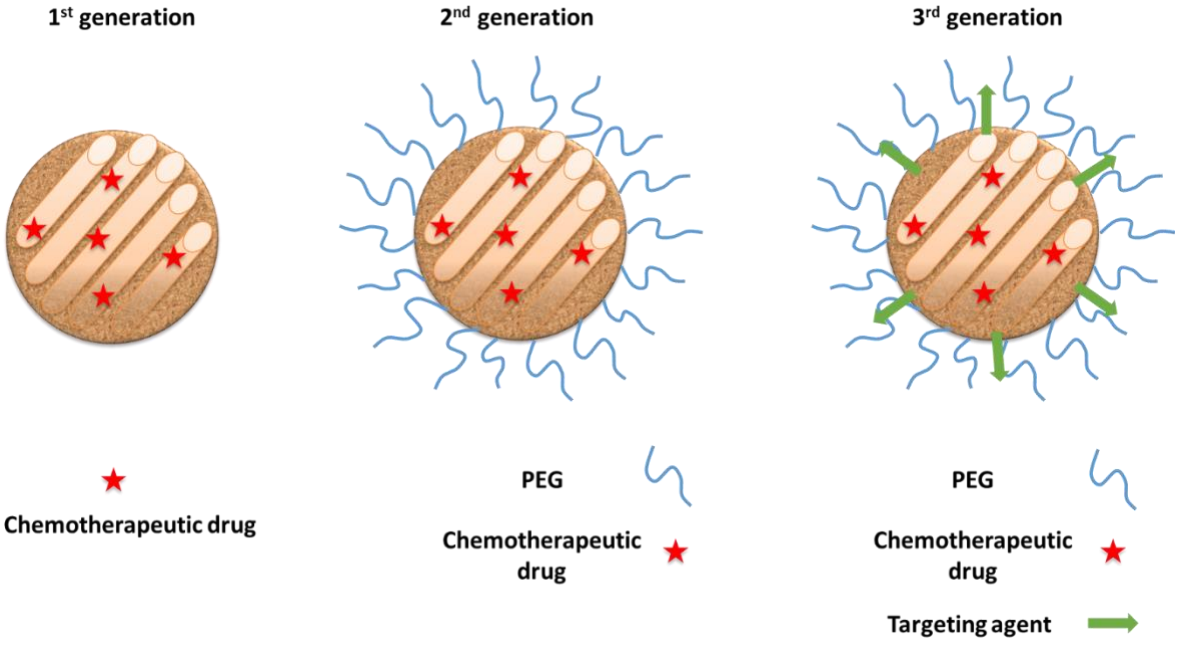

Figure 1. Schematic representation of the three generations of nanoparticles.

2.1.2. Classification

The nanoparticles can be classified into two main groups: organic and inorganic nanoparticles.[52]

2.1.2.1. Organic nanoparticles

- LIPOSOME NANOPARTICLES

Discovered by Alec D. Bangham in 1961, and first published in 1964, they were the first vectors used in medicine, and are still widely employed and developed for clinical applications.[53-54] Liposomes are self-assembling bilayer vesicles made of natural or synthetic phospholipids. Their amphiphilic structure makes it possible to spontaneously form vesicles, with a hydrophilic core and a hydrophobic membrane, in water. Hydrophobic drugs will be encapsulated inside the membrane; while hydrophilic ones will be inside the core.

A PEGylated liposome containing Doxil® (doxorubicin) was the first formulation introduced in the market for the treatment of Kaposi's sarcoma in 1995.[55] This formulation showed reduced cardiotoxicity compared to the conventional one.[56] Nowadays, other lipid vectors have been approved, either by FDA or by EMA, for their use in different types of cancers, such as non-PEGylated liposomal doxorubicin (Myocet®)[57], non-PEGylated liposomal cytarabine (DepoCyt®)[58], vincristine sulfate liposomes (Marqibo®)[59], and liposomal mifamurtide (Mepact®)[60]. Morita and coworkers used doxorubicin-loaded thermo-sensitive liposomes heated with infrared-A radiation, showing inhibition in the growth of the RMS in rats and a reduction in the systemic toxicity.[61] DaunoXome® (Daunorubicin) liposomes combined with hyperthermia (1 h, 43 °C) were investigated by van Bree *et al*. in rats bearing R-1 rhabdomyosarcoma.[62] Not many studies using liposomes for RMS have been reported yet, but scientists continue working on these vectors because they present advantages such as their low systemic toxicity or their biodegradability.[63]

According to the search engine ClinicalTrial.gov, the number of ongoing studies considerably differs between adults and children. Among 364 clinical studies with liposomes, only 10 of them were specially designed for children. A summary of them is collected in Table 1.

Phase	Drug Loaded	Study Start Date	Study Completion Date	Recruitment Status	Last Update Posted	Ages Eligible for Study	Type of Cancer
1	Irinotecan	Dec. 2013	December 2020	Recruiting	18 September 2019	1 year to 20	ST, ES, RMS, NB, OS
1	Doxorubicin	Oct. 2016	October 2021	Recruiting	25 September 2020	Up to 30 years	ST, ES, RMS, STS, NB, OS, WT, HT, GCT
1	Doxorubicin	July 1999	-	Completed	28 April 2015	Up to 21 years	STS, LC, BC, BT, KT
1	Doxorubicin	Dec. 2016	16 March 2019	Withdrawn	19 March 2019	1 year to 40	RMS, NB, ES, OS, CNST
1	Cytarabine	Feb. 1997	-	Unknown	23 March 2010	1 year to 21	Leukemia, Lymphoma,
2	Daunorubicin	13 March 2019	12 May 2027	Suspended	13 February 2020	3 months to 17 years	FLT3-mutated, AML
2	Daunorubicin	6 August 2019	June 2022	Recruiting	24 November 2020	Up to 17 years	ALL, AML
2	Cytarabine	January 2013	December 2019	Recruiting	13 March 2019	3 years to 31	DLCL, BL, HGBL
2	Cytarabine	January 1996	June 2004	Completed	13 March 2019	Up to 20 years	Leukemia, STS, WT, OS,
2	Vincristine	June 2000	September 2005	Completed	31 October 2018	Child, adult, older adult	Lymphoma, Leukemia
2	Vincristine	23 Nov. 2016	11 March 2018	Terminated	3 April 2019	Up to 21 years	ALL, NHL, Leukemia

Table 1. Liposome formulations under clinical trial for pediatric cancer*. Reproduced and adapted from Ref.[40]
*Data collected on December 5th 2020.

- POLYMERIC NANOPARTICLES

It is possible to classify them in natural, as chitosan, alginate, cyclodextrins, albumin, etc., or synthetic ones like poly-glycolic acid (PGA), poly-lactic acid (PLA), poly-lactic-co-glycolic acid (PLGA). Polymeric nanoparticles must fulfill some criteria such as biocompatibility, non-toxicity, and potential biodegradability, and can be presented in different arrangements such as micelles, nanospheres, and/or nanocapsules. Micelles are self-assemblies of amphiphilic molecules, in which the hydrophilic and hydrophobic parts orient according to the medium (aqueous or organic), allowing the load of both hydrophobic and hydrophilic molecules. Nanospheres are solid colloidal nanoparticles in which the drugs are encapsulated inside the polymeric matrix. Nanocapsules are colloidal vesicular systems in which an aqueous or oily core is enveloped by a polymer membrane, the drug will be confined inside the core (Figure 2).[64]

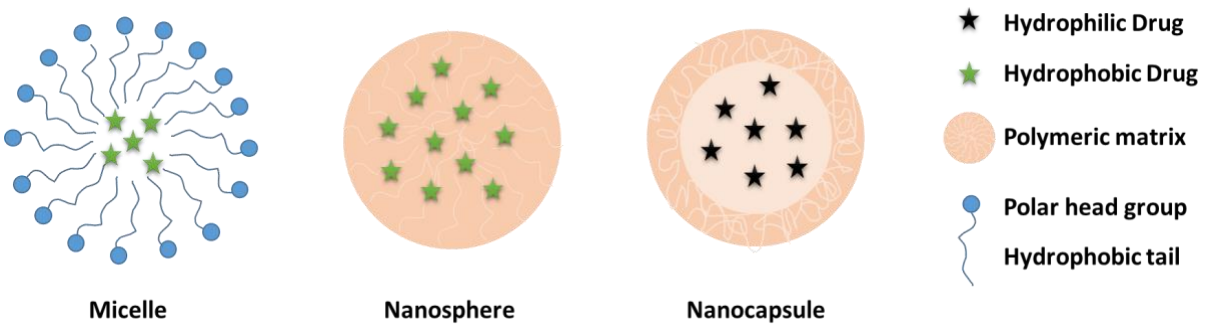

Figure 2. Schematic representation of polymeric nanoparticles (micelles, nanospheres, and nanocapsules).

Abraxane®, albumin-bound paclitaxel, was already approved (2005) for use in adults because it helped to reduce the side effects associated with the conventional drug alone.[65] Currently, it is studied in preclinical pediatric solid tumor models including RMS.[66] Most of the examples found in the bibliography describe chemotherapeutic drugs especially addressed to adult pathologies. Elazar and coworkers described two PLGA-based antisense (AS) formulations, OPN-AS or BSP-AS loaded NPs (osteopontin and bone sialoprotein genes respectively), which were able to reduce tumor bone metastasis incidence and lesion sizes in rats with metastasis.[67] Matsumura *et al*. introduced a micelle consisting of a PEG-poly (aspartic acid)block copolymer conjugated with doxorubicin, showing enhanced pharmacokinetics in humans compared to doxorubicin.[68] In pediatric cancers, Attawia *et al*. showed how the combination of radiation therapy with polymeric microspheres encapsulating Taxol® could reduce the number of remaining sarcomatous cells compared to radiation alone.[69] Schluep *et al*. reported the efficacy of a conjugate of 20(S)-camptothecin with cyclodextrin-based polymer in tumor regression in animals presenting disseminated Ewing sarcoma among other tumors.[70]

- DENDRIMERS

Dendrimers are tree-like branched polymers that can be functionalized with targeting or therapeutic molecules. The most investigated family is the biocompatible, non-immunogenic, water-soluble, and modifiable polyamidoamine (PAMAM) dendrimer.[71] These polymers are synthesized in a shell-by-shell manner, either in a divergent approach, starting from an initiator core, or in a convergent approach, beginning from the periphery, giving rise to well-controlled molecules in terms of size, degree of branching, and dispersity.[72-73] Although the arrival of dendrimers was in the 80s,[74-75] it started to be used in drug delivery in the last decade.[72, 76] Minko and collaborators showed a poly(-propyleneimine tetrahexacontaamine) dendrimer generation 5 (PPIG5) as starting material to condense with siRNA against B-cell lymphoma

(BCL, anti-apoptotic) mRNA.[77] There is still considerable work to do in dendrimers for pediatric cancer, but some examples are found in the bibliography. Alfei and coworkers showed the anticancer activity of GA-dendrimer against neuroblastoma cells. The effectiveness of GA-dendrimer was comparable to this of GA at a concentration almost 100-fold lower than that of GA. This reduction of the dose implied systemic toxicity and side effect diminutions.[78] Kang and colleagues studied the effect of subconjunctival carboplatin-loaded poly(amidoamine) dendrimer of generation 3.5 (PAMAM G3.5) in murine retinoblastoma. Comparing this formulation to the carboplatin in aqueous solution, it was observed an important decrease in the tumor size in the treated eye compared to the contralateral eye.[79]

2.1.2.2. Inorganic nanoparticles

In this section, only organosilica and porous silicon nanoparticles will be described among other inorganic materials such as QDOTs, carbon-based nanostructures, magnetic or metal nanoparticles.

- ORGANOSILICA NANOPARTICLES

Periodic mesoporous organosilica (PMOs) nanoparticles are hybrid frameworks in which functional organic groups are incorporated in the pore walls, either by post-synthesis grafting into the mesoporous silica or by direct co-condensation between the organosilane and the silica precursors.[80-81] This synthetic preparation based on the sol-gel self-assembly reaction, leads to the formation of materials presenting the advantages of both organic and inorganic constituents.[82] The first examples of PMO preparation dated back from 1999 [83-84] and since then, these novel materials have opened the possibility to their application in several and different fields. In biomedical applications, they have received growing attention, due to their high surface areas, improved drug loading capacity, easily chemically modifiable frameworks, excellent biocompatibility [85], and biodegradability.[86-87] Vu *et al*. showed the effectiveness of biodegradable doxorubicin-loaded PMOs (BPMOs) compared to free doxorubicin in human ovarian carcinoma (OVCAR-8) transplanted onto the chicken chorioallantoic membrane (CAM) of fertilized eggs. After the injection of doxorubicin-loaded BPMOs, tumor elimination was observed. In addition, no important damage to various organs present in the chicken embryo was observed, while a widespread organ injury was observed when free doxorubicin was used.[88] Daurat *et al*. described tailored PMO nanoparticles with amine or ammonium silane

precursors constituting their structures. Both nanoparticles were capable of delivering gemcitabine monophosphate (GMP) in MCF-7 cells causing cell death.[89] Mai and colleagues synthesized biodegradable daunorubicin-loaded PMO nanoparticles, containing tetrasulfide bonds, and tested their efficacy in the CAM model. Their use as a vehicle allowed a significant accumulation in the chicken egg model while minimizing the side effects.[90] Rahmani and coworkers designed gold core-shell organosilica NPs from two molecular precursors, bis(triethoxysilylpropyl)tetrasulfide, and bis(triethoxysilyl)ethane and loaded them with gemcitabine monophosphate (GMP). After testing them *in vitro* on MDA-MB-231 cancer cells, these nanoparticles provoked a significant killing effect of 60%.[91]

- POROUS SILICON NANOPARTICLES

Porous silicon nanoparticles (pSiNPs) are silicon nanostructures, with sizes between 50 and 200 nm and high porosity, prepared by a "top-down" synthetic approach. A crystalline silicon wafer is electrochemically etched and mechanically fractured employing sonication [92] or ball milling.[93] pSiNPs present special features such as biocompatibility, biodegradability [94-97], tunable porosity, ability to support cell growth,[98-100] large capacity for cargo load and delivery [101-102], and possibilities for simple chemical functionalization by hydrosilylation and silanisation [103] allowing their use in biomedical applications. Saffie *et al*. developed chlorambucil-loaded pSi microparticles and injected them into mice. The authors showed how chlorambucil loaded into the pSi provoked efficient tumor regression and produced only 10% of animal mortality, while the equivalent amount of free chlorambucil produced 90% and no significant diminution in tumor size.[104] Wang and coworkers showed a multiple drug loading system healthcare, in which pSiNPs were able to chemically conjugated the anticancer drug methotrexate (MTX) and to encapsulate the antiangiogenic drug sorafenib (SFN). *In vitro* experiments on endothelial cells (EA.hy926) and brain tumor cells (U87 MG) demonstrated a decrease in neovascularization, which was attributed to SFN and an inhibition of cell proliferation due to MTX activity after cellular uptake.[105] More recently Landgraf and collaborators prepared camptothecin porous silicon nanoparticles (CPT-pSiNPs), which were tested *in vitro* on MDA-MB-231BO cells to confirm their cytotoxic effect. In addition, this formulation led to a reduction of the orthotopic primary tumor in humanized breast cancer bone metastasis mouse model.[106] Secret and coworkers also used pSiNPs functionalized with cancer cell targeting antibodies to delivery CPT. pSiNPs showed selective killing effect of cells expressing the receptor corresponding to the antibody attached.[107] Correia and coworkers

developed an undecylenic acid-modified thermally hydrocarbonized porous silicon nanoparticles (UnTHCPSi NPs) [108] loaded with sorafenib, and surface-conjugated with heptakis(6-amino-6-deoxy)-βcyclodextrin (HABCD). The HABCD polymer helped to reduce the toxicity of the NPs, increase their stability, enhance the cell-NPs interactions, and sustain the loaded drug release. SFN-loaded UnTHCPSi−HABCD NPs showed efficient inhibition of cell proliferation of the breast cancer cells.[109]

Since the occurrence of nanotechnologies in the 80s, many expectations have been created around the use of nanoparticles in biomedical applications. Most of the examples found in the bibliography are at a laboratory scale, but the translation to the clinic is still limited. Considering the number of patents or publications in the field of cancer therapy, only a few carriers have been placed on the market.[110] Some examples are Doxil® (Doxorubicin; Johnson & Johnson), DaunoXome© (Daunorubicin; Gilead), Mepact© (Muramyl tripeptide; IDM Pharma SAS) Abraxane®, Myocet© (Doxorubicin; Enzon) approved in Europe and Canada [111], and several PEGylated proteins with Zinostatin stimalmer© (SMANCS) [112] approved in Japan. As scientists, we should focus our research on overcoming and understanding the limitations linked to nanomedicine, e.g. the high economic cost of the scale-up, or how the biodistribution in the human body takes place. An approach oriented in the disease rather than the formulation could be a suitable way of working to finally get tangible applications. [44, 113-114]

2.1.3. EPR effect: Passive targeting

The "Enhanced Permeability and Retention effect" (EPR), which was first introduced by Maeda and coworkers in 1986,[115] is defined as the drug-loaded nanocarriers passive entrance and accumulation inside a tumor, minimizing the systemic toxicity associated with conventional treatments.[116] This passive accumulation takes advantage of the abnormal and irregular tumor vasculature, which makes the tumor membrane highly porous and permeable to different chemotherapeutic drugs, and the lack of functional lymphatic drainage, failing in the NPs clearance.[117] A scheme comparing NPs behavior through both types of tissues (normal and malignant) is shown in Figure 3. In the case of normal tissue vasculature, which typically possesses tight interendothelial junctions, the NPs extravasation does not take place; therefore, the nanoparticles will not penetrate the tissue.

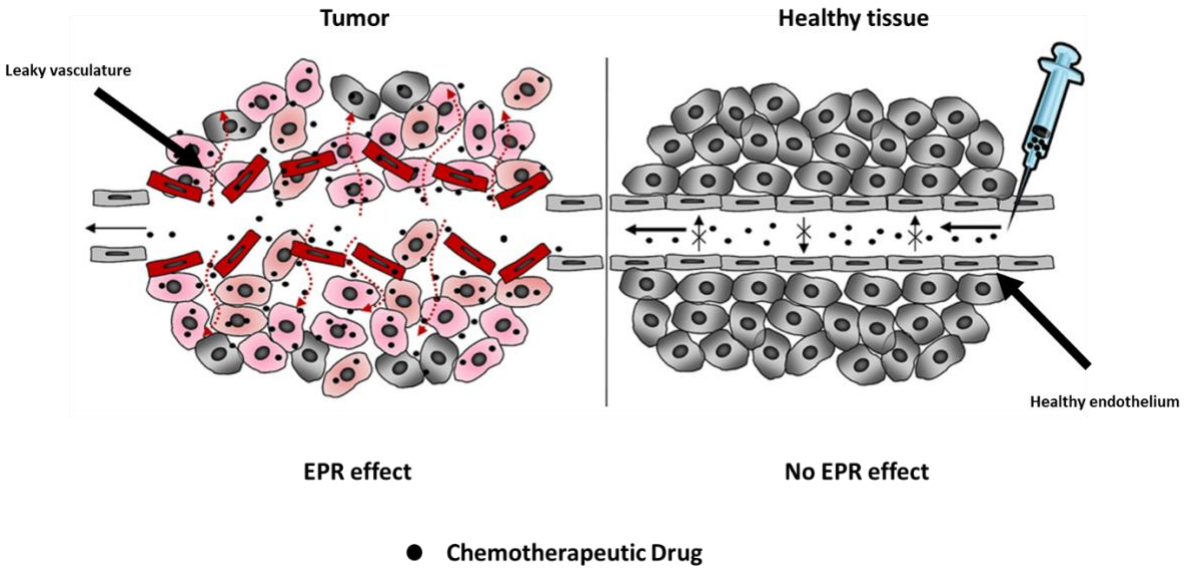

Figure 3. Schematic representation of EPR effect in both tumor and healthy tissue. Reproduced and adapted from Ref.[118]

2.2. Active targeting

The use of passive targeting in cancer treatment presents some limitations. One factor is the significant heterogeneity of the tumors. The cancer cells are not identical, moreover the environment in which cancer starts and develops, is not always the same [119]. Another factor is the lack of control to prevent the accumulation of nanocarriers in other organs with fenestrated endothelium, e.g., the liver and spleen.[120] In addition to these issues, only a small number of nanocarriers reach the tumors according to some preclinical studies.[113, 121-123] Active targeting appears as an option to face these problems.

Active targeting mode, involving molecular recognition, allows a better, faster, and more specific addressing to the cancer cells, preventing the interaction with the healthy cells, and thus a greater NP accumulation into the tumor, i.e. a higher drug accumulation (Figure 4). To guarantee this targeted delivery several criteria are necessary: [124]

- The target must be expressed specifically onto the tumor and not onto healthy tissues.
- The ligand must be chosen to be strongly specific, and have a great affinity for the target cells present in tumors while minimizing binding to healthy cells.
- The density of the ligands needs to be optimized to maintain stealth properties and avoid rapid recognition by the MPS and the RES, but also to ensure an optimal internalization.

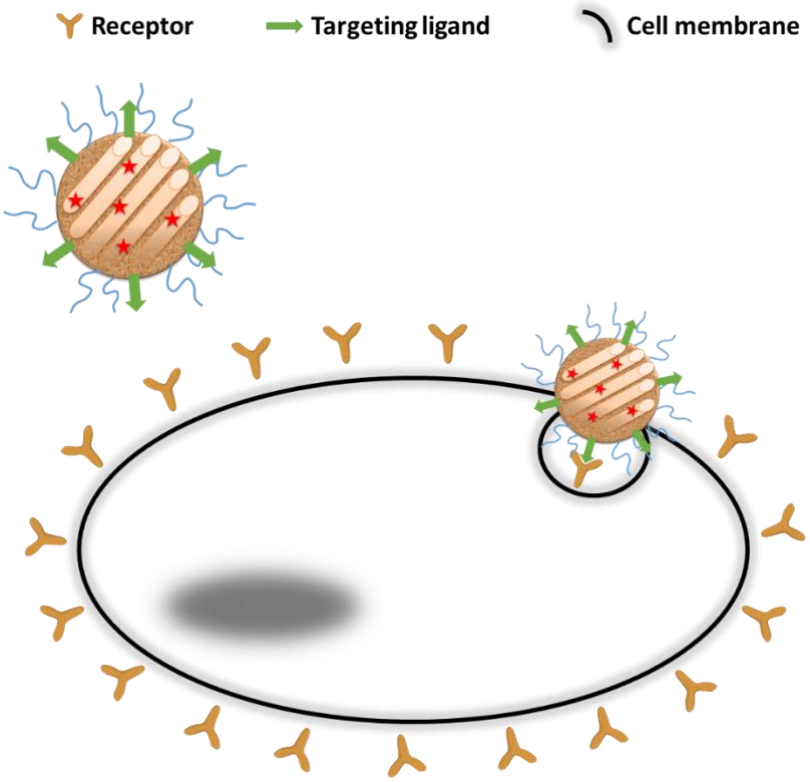

Figure 4. Schematic representation of active targeting mechanism.

2.2.1. Targeting agents

An ample range of ligands has been used for active targeting. Table 2 shows a summary of several types tested against several cancer forms.

Type of targeting ligand	Targeting ligand	Receptors	Type of tumor	Model
Antibodies	VEGF-neutralising antibody	VEGF	RMS	Human A673 RMS mouse tumor model.[125]
	Tuzdal® or Herceptin® (Trastuzumab)	HER2	Breast	
	Mylotarg© (Gemtuzumab ozogamicin)	CD33	AML	
	Anti-CD20, anti-Lym1	CD20 and HLA-DR antigens	NHL	CD-1 mice. [126]
	Cetuximab (boronated EGF)	Epidermal growth factor receptor (EGFR)	Glioma	$F98_{EGFR}$ glioma bearing rats.[127-129]
	Anti-GD2	Disialoganglioside antigen (GD2)	NB	Two murine (nude and SCID-bg) xenograft mice models.[130]

Peptides	Tf or OA-R8	TfRs	Glioma	U87 glioma bearing mice.[131]
	Human H-ferritin (HFn)	TfR1	Glioma	U87MG glioma - bearing mice [132]
	NCAM	CD56	WT	NOD/SCID mice.[133]
	Tf	TfRs	GBM	U87 glioblastoma cell line (*in vitro*).[134]
	Cyclic peptide containing arginine−glycine−aspartic acid sequence (c(RGDyC))	Cell adhesion molecule integrin $\alpha_v\beta_3$	Glioma	U87MG glioblastoma cell line (*in vitro*).[135]
Carbohydrates	hGM	GLUT-1	ES RMS	Mice bearing PDX models. [136]
	Hyaluronic acid	CD44	Liver	HepG2 cancer cells (*in vitro*).[137]
	AMFA	M6CPR	Prostate	LNCaP cancer cells *(in vitro).*[138-140]
	Mannose	M6CPR	Breast Retinoblastoma Colon	MCF-7 cancer cells.[141] MDA-MB-231 cancer cells.[142] Y-79 cancer cells.[143] Mice bearing HCT-116 cells.[144]
Vitamins	Folic acid	Folate	Glioma	Subcutaneous tumor model of nude mice[145]
Proteins	Apolipoprotein A1, anti-CD15	CD15	Medulloblastoma	SmoA1+/+: Math1GFP+/+ SmoA1 MB tumor-bearing mice.[146]
	Epithelial cell adhesion molecule (EpCAM)	EpCAM antigen	Retinoblastoma	Squamous cell carcinoma xenografts in nu/nu mice.[147]

Table 2. Examples of targeting ligands evaluated for the treatment of different cancers. Reproduced and adapted from Ref.[40]

As it can be seen from the table, antibodies are the most commonly used, and nowadays eleven of them are approved for therapy: Rituxan© (CD20; Genentech), Herceptin© (HER2; Genentech/Roche), Campath© (CD52; Genzyme), Zevalin© (CD20; labeled with Y-90; Biogen-Idec), Bexxar© (CD20; labeled with I-131; Coriza/GlaxoSmithKline), Erbitux© (EGFR; Imclone/Lilly), Avastin© (VEGF; Genentech/ Roche), Vectibix© (EGFR; Amgen),

Arzerra© (CD20; Genmab), Yervoy© (CTLA-4; Bristol-Myers Squibb), Adcetris© (CD30; Seattle Genetics) with Mylotarg© (CD33; labeled with calicheamicin; Wyeth/Pfizer) withdrawn from the market in 2010.[148]

According to the way they act against tumors, it is possible to separate antibodies into two types:

- Antibodies that act against cellular growth by blocking a growth factor receptor such as Tuzdal© and Herceptin© (Trastuzumab)[149], which targets overexpression of the HER2 receptor in breast cancer cells. Another example is Erbitux© (Cetuximab), which is an EGFR inhibitor, used for the treatment of metastatic colorectal cancer.

- Antibodies that can be combined with therapeutic molecules, such as Mylotarg© (Gemtuzumab ozogamicin), which is a monoclonal antibody directed against the CD33 receptor, overexpressed in acute myeloid leukemia. The cytotoxic drug is released into the cell to induce double-strand DNA break and subsequently cell death.[150] Kin Man Au *et al*. developed NPs loaded with the PI3K/mTOR inhibitor BEZ235 and conjugated with anti-CD20 and anti-Lym1 antibodies, allowing a specific target of non-Hodgkin lymphoma. Antibody conjugation effectively raised the number of NPs retained on target tumor cells and strengthened the anti-tumor activity of BEZ235 *in vitro* as well as *in vivo* models.[126] Zeisberger *et al*. developed clodronate-loaded liposomes conjugated with VEGF antibody and tested this formulation in a human A673 RMS mouse tumor model. Preliminary studies showed their effective inhibitory activity, resulting in a promising formulation for future targeted therapies.[125]

Wu and coworkers showed the efficacy of a folacin-modified poly(e-caprolactone) micelle to deliver luteolin. The conjugation with folic acid allows the binding to the folate receptor, which is overexpressed in many tumors such as glioblastoma. This strategy showed significantly higher cell inhibition and increased apoptosis of GL261 glioma cells compared to free luteolin.[145] Zaritski and colleagues used a hydrolyzed galactomannan (hGM)-based amphiphilic nanoparticle for selective intratumoral accumulation in pediatric sarcomas such as RMS and ES. Employing fluorescence confocal microscopy and imaging flow cytometry, it was observed that the NPs can target glucose transporter-1 (GLUT-1), which is overexpressed in RMS and ES tumors, showing the potential of this new type of NPs.[136] Xu *et al*. developed

a one-pot synthesis of Dox-loaded organosilica NPs, followed by modification with hyaluronic acid (HA). The authors observed that the Si-Dox@HA NPs present improved uptake by HepG2 cancer cells (overexpressing CD44 receptors) than normal NIH 3T3 cells (low CD44 expression), resulting in a better selectivity and increased cytotoxicity of Si-Dox@HA NPs towards HepG2 cancer cells. In addition, Si-Dox@HA NPs were also suitable for targeted fluorescence imaging of CD44-overexpressing cancer cells.[137]

2.2.2. Peptide targeting and analogs for RM6P-CI targeting

The use of targeting ligands in the treatment of RMS is still scarce. Recently, one preclinical study showed the inhibitory activity of AZD1775 in combination with vincristine and irinotecan, against Wee1 kinase (involved in cell cycle regulation).[151] Another example includes the inhibition of the Receptor Tyrosine Kinases (RTKs). RTK small molecule inhibitors, monoclonal antibodies against RTK ligands, and monoclonal antibodies against RTKs have followed phase I and phase II trials since the year 2000.[33] Roessler and coworkers developed RGD-liposomes loaded with tubulin binding agent epothilone B, showing inhibition of endothelial and tumor cell viability in a lower dose of epothilone B compared to the use of the free the drug.[152] In this thesis work, we use a peptide and a carbohydrate, for specifically targeting two receptors overexpressed onto RMS tumors.

- γ-SUBUNIT OF THE FETAL ACETYLCHOLINE RECEPTOR

The fetal acetylcholine receptor (fAChR) of muscles is a transmembrane protein with subunit composition ααβδγ. Their expression is restricted to thymic myoid cells, extraocular muscles, and denervated striated muscles. The fAChR, more specifically the γ-subunit, is the first receptor shown to be overexpressed on both ERMS and ARMS, but non-expressed on non-rhabdomyomatous tumors nor normal muscle, making it a diagnostic marker for RMS patients and avoiding the risk of side effects by cross-reactivity with normal tissues. [153-155]

Teichert and coworkers have described a novel conotoxin from the venom of *Conus obscurus*. This peptide (αA-conotoxin OIVB), whose sequence is CCGVONAACPOCVCNKTCG, has shown the capacity of inhibiting the mammalian fAChR ($\alpha_1\alpha_1\beta_1\delta\gamma$-subunits). On the other hand, it has shown a lower affinity for the adult muscle AChR and no inhibitory activity on several neuronal AchR subtypes.[156] Therefore, the use of αA-conotoxin OIVB could be a promising tool for the theranostic of RMS.

The target of this receptor employing pSiNPs decorated with αA-conotoxin OIVB is presented in Chapter 3.

- (CI) MANNOSE- 6 PHOSPHATE RECEPTOR

The cation-independent mannose 6-phosphate receptor belongs to the type I transmembrane glycoprotein family. It is responsible for the intracellular transport of newly synthesized lysosomal enzymes between the *trans*-Golgi network and the endosomes, to transfer them to the lysosomes afterward. In addition, it is in charge of the endocytosis of molecules bearing the mannose-6-phosphate signal,[157-159] because the CI-MPR extracytoplasmic domain contains two distinct M6P-binding sites.[160] The ability of this receptor to interact with several growth factors such as IGF-II and TGFβ1 is well known, being able to act against the cellular proliferation,[159] but in this case, their function as a therapeutic target will be investigated.[161] In the bibliography, it has been shown examples of the overexpression of CI-M6PR in different cancers such as breast,[141-142, 162-163] prostate,[138-140] retinoblastoma,[143] or colon[144]. A laboratory study performed by Vaillant and coworkers has shown the overexpression of the CI-M6PR in prostate cancer compared to normal cell lines. They employed mesoporous silica nanoparticles (MSN) functionalized with a new carbohydrate derivative, an analog of mannose-6-phosphate, to specifically target this receptor. The MSNs were used in PDT and they showed better efficacy than non-targeted NPs.

The application of functionalized porphyrin-based periodic mesoporous organosilica nanoparticles (PMOsPOR-NPs) for actively targeting the CI-M6PR in solid tumors such as RMS is presented in chapter 2.

2.3. Photodynamic therapy & Gene therapy

2.3.1. Photodynamic therapy generalities

Photodynamic therapy (PDT) is a well-recognized non-invasive treatment using molecules (photosensitizers) activated by light to produce specific biological effects in cells or tissues. [164] Initial attempts were performed in the early 20th century when Von Tappeiner and Albert Jesionek first reported their clinical uses in 1903. Eosin was applied locally to a tumor on the lip and exposed to light.[165-166] This modern era, which corresponds with the discovery of the hematoporphyrin derivative (HpD), starts in the 50th/60th. This period led to several

preclinical and clinical studies to finally get the first government approval in 1993 with a purified version of HpD (Photofrin®).[164, 167-169] Nowadays, PDT is approved not only for the treatment of solid tumors and precancerous conditions but also for non-oncological applications. This innovative technique has shown its effectiveness in killing microbial cells (bacteria, fungi, and viruses),[170-171] in cancer therapy,[172-173] in ophthalmology,[174] and in dermatology.[175-176] In cancer treatment, some of its advantages over surgery, chemo, or radiotherapy are the spatial and temporal control, negligible toxicity to healthy tissue, and the lack of intrinsic or acquired resistance mechanisms.[177]

Concerning the basis of PDT, there are three essential elements to perform it: [178-180]

- A photosensitizer (PS).
- A light source
- The reactive oxygen species (ROS) generated by the PS when it is activated by the light source.

2.3.2. Photophysical mechanism

After the light absorption, the PS is excited from its ground state (singlet state S_0) into a relatively long-lived electronically excited state (triplet state T_1) *via* a short-lived excited singlet state (S_1) by a process termed "intersystem crossing". The triplet state can undergo two kinds of reactions, which are schematized in Figure 5 (type I and II mechanism). In the type I mechanism, the triplet state can react directly with a substrate and form radicals, such as hydroxyl radicals (•OH) and superoxide (O^{2-}) ions. Successively, these radicals interact with the oxygen to produce oxygenated species. In the type II mechanism, the triplet state can transfer its energy directly to molecular oxygen to form singlet oxygen $^1O_2$, a highly cytotoxic Reactive Oxygen Species (ROS). [181-183]

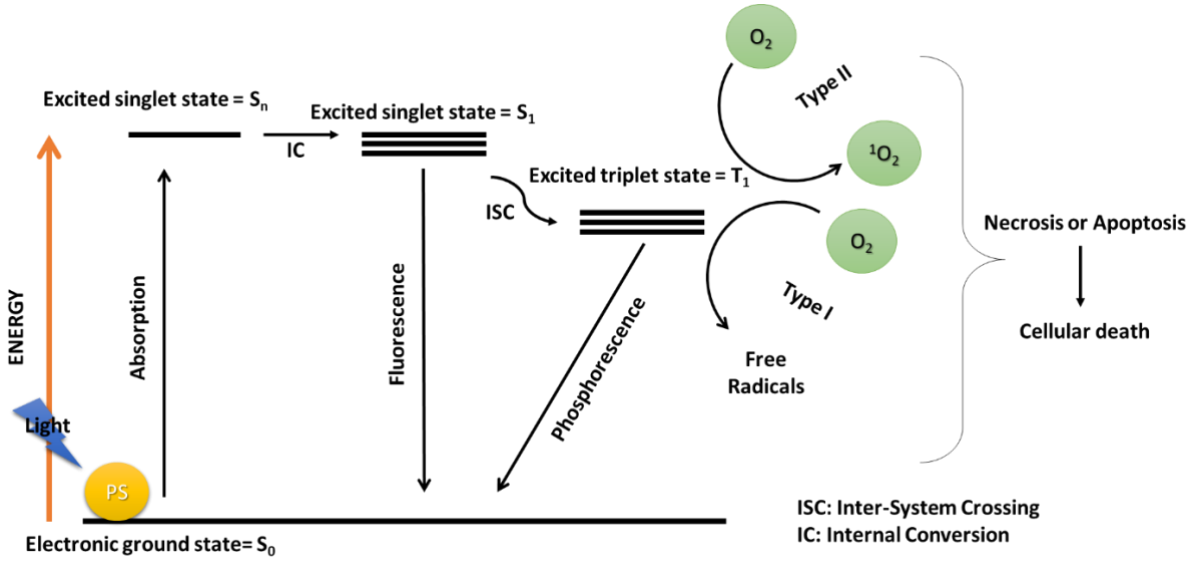

Figure 5. Jablonski diagram applied to PDT.

ROS will destroy tumors following different mechanisms; it may be possible to provoke the oxidation of different molecules (amino acids, nucleic bases, lipids…) in the cells, inducing the destruction of the organelles and the plasma membrane and leading to cell death by necrosis. In addition, singlet oxygen can induce the release of cytochrome C in the mitochondria, which is responsible for the apoptosis mechanism. Another option is to damage tumor-associated vasculature, which shuts down the tumor oxygen supply (hypoxia) and the nutrients supply, or to trigger an immune response against tumor cells.[184-185]

Under appropriate excitation the PS transfer its energy to the surrounding molecular oxygen in its singlet state (which then converts to triplet state). It must fulfill some specific criteria:[186]

- Preferential accumulation in diseased tissue/targeted tissue over healthy ones.
- Generation of cytotoxic species ($^3O_2$, O_3, etc.) which conduct to cell death.
- Strong absorption with a high extinction coefficient in the red/near-infrared spectrum (600–850 nm), which allows deeper tissue penetration.
- Low dark toxicity and negligible cytotoxicity.
- Rapid clearance from the body post-procedure.
- High chemical stability and photostability.
- Biocompatibility and solubility in biological media to effectively carry them through the bloodstream to the target site.
- Low photobleaching to prevent its degradation and maintain the effectiveness during treatment.

- Natural fluorescence to ease monitoring its biodistribution by imaging.

Currently, just a few PS have been approved to be used in clinical applications. They are summarized in Table 3.

PS	Trade name	Cancer	Wavelength/nm	Current Status
Hematoporphyrin derivative	Photofrin®	Lung, esophagus, bile duct, bladder, brain, ovarian, breast skin metastases	630	Canada, 1993 Japan, 1994 USA, 1995
Aminolevulinic acid	Levulan®	Skin, bladder, brain, esophagus	417	USA, 1999
Methyl aminolevulinate	Metvixia®	Actinic keratosis, basal cell carcinoma, non-melanoma skin cancer	630	USA, 2004 EU, 2001 New Zealand, 2002 Australia, 2003
Hexylaminolevulinate	Hexvix®	Bladder	White light	Sweden, 2004 EU, 2006 US, 2010
Verteporfin/benzoporphyrin derivative monoacid (liposomal formulation)	Visudyne®	Pancreas, breast	690	USA, 2000 Canada, 2000 EU, 2000 Japan, 2003
Palladium bactereopheophorbide, padeliporfin	Tookad®	Esophagus, prostate	762	MEX, 2015
Temeporfin/m-THPC	Foscan®	Head and neck, lung, brain, bile duct, pancreas skin, breast	652	EU, 2001
Talaporfin/Mono-L-aspartyl chlorin e6	Laserphyrin®	Lung, liver, colon, brain, breast skin metastases	664	Japan, 2004
2-(1-hexyloxyethyl)-2-devinyl pyropheophorbide-a	Photochlor®	Head and neck, esophagus, lung	665	NCT02119728 Clinical trail
Tin ethyl etiopurpurin I	Purlytin®	Skin, breast	660	NCT00002167 Clinical trail
Disulfonated tetraphenyl chlorin	Amphinex®	Superficial cancer, colon	633	NCT00993512 Clinical trail
Motexafin lutetium	Lutex®	Breast	732	NCT00005067 Clinical trial
Sulfonated aluminum phthalocyanine	Photosens®	Various cancers	675	Russia, 2001

Table 3. Current photosensitizers approved or in clinical trial for cancer treatment. Adapted and Reproduced from Refs.[187-188]

These commercial examples are principally applied to adult cancer, but in the bibliography, several studies using PS for pediatrics have been reported. Fakhar-e-Alam and coworkers showed the photodynamic effects of PHOTOGEM® on the RMS cell line. The viability of human muscle carcinoma RMS cells was of 25% when the cells were incubated with PHOTOGEM® and irradiated with a He-Ne laser, presenting a promising therapy for the

treatment of muscular tumors.[189] Ocker *et al.* developed an *in vitro* study in which they used Hypericin and derivatives (^{131}I-HYP) combined with PDT for the treatment of alveolar RMS cells.[190] Atif *et al.* showed the cytotoxic effects produced by Photofrin® combined with laser irradiation to human RMS cancer cells. A loss of 82% in cell viability was generated by ROS species produced after irradiating the PS.[191]

Most applications of PDT treatments involve one-photon excitation (OPE) lasers, but this modality presents several limitations such as low photosensitizing efficiencies, tumor resistance, lack of spatial resolution, and poor penetration into living tissues, restraining PDT treatments to superficial cancers.[178] Two-photon excitation (TPE) modality emerges as a good candidate to overcome all these problems.

2.3.3. Two photon-excited photodynamic therapy

The TPE-PDT process is based on the absorption of two photons of the same energy (or not) by the photosensitizer. This absorption produces energy equal to the sum of the energies of the two photons. [178, 192] The PS are photoactivated by short laser pulses (femtosecond) at low power and in the near-infrared. TPE allows a deeper tissue penetration (up to 2 cm), a better 3D resolution, and reduced photo-damage to surrounding tumor tissue. In TPE, the irradiation is limited at the focal point of the laser (resolution of the order of µm), whereas in one-photon excitation, the irradiation takes place all along the path of the laser (Figure 6).

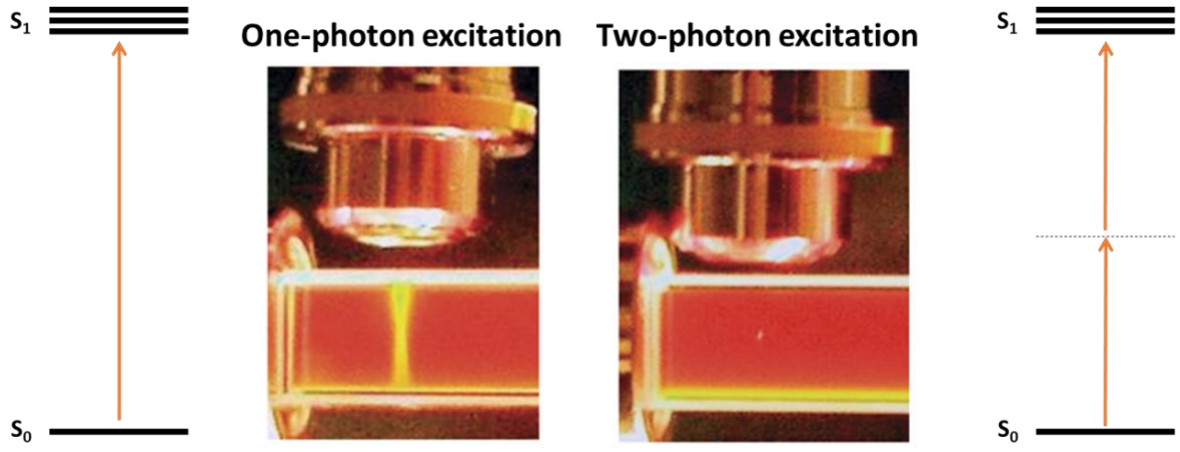

Figure 6. Comparison between OPE-PDT and TPE-PDT. Reproduced and adapted from Ref [193].

The use of the TPE-PDT in the clinic is currently limited to small solid tumors, which must be accessible by light irradiation (skin tumors) or accessible endoscopically[194]. TPE-PDT has been studied with nanoparticles and the topic has been compressively reviewed.[185]

2.3.4. Gene therapy generalities

Currently, gene therapy is being applied for a varied range of illnesses, such as cancer, peripheral vascular diseases, arthritis, neurodegenerative disorders, and acquired immunodeficiency syndrome (AIDS), but at the beginning, this new therapy was essentially applied to genetic diseases. [195] The first officially approved clinical protocol to introduce a foreign gene into humans was approved by the Recombinant DNA Advisory Committee (RAC) in December 1988.[196] In this study, Rosenberg *et al*. used gene marking to track the movements of tumor-infiltrating blood cells in a cancer patient.[197] Michael R. Blaese was the first to conduct a trial using a therapeutic gene. On September 14 of 1990, the FDA approved for the first time a gene therapy trial in humans. Two kids suffering from adenosine deaminase deficiency (ADA-SCID) were treated with white blood cells modified *ex vivo* to express the normal gene responsible for adenosine deaminase production. [198] At the moment, close to 60% of all ongoing clinical gene therapy trials worldwide are developed for cancer treatment, leading to patents and/or clinical trials for new therapeutic formulations (see: http://www.freepatentsonline.com http://www.delphion.com/ and http://clinicaltrials.gov/ct2/home).[196, 199]

This therapeutic strategy involves the transference of nucleic acids (DNA or RNA), using a vector, to the appropriate cellular target to help in the treatment of a genetic or a medical disorder. Two ways of acting are possible; the delivered gene can either correct damaging consequences of specific gene mutations or re-program cell functions to overcome a disease. In any case, for the success of the therapy, the exogenous gene has to be efficiently, precisely, and stably introduced into the target cell. [200-201]

2.3.5. Viral vectors & non-viral vectors in gene therapy

Two carriers are developed for the transference of the genetic material. On one hand, it is possible to use viral vectors such as herpes virus, adenovirus, retrovirus, adeno-associated virus, and more recently lentivirus. [200] On the other hand, non-viral vectors such as cationic lipids, liposomes, cationic polymers, or inorganic nanoparticles are used.

The principal advantage of viral vectors (about 75% of the protocols) is their transfection efficiency; in contrast, they have some limitations in the insert's size, production, and immunogenicity. Non-viral vectors are less efficient in transfection but there are no

limitations in terms of insert size, they are less immunogenic and easier to manufacture.[202] Table 4 shows a summary of gene-transfer vectors with their advantages and disadvantages.

Vector	Advantages	Limitations
Retrovirus	- Easy to prepare - Well characterized - Currently in clinical trials - Stable expression - High capacity for insertion of foreign DNA fragments (8Kb)	- Can only infect diving cells - Low capacity for insertion of foreign DNA fragments - Risk of replication - Random integration into host genome
Lentivirus	- Can infect nondiving cells - Low immunogenicity - High capacity for insertion of foreign DNA fragments (8Kb)	- Not very well studied - Low capacity for insertion of foreign DNA fragments - Insertional mutagenesis - Random integration into host genome
Adenovirus	- High capacity for insertion of foreign DNA fragments (7 – 10 Kb) - Can infect nondiving cells - Infection in most cell types - Efficient transfer	- High immunogenicity - Limited duration of *in vivo* gene expression - Risk of replication - Limited repeat administration
Herpes virus	- High capacity for insertion of foreign DNA fragments (25 Kb) -Wide host range	- High immunogenicity - Limited duration of *in vivo* gene expression
Adeno-associated virus	- No viral gene expression - Can infect nondiving cells - Low immunogenicity - Long term gene expression - Nonpathogenic - Currently in clinical trials	- Low capacity for insertion of foreign DNA fragments (8Kb) - Tedious to prepare large quantities - Reduced efficacy of repeat administration
Naked DNA	- Manufacturing, storage, quality control are simple and cheap - Very low immunogenicity - Clinical efficacy demonstrated in critical limb ischemia - Very good safety profile	- Very short duration of expression in most tissues - Very inefficient transfection *ex vivo* and *in vivo* - Retargeting transfection very difficult
Cationic lipids	- Relatively simple manufacturing, storage, quality control - Low immunogenicity - Efficient transfection *ex vivo* - Good safety profile	- Inefficient transfection *in vivo* - Very short duration of expression - Little clinical experience - Retargeting transfection difficult
Cationic polymers	- Relatively simple manufacturing, storage, quality control - Low immunogenicity - Efficient transfection *ex vivo* - Good safety profile - Retargeted transfection demonstrated	- Inefficient transfection *in vivo* - Very short duration of expression - No clinical experience
Inorganic nanoparticles	- Easy production - Surface functionalization - Short time of transfection - Wide availability - High transfection efficiency - Potential capability for targeted delivery and controlled release	- Most of them are instable, toxic and non-biocompatible

Table 4. Advantages and limitations of the main gene-transfers vectors. Reproduced and adapted from Refs. 199, 202-203

Rengaswamy and coworkers showed the use of liposome protamine particles (LRP) carrying siRNA and conjugated with cyclic RGD (arginine-glycine-aspartate) peptide to target ARMS. This vector was able to target the overexpressed αVβ3 integrin receptor leading to the downregulation of the PAX3-FOXO1 in ARMS cells.[204] Schiffelers *et al*. developed PEGylated-PEI NPs functionalized with RGD peptide for the delivery of siRNA sequences. The vector was intravenously administrated into neuroblastoma N2A tumor-bearing mice leading to a selective tumor uptake, inhibition of VEGFR-2 expression, and inhibition of both tumor angiogenesis and growth rate. [205] Toub *et al*. loaded a siRNA into poly-isobutyl cyanoacrylate aqueous core nanocapsules to block the expression of the Ewing Sarcoma-Fli1 fusion gene. The injection of this formulation into mice xenografted EWS-Fli1-expressing tumor showed both inhibitions of tumor growth and the EWS-Fli1 fusion gene.[206] Di Paolo and colleagues prepared anti-GD2 NPs encapsulation ALK-directed siRNA. These NPs were precisely and efficiently delivered to GD2-expressing NB cells. After injection of the formulation in NB xenografts, the ALK knockdown was observed, resulting in significant inhibition of xenografted tumor growth *in vivo*.[207]

Although, this new therapy has achieved some improvements in terms of antitumor effects, only a few delivery systems have been approved by the medical regulatory agencies and are in clinical trials for cancer therapy, so there is still work to do to overcome the limitations of gene therapy. The reduction of the toxicity and immunogenicity of viral vectors, the increase of the transduction efficiency in the case of the non-viral vectors, or the reduction of the toxic effects associated with the use of retrovirus for gene transfer in humans, are some of the drawbacks that researchers have to confront.

CHAPTER 2: PMOsPOR-NPs as a platform for cancer theranostics

Personalized medicine in cancer treatment is an interesting strategy, whose purpose is to treat tumors in a more tailored manner. Not only to be selective with the type of cancer but also with the patient. Targeted therapies are directed against a specific step in the development of the tumor (using monoclonal antibodies, or tyrosine kinase inhibitors) or against a specific tumor. By targeting specific markers present in tumor membranes, afterward, it will be possible to induce cellular death by different mechanism:

- Drug delivery, for cytotoxic chemotherapy, which aims to block cells division.
- Delivery of photosensitizers, for photodynamic therapy (under one or two photon excitation), which generates Reactive oxygen species (ROS) and singlet oxygen that are cytotoxic.
- Delivery of genes, which induces the activation or deactivation of the expression of a gene, for therapeutic purposes.

The final aim of this new trend is to limit the side effects provoked by traditional treatments and to ensure a better quality of life for patients.

The objective of this chapter is to describe the use of Porphyrin-based organosilica nanoparticles (PMOsPOR-NPs) as a platform for cancer theranostics. The particular structure of these nanoparticles, with a large mesoporosity (5-80 nm) and a framework consisting of J aggregates of porphyrins, allows their loading with different cargoes and also their use in two-photon excitation (TPE).

- The first part of the chapter describes the functionalization of PMOsPOR NPs with an analog of mannose-6 phosphate, capable of targeting a membrane receptor (RM6P-CI) of RMS. The TPE imaging as well as their TPE-PDT efficiency on RMS cells is presented.

- In the second part, TPE-induced siRNA delivery is studied and presented. (3-Aminopropyl)triethoxysilane is grafted onto PMO−PEG−AMFA and transfection efficiency is studied on MCF-7-luc cells.

Part I. The mannose 6-phosphate receptor targeted with porphyrin-based periodic mesoporous organosilica nanoparticles for rhabdomyosarcoma theranostics

Abstract

Porphyrin-based periodic mesoporous organosilica nanoparticles (PMO) synthesized from a large functional octatriethoxysilylated porphyrin precursor and allowing two-photon excitation photodynamic therapy (TPE-PDT) and NIR imaging were synthesized. These PMO were grafted with polyethylene glycol (PEG) moieties and an analog of mannose 6-phosphate functionalized at the anomeric position (AMFA). AMFAs are known to efficiently target mannose 6-phosphate receptors (M6PRs) which are overexpressed in various cancers. Here, we demonstrated for the first time that M6PRs were over-expressed in rhabdomyosarcoma (RMS) cells and could be efficiently targeted with PMO–AMFA allowing TPE imaging and TPE-PDT of RMS cells. The comparison with healthy myoblasts demonstrated an absence of biological effects, suggesting a cancer cell specificity in the biomedical action observed.

Interdisciplinary collaboration

Nanomaterial synthesis, physic-chemical characterizations: S. Dominguez Gil, C. Nguyen, C. Charnay, L. Raehm, J-O. Durand, F. Cunin.

Synthesis of porphyrin photosensitizer: V. Chaleix, V. Sol

Synthesis of M6P-PhSq: K. El Cheikh, A. Morère

Cell studies: M. Daurat, M. Gary-Bobo, M. Garcia.

Proteomic Analysis: M. Bernasconi, A. Timpanaro, J. Roessler

- *Biomater. Sci*., 2020, 8, 3678

Introduction

Rhabdomyosarcomas (RMSs) are the most common soft tissue sarcomas in childhood. There are two major subtypes, the embryonal and the alveolar (the most aggressive) RMS. Despite intensified multimodality treatments, the overall survival of high-risk populations has remained at 5% to 20% over the last few decades. This rate is insufficient, and therefore innovative treatments based on nanomedicine are urgently needed. Very few examples of nanoparticles for the treatment of RMS have been described in the literature. Abraxane and liposomal vincristine have been investigated in RMS-xenografted mice,[66, 208] magnetic drug targeting was reported in rat models of RMS,[209] and chitosan nanoparticles have been used to silence TGFβ1 (transforming growth factor β1) in cells with small hairpin RNA.[210] Mesoporous silica nanoparticles functionalized with polyethyleneimine have also been used in cells to silence ELMO1, a protein involved in cell migration.[211] None of these nanoparticles was functionalized with a biomolecule to target RMS. Targeting an overexpressed receptor in cancer research is very important to differentiate between malignant and normal tissues. Gold nanoparticles have been functionalized with a TAT peptide to target RMS cells, and induce cell death[212] but the TAT peptide is not specific for RMS. Liposomes loaded with the tubulin binding epothilone B agent were developed in order to target RMS. These liposomes have been shown to inhibit endothelial and tumor cell viability to the same extent as the free drug. Furthermore, potent antitumor growth activity could be demonstrated *in vivo* by using vascular endothelial cell targeting. Indeed, the RGD peptide was attached on the surface of the liposomes. These liposomes interact with the integrin receptor and show a beneficial effect in comparison to the untargeted formulation, by increasing the cumulative survival of mice bearing RMS.[204] However, the RGD peptide is not sufficiently specific for RMS as integrins are also overexpressed in all the vascular endothelial cells of children.

Identification of cation-independent mannose 6-phosphate receptor (M6PR) overexpression on prostate cancer cells[140] led us to study the expression level of M6PR on other types of cancer such as RMS. In the present study, the overexpression of M6PR on RMS cells compared to healthy myoblasts was studied and confirmed. We therefore decided to target RMS cells using a M6PR pathway and more particularly using analogs of mannose 6-phosphate functionalized on an anomeric moiety (AMFA) grafted on nanoparticles.

We recently synthesized porphyrin-based periodic mesoporous organosilica nanoparticles (PMO), presenting a 250 nm diameter and showing interconnected cavities (from

10 to 80 nm) for breast cancer treatment using two-photon excited photodynamic therapy (TPE-PDT).[46] To synthesize these PMO, a large functional octatriethoxysilylated porphyrin precursor was condensed without any silica source. The framework of the nanoparticles was formed by J-aggregates of porphyrins inside the pores of the walls, allowing two-photon excitation (TPE).[213] TPE is of particular interest for biological applications because it allows a deep penetration of the near-infrared beam down to 2 cm in soft tissues and a high spatiotemporal resolution for imaging and cancer detection. Importantly, TPE-PDT has demonstrated a high potential for cancer therapy, in particular, the treatment of small-sized tumors.[214]

Therefore, we present here the combination of PMO with AMFA to target M6PR overexpressed in RMS cells of both phenotypes, embryonal and alveolar subtypes of RMS, for TPE-PDT. The strong therapeutic potential and selectivity of PMO grafted with PEG and AMFA were demonstrated.

1.1. Experimental part

Materials

Cetyltrimethylammonium bromide (CTAB, 99%), sodium hydroxide (NaOH, 97%), toluene, and ammonium nitrate (NH_4NO_3) were purchased from Sigma-Aldrich. Ethanol (EtOH) was purchased from VWR. Aminoundecyltriethoxysilane and PEG-triethoxysilane were purchased from SIKEMIA. p-[N- (2-Ethoxy-3,4-dioxocyclobut-1-enyl)amino]phenyl 6 deoxy-7- hydroxycarbonyl-α-D-manno-heptopyranoside [M6C-PhSq] was synthesized described by E. Bouffard *et al.*[139] Octapropargyl porphyrin derivative was prepared according to the synthesis described by M. Fathalla *et al.*[215]

Analytical techniques

^1H and ^{13}C solution NMR spectra were recorded on a Bruker AC 400 spectrometer. Chemical shifts (in δ units, ppm) are referenced to TMS using residual DMSO-d_6 (δ = 2.50 ppm) resonance as the internal standard for ^1H NMR spectra, and DMSO-d_6 (δ = 39.52 ppm) for ^{13}C NMR spectra. UV-vis absorption spectra were recorded on a Hewlett-Packard 8453 spectrophotometer using correction factors supplied by the manufacturer. TEM analysis was performed on a JEOL 1200 EXII instrument. Dynamic light scattering analyses were performed using a Cordouan Technologies DL 135 Particle Size Analyzer instrument and analyzed with NanoQ software. IR spectra were recorded on a PerkinElmer 100 FT spectrophotometer. Zeta

potential measurements were performed with a Malvern Zetasizer NanoSeries Instrument (pH = 7, NaCl 5 mM). Click reaction was performed using a microwave CEM Discover-Explorer.

Nanomaterials synthesis and characterization

Synthesis of the octasilylated porphyrin derivative

A mixture of the octapropargyl porphyrin derivative (100 mg, 9.0×10^{-2} mmol), bromotris(triphenylphosphine)-copper(I) ([$CuBr(PPh_3)_3$], 13 mg, 1.5×10^{-2} mmol), and anhydrous THF (3 mL) was placed in a 10 mL sealable microwave reactor, and 3-azidopropyltriethoxysilane (178 mg, 7.1×10^{-1} mmol) was added. Then, the tube was flushed with argon and microwave irradiation was conducted for 30 min at 100 °C (maximum power 200 W). After evaporation of the solvent, octasilylated porphyrin was quantitatively obtained as a purple solid (225 mg, 7.25×10^{-2} mmol). ^{1}H NMR (400 MHz, DMSO-d^6, δ): 8.94 (s, 8H, H$\beta_{pyrrole}$), 8.35 (t, broad, 4H, H_4 aryl), 7.53 (d, $^4J_{H-H}$= 1.5 Hz, 8H, $H_{2,6}$ aryl), 7.28 (s, 8H, triazole), 5.41 (s, 16H, aryl-CH_2-triazole), 4.42 (t, 16H, $^3J_{H-H}$= 6.9 Hz, CH_2-CH_2- triazole), 3.76 (q, $^3J_{H-H}$= 7.0 Hz, 48H, O-CH_2-CH_3), 1.95 (m, 16H, CH_2-CH_2-CH_2-Si), 1.15 (t, $^3J_{H-H}$= 7.0 Hz, 72H, O-CH_2-CH_3), 0.58 (t, $^3J_{H-H}$ = 8 Hz, 16H, CH_2-Si); ^{13}C{1 H} NMR (400 MHz, DMSO-d_6, δ): 157.3, 149.1, 142.6, 131.9, 128.6, 124.5, 119.9, 114.6, 100.8, 61.6, 57.6, 51.7, 23.9, 17.8, 6.9; ^{13}C NMR (100 MHz, DMSO-d^6), δ: 157.3, 149.1, 142.6, 131.9, 128.6, 124.5, 119.9, 114.6, 100.8, 61.6, 57.6, 51.7, 23.9, 17.8, 6.9; ^{29}Si NMR (79 MHz, DMSO-d^6, δ) : -46.5; FTIR (KBr): ν = 2973, 2931, 2900, 1600, 1446, 1402, 1357, 1183, 1165, 1125, 1100, 990, 940, 790, 709, 682 cm^{-1}; UV–vis (EtOH) : λ_{max} = 426, 559, 595 nm; Emission (EtOH): λ_{max} = 601, 651 nm ($\lambda_{excitation}$ = 420 nm); HRMS (MALDI-TOF): calcd for $C_{140}H_{212}N_{28}O_{32}Si_8Zn$, 3089.440, found 3089.329.

Synthesis of the porous porphyrin-based organosilica nanoparticles (PMO)

PMO were synthetized following the protocol previously described by C. Mauriello Jimenez *et al.*[46] A mixture of CTAB (120 mg, 0.39 mmol), distilled water (60 mL), and NaOH (0.2 M aqueous solution, 437 µL) was stirred at 80 °C for 2 hours at 750 rpm in a 250 mL three-neck round bottom flask. Then, the octasilylated porphyrin (55 mg, 0.018 mmol, in 1 mL of absolute ethanol) was added, and the mixture was stirred for 30 hours at 80 °C. Afterwards, the solution was cooled to room temperature while stirring. The crude mixture was centrifuged (20 000 rpm, 20 min). The supernatant was removed, and the PMO were washed with ethanol and stored at 4 °C.

Synthesis of the PMO-PEG/NH_2 nanoparticles

After centrifugation, PMO (48.8 mg) were resuspended in 6 ml of toluene at 100 °C. Then a mixture of 11-aminoundecyltriethoxysilane (29.3 mg – 87.8 µmoles) and PEG-triethoxysilane (MW = 410.62 – 36 mg – 87.8 µmoles) was dissolved in 1 mL of toluene and added to the PMO. 20 µL of water was added to the reaction. The reaction was kept under stirring 18h at 100 °C. Then, it was cooled down to room temperature and centrifuged for 30 minutes at 20 000 rpm. The supernatant was removed and the solid was washed with EtOH leading to 40 mg of grafted PMO-PEG/NH_2 in EtOH.

Synthesis of PMO–AMFA nanoparticles

10 mg of PMO-PEG/NH_2 was resuspended in ethanol at 50 °C. A water solution (2 mL) of 3.6 mg of AMFA, more precisely a mannose 6-carboxylate with a phenyl squarate arm (M6C-PhSq), was added dropwise to the PMO. The reaction was kept under stirring at 50 °C, 18 h. Then, the resulting mixture was cooled down to room temperature and centrifuged. The supernatant was then removed and the solid washed trice with a solution of ammonium nitrate in ethanol (6 $g \cdot L^{-1}$), water, and ethanol leading to 9.3 mg of grafted PMO–AMFA in EtOH.

AMFA grafting quantification

The amount of AMFA grafted on PMO was determined by HPLC measurement in the supernatant using projection with a reference solution of AMFA at different concentrations. We calculated indirectly the grafting efficiency by separating the nanoparticles out of the suspension with ultracentrifugation at the end of the reaction and measured the AMFA concentration in the supernatant with HPLC. We performed a calibration curve using HPLC and took a reading for our supernatant. One µL of the solution of subsequent dilutions from 0.84 to 0.1 µg mL^{-1} of AMFA, prepared in water/ethanol, was injected into HPLC Agilent 1260 infinity on a Kinetex EVO column C18 1.7 µM 100 Å 50 × 2.1 mm. One µL of the supernatant was injected and gave us the quantification of non-grafted AMFA. The amount of grafted AMFA is 66 µg of AMFA per mg of PMO. The mobile phase consisted of a mixture of acetonitrile and water with trifluoroacetic acid and was eluted at a flow rate of 0.5 mL min^{-1}. The analysis was performed at 298 nm, and the run time was about 11 min. The chromatographic data analysis was performed using Agilent OpenLAB Software. Linearity was determined through the construction of three calibration curves using five AMFA concentrations at three wavelengths specific to AMFA absorbance (298, 223 and 198 nm).

Linear least squares methodology was applied to calculate the calibration equation and correlation coefficient.

Biological studies

Cell culture

Rhabdomyosarcoma cell lines Rh30 from ATCC; Rh4, Rh18, Rh36, and RD from Peter Houghton (The Research Institute at Nationwide Children's Hospital, Columbus OH); RMS and RMS-YM from Janet Shipley (The Institute of Cancer Research, London, UK); JR and Rh28 from Corinne Linardic (Duke University School of Medicine, Durham, NC); Rh5 from Susan Ragsdale (St Jude Children's Research Hospital, Memphis, TN); RUCH-3 from Beat Schäfer (University Children's Hospital, Zurich, Switzerland); TTC442 from Timothy Triche (Children's Hospital of Los Angeles, Los Angeles, CA); SK-1111 normal myoblasts from CookMyoSite, and MH38 normal myoblasts provided by G. Carnac (Inserm U1046-UMR CNRS 9214, Montpellier, France) were used. RMS-YM, RD and RMS cells were cultured in RPMI-1640 medium supplemented with 10% FBS and 1% penicillin/streptomycin. SK-1111 and MH38 were cultured in Ham F10 medium plus 20% fetal bovine serum, 1% insulin, 25 ng mL^{-1} FGF, 10 ng mL^{-1} EGF and 1% penicillin/streptomycin. All cell types were allowed to grow in a humidified atmosphere at 37 °C under 5% CO_2.

Western blotting

To study the expression level of M6PR, RMS-YM, RD, RMS, SK-1111 and MH38 were subjected to western blot analysis. The cells were harvested, washed three times in PBS and lysed by three freeze–thaw cycles in a buffer containing 50 mM HEPES, 150 mM NaCl, 1 mM EDTA, 2.5 mM EGTA, 0,1% Tween 20, 10% glycerol, 1 mM NaF, 1 mM $NaNO_3$, 10 mM glycerophosphate and protease inhibitors (dilution 1: 25 Complete, Roche Diagnostics). The lysates were precleared by centrifugation at 10 000g for 15 min at 4 °C. Samples were tested for protein concentration by the Bradford method and equal amounts (25 µg) of cell extract and 1 µg bovine purified M6PR were resolved by 12% SDS-PAGE electrophoresis. After blotting, the gel was transferred onto the PVDF membrane and the M6PR protein was detected by probing with the antihuman M6PR (cation independent) antibody (dilution 1: 50 000, Abcam). β-Actin detected by a monoclonal mouse antibody was used as the loading control. Immunoblotting was performed using a secondary antibody coupled with horseradish peroxidase and revealed by the ECL detection system (Amersham).

Proteomic analysis

Membrane proteins were enriched from 80–90% confluent cells plated in six 15 cm dishes, following a two-step centrifugation protocol.[216] After gel separation, and in-gel digestion, peptides were loaded onto HPLC-MS.[217] Data acquisition was made in the data dependent mode with precursor ion scans recorded in the Fourier transform detector (FT) with resolution ≥60 000 (at m/z-400) and fragment spectra of the most intense precursor ions in an Orbitrap (QE). For protein quantification, we relied on the MaxQuant built-in label-free quantification (LFQ) algorithm[218] and also applied a top3 peptide approach.[217,219] For top3, all peptide form identifications within a sample set in the evidence output file from MaxQuant were median normalized before imputation of missing values from the normal distribution of LOG2-transformed peptides using a down shift of 1.8 and a width of 0.3 standard deviations, a left-censored imputation strategy set as default in Perseus software (version 1.5.5.3).[220] Missing value imputation was carried out when there were at least two peptide form identifications in all technical replicates from the same sample, otherwise the intensity was set to zero according to recommendations.[221] The three most intense peptide intensities were then summed to the protein group iTop3 intensity.

Cytotoxicity measurement

For cytotoxicity analysis, RMS-YM and SK-1111 cells were seeded into a 96 well plate, 2000 cells per well in 200 µL of culture medium and allowed to grow for 24 h. Then the cells were treated with increasing concentrations of nanoparticles (from 1 to 100 µg mL^{-1}). Three days after treatment, a MTT assay was performed to determine the cell viability. Briefly, cells were incubated for 4 h with 0.5 mg mL^{-1} of MTT (3-(4,5-dimethylthiazol-2-yl)-2,5-diphenyltetrazolium bromide; Promega) in media. The MTT/media solution was then removed and the precipitated crystals were dissolved in EtOH/ DMSO (v/v). The solution absorbance was read at 540 nm in a microplate reader. All values are reported in relation to the control values (without any treatment) which are considered as 100% living cells.

Two-photon excited photodynamic therapy

RMS-YM and SK-1111 cells were seeded into a 384 multi-well glass-bottomed plate (thickness 0.17 mm) with a black polystyrene frame at a concentration of 1000 cells per well in 50 µL of culture medium, and allowed to grow for 24 h. Then, cells were treated with nanoparticles (40 µg mL^{-1}) for 16 h. For M6P competitive inhibition, the cells were incubated or not with 10 mM of M6P for 10 min prior to the incubation with PMO–AMFA (40 µg mL^{-1})

for 4 h. The cells were submitted or not to laser irradiation with the LSM 780 live confocal microscope (Carl Zeiss Microscope) at 800 nm by 3 scans of 1.57 s duration in 4 different areas of the well with a focused laser at a maximum laser power (laser power input 3 W). The laser beam was focused by a microscope objective lens (Carl Zeiss 10×/0.3 EC Plan-Neofluar). After 2 days, the MTT assay was performed as previously described and was corrected according to the following formula: Abs "No laser" − 2 × (Abs "No laser" − Abs "Laser").

Two-photon fluorescence imaging

RMS-YM cells were grown on a tissue culture dish with cover glass bottom (FluoroDish from WPI) in complete culture medium. The next day, the cells were treated or not with 10 mM of M6P for 10 min, then the cells were incubated with PMO–AMFA (40 µg mL^{-1}) for 4 h. Fifteen minutes before the end of incubation, cells were loaded with Hoechst 33342 (5 µg mL^{-1}, Invitrogen, Cergy Pontoise, France) for nuclear staining and with green Cell Mask (5 µg mL^{-1}, Invitrogen) for membrane staining. Before visualization, cells were washed three times with cell media. Cells were examined under an LSM 780 live confocal microscope (Carl Zeiss Microscope) and excited at 488 nm for membranes at 760 nm for nuclei and 800 nm for PMO–AMFA. All images were performed with a high magnification (63×/1.4 OIL DIC Plan-Apo).

Flow cytometry

RMS-YM cancer cells were seeded on a 6-well plate for 24 h. Then, cells were treated or not with 40 µg mL^{-1} of PMO–AMFA for 0, 1, 2, 4, 16 and 24 h. After treatment, cells were washed thrice with culture medium, harvested and centrifuged (1300 rpm, 5 min). Cell pellets were re-suspended in PBS enriched with $CaCl_2^+$ and $MgCl_2^+$. Flow cytometry determination of PMO-AMFA positive cells was done by FACS Novocyte Flow Cytometer (ACEA Biosciences Inc.) with a minimum of 5000 cells collected (excitation laser 561 nm; filter: 660 ± 20 nm).

Statistical analysis

Statistical analysis was performed using the Student's t test to compare paired groups of data. A p-value of <0.05 was considered to be statistically significant.

1.2. Results and discussion

Overexpression of M6PR on RMS cells

The first step of this work was the study of M6PR expression on RMS cells of embryonal and alveolar subtypes and healthy myoblasts. For this, the protein expression level of M6PR in three different RMS cells lines and in healthy myoblasts was analyzed by a western blot (Figure 7).

As shown in Fig. 7A, the protein expression level of M6PR is clearly higher in RMS cell lines than in healthy myoblasts. The quantification of the M6PR level by Image J software corrected by the expression level of an invariant (β-actin) indicated that on average, there was a 7-fold-higher M6PR expression in RMS cells than in healthy cells (Fig. 7B). To confirm and to expand these data, we performed proteomic analysis of the membrane fraction of several RMS cell lines. Healthy myoblasts were used as the control (Fig. 7C). These results confirmed a higher expression of M6PR in RMS cell lines of both the alveolar and embryonal subtypes. This suggested that the increase in M6PR expression could be considered as a biomarker of RMS development.

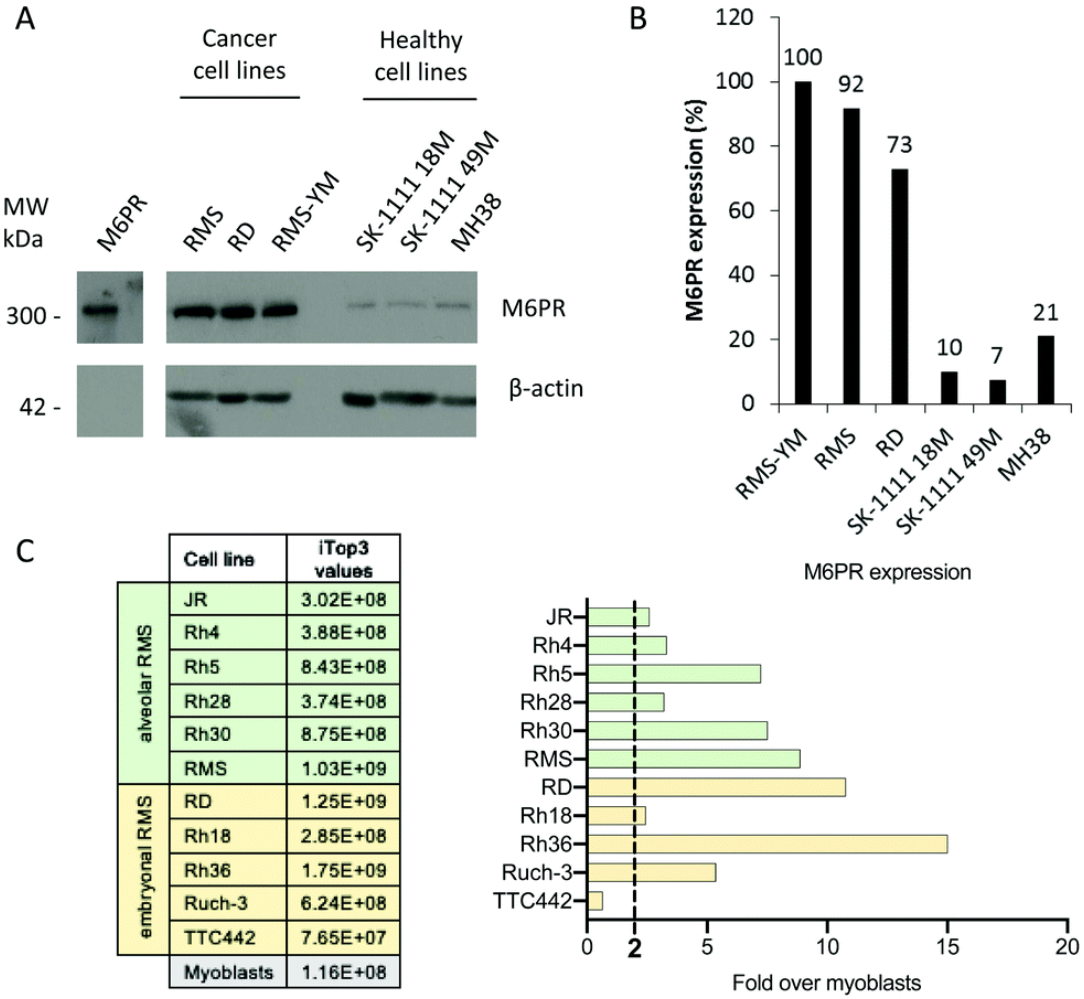

Figure 7. M6PR expression in different cell lines. (A) The cell extracts (25 µg) were analyzed by Western blots using human M6PR or β-actin antibodies. β-actin is a control for total protein loading. (B) Quantification with Image J software of 300-kDa M6PR protein corrected by β-actin expression. RMS-YM cells are considered as 100%. (C) Proteomics analysis of M6PR expression in a panel of RMS cell lines. Membrane proteins were enriched with two-step centrifugation protocol and analyzed by HPLC-MS. iTop3 values were calculated from the sum of the intensity of the three most intense peptides of each Leading Razor Protein.

Synthesis of PMO grafted with PEG and AMFA

Porphyrin-based PMO were first synthesized following our recently described procedure (Fig. 8A).[46] We then investigated the functionalization of PMO with AMFA (Fig. 8B). For this, aminoundecyltriethoxysilane and PEG triethoxysilane were first grafted on the surface of PMO following a method we published on mesoporous silica nanoparticles (MSN) of 20 nm diameter. [143] Then AMFA was grafted on the surface of functionalized PMO. Here, the AMFA used was the M6C-PhSq (Fig. 8B), and the reaction of its squarate moiety with the amino groups led to a covalent attachment of AMFA on the surface of PMO.

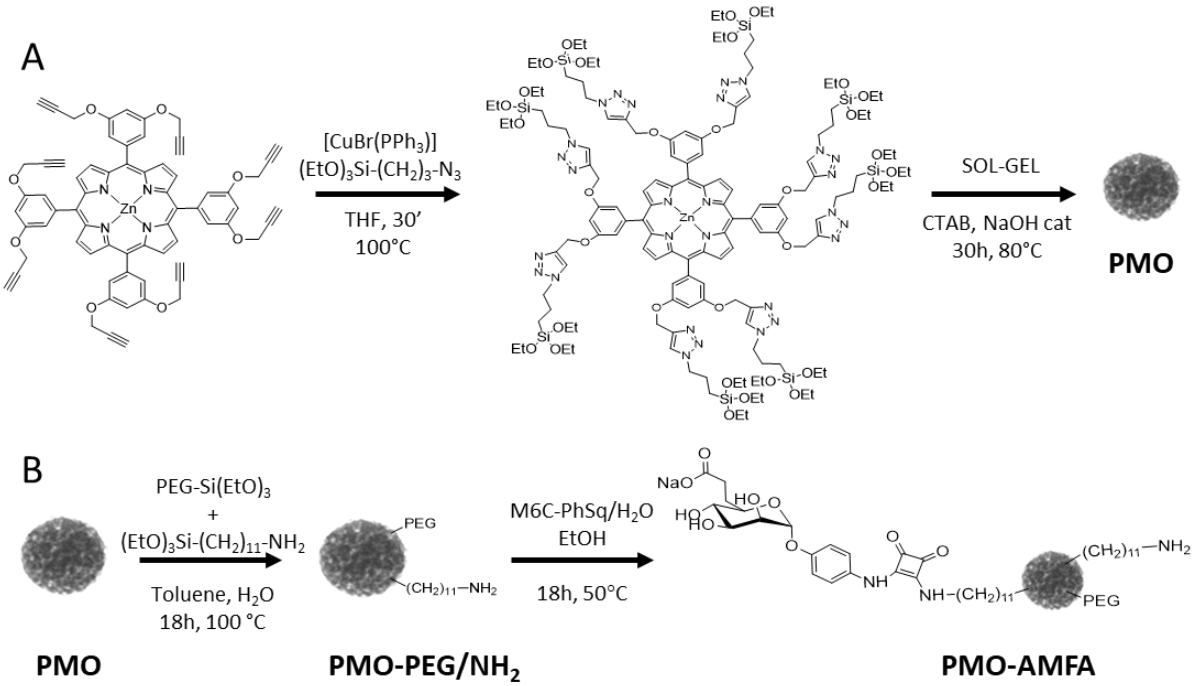

Figure 8. Synthesis of PMO-AMFA. (A) Synthesis of PMO. (B) Schematic representation of the coupling of mannose 6-carboxylate with a phenyl squarate arm (M6C-PhSq) also called AMFA in order to obtain PMO–AMFA.

The different steps of the functionalization were monitored by DLS and zeta potential. PMO nanoparticles showed a negative zeta potential (−38.3 ± 0.5 mV, after extraction of the surfactant), which can be attributed to the deprotonated silanol groups on the surface. The DLS showed a 245 nm hydrodynamic diameter. After functionalization with NH_2 groups and PEG, the hydrodynamic diameter increased to 310 nm and the zeta potential was found to be +18.3 mV ± 0.2 (after extraction of the surfactant). The increased diameter and charge reversal showed the successful functionalization of PMO-NH_2. The AMFA grafting level was quantified by HPLC demonstrating that 66 μg of AMFA was grafted per mg of PMO. This reaction led to a 399 nm hydrodynamic diameter (Fig. 9A) and a negative zeta potential of −22.9 ± 0.3 mV, which is in agreement with the anchoring of the carbohydrate moiety on the surface of the nanoparticles. TEM imaging of PMO–AMFA showed a homogenous dispersion and a large number of small-sized nanoparticles and an average size of 312 ± 103 nm (Fig. 9B).

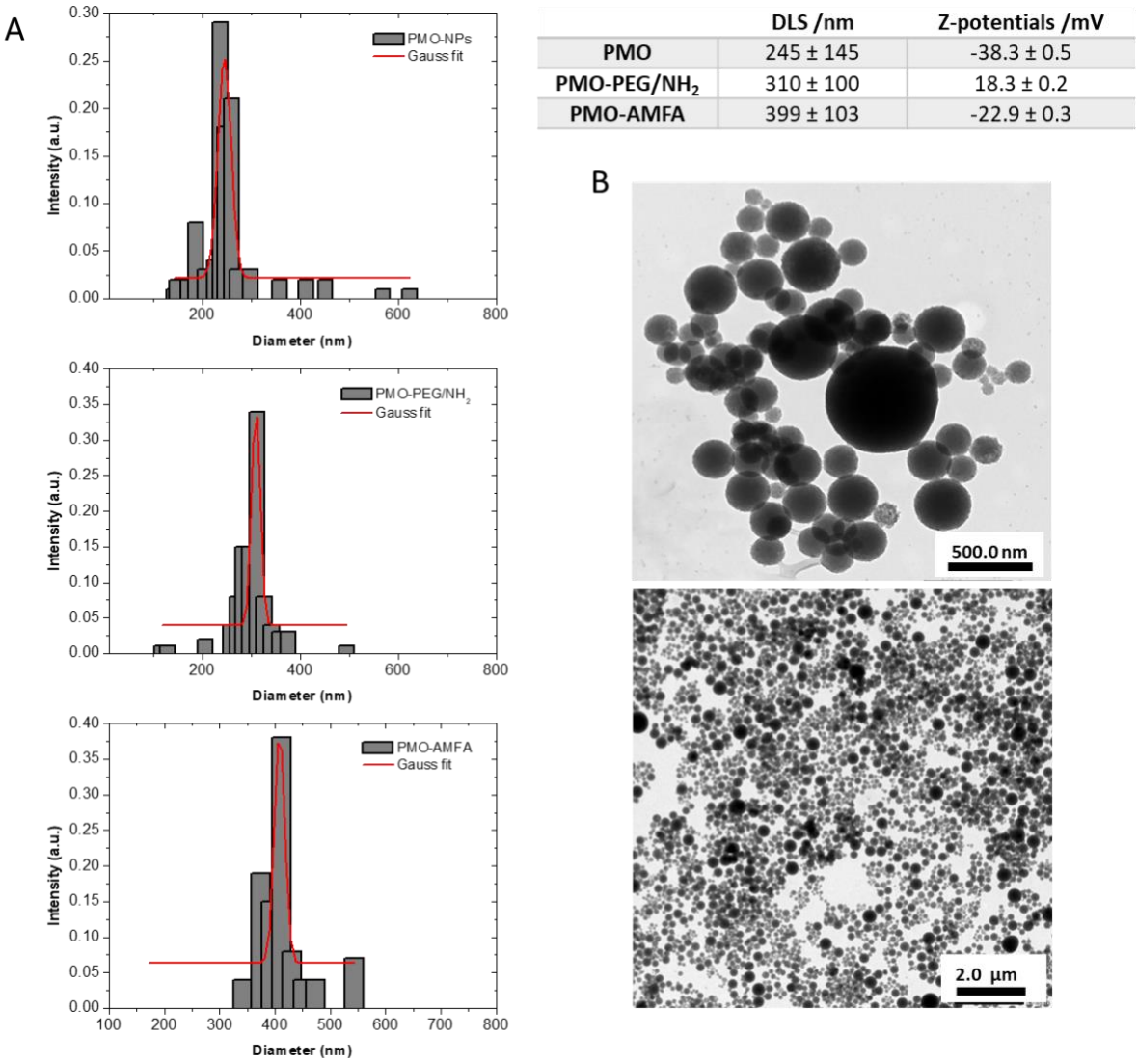

	DLS /nm	Z-potentials /mV
PMO	245 ± 145	-38.3 ± 0.5
PMO-PEG/NH_2	310 ± 100	18.3 ± 0.2
PMO-AMFA	399 ± 103	-22.9 ± 0.3

Figure 9. Characterization of PMO–AMFA. (A) DLS in intensity and zeta potential of PMO (after surfactant extraction), PMO-PEG/NH_2 and PMO–AMFA. (B) Microscopy images of PMO–AMFA by TEM at different magnifications.

Biocompatibility of PMO on different cell lines

A cytotoxic study was carried out by 3 days incubation time with increasing concentrations of PMO grafted with PEG and AMFA. This study was performed on one RMS and one healthy cell line: RMS-YM and SK-1111, respectively. These data demonstrated that for both cell lines, the batch of PMO, which were grafted with PEG and AMFA (PMO–AMFA), did not show significant cytotoxicity (Figure 10). In contrast, pristine PMO (here called PMO) generated slight cell death. In fact, in RMS-YM cells, the incubation with PMO at 100 µg mL^{-1} induced 30% cell death (Fig. 10A). In SK-1111, PMO and PMO-PEG/NH_2 at 100 µg mL^{-1} induced approximately the same percentage of cell death (Fig. 10B). However, up to 40 µg

mL^{-1} no significant cell death was observed in any of the cell lines. So, this concentration was chosen for further biological experiments.

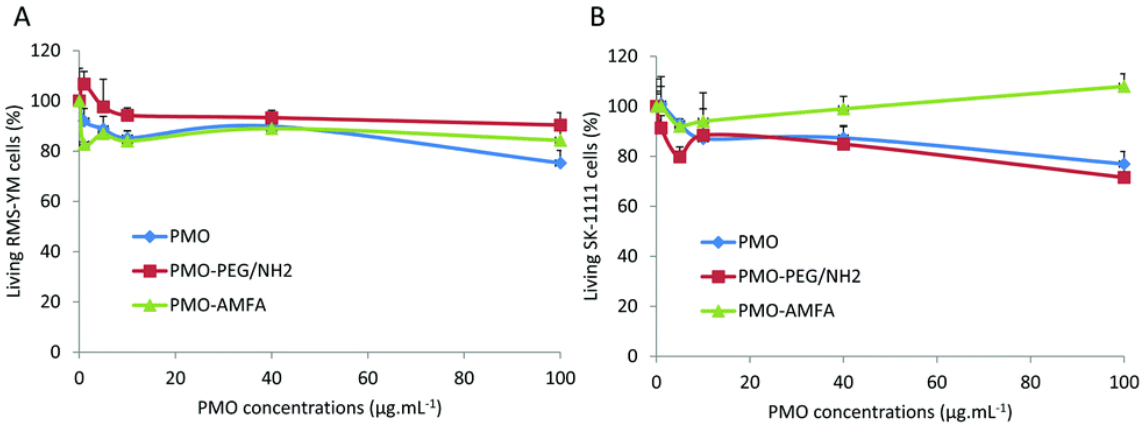

Figure 10. Cytotoxicity of PMO on cancer and healthy cells. Cytotoxicity of PMO on RMS and healthy cells. (A) RMS-YM cells and (B) SK-1111 healthy cells were treated with increasing concentrations of nanoparticles. After three days of incubation, a MTT assay was performed. Data are presented as mean ± SEM, of two independent experiments realized in triplicate.

Study of TPE-PDT and fluorescence imaging potential

The potential of PMO–AMFA to target and kill RMS cells under near infrared two-photon excitation was studied (Figure 11). For this purpose, RMS-YM cancer cells and SK-1111 healthy cells were incubated with 40 µg mL^{-1} of PMO, PMO-PEG/NH_2 or PMO–AMFA for 16 h. Then, the cells were irradiated or not at 800 nm for a short time (3 × 1.57 s) at maximal laser power (Fig. 11A and B). PMO and PMO-PEG/NH_2 induced 62% and 57% RMS-YM cell death, respectively. On SK-1111 healthy cells, PMO and PMO-PEG/NH_2 induced 51% and 50% cell death, respectively. This result suggested that PMO and PMO-PEG/NH_2 exhibited a similar effect on both cell types. Interestingly, PMO–AMFA were highly efficient on cancer cells, inducing 94% RMS-YM cell death after TPE, but did not induce any significant phototoxicity on healthy cells. This result demonstrated the importance of the targeting and the specificity of PMO–AMFA for RMS.

The M6PR involvement in the active endocytosis of PMO– AMFA was demonstrated by addition in the culture medium of the natural ligand of M6PR, the M6P. This experiment was based on a competitive inhibition of PMO–AMFA endocytosis by M6P. RMS-YM cells were incubated for 4 h with PMO–AMFA in the presence or absence of excess M6P (10 mM). Under TPE-PDT PMO–AMFA induced 58% cancer cell death. Importantly, the addition of M6P totally inhibited RMS-YM cell death meaning that M6P prevented the internalization of

PMO AMFA through the M6PR pathway (Fig. 11C). This result was confirmed by two-photon fluorescence imaging demonstrating the almost total disappearance of the luminescent red dots of PMO–AMFA, in the presence of M6P (Fig. 11D).

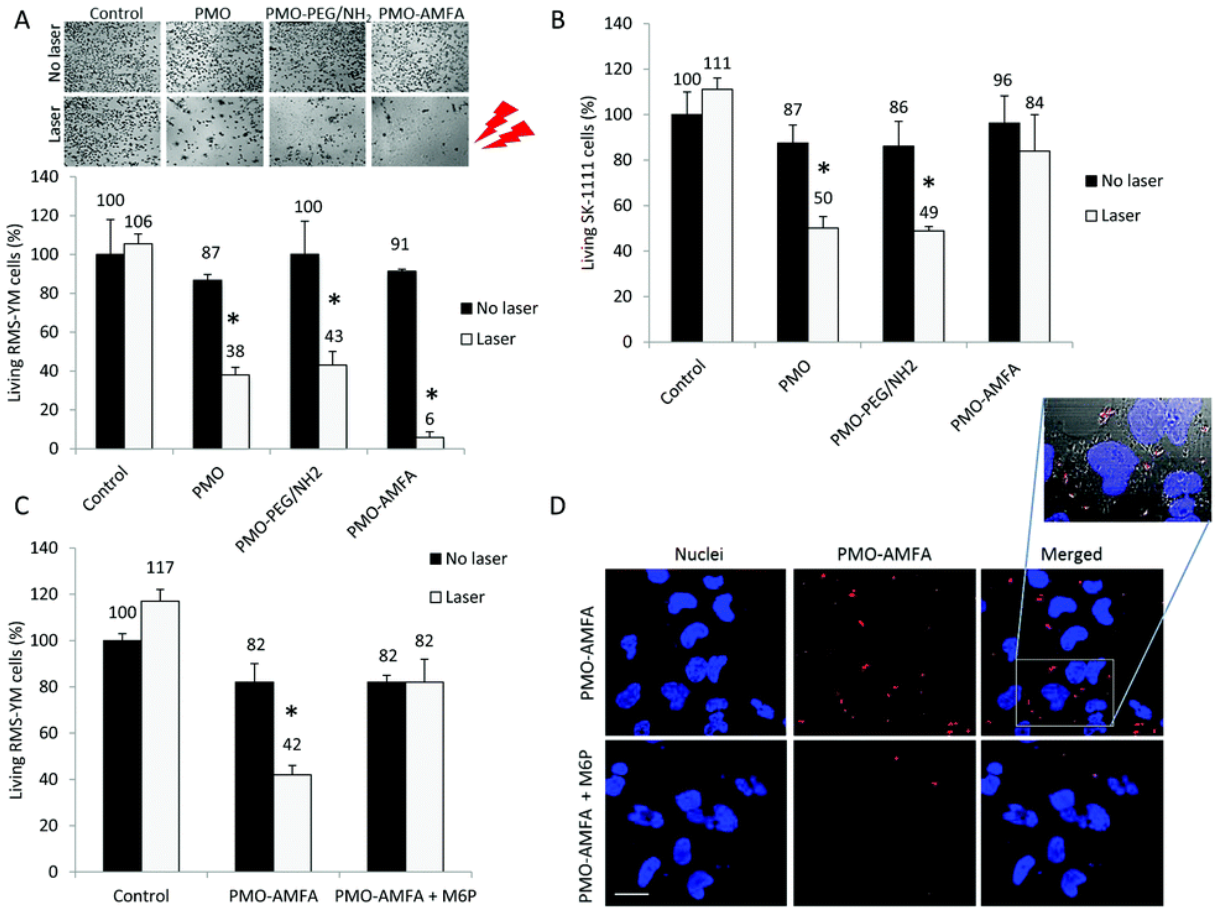

Figure 11. TPE-PDT and fluorescence imaging with PMO. (A) Cancer cells (RMS-YM) were incubated for 16h with PMO (40 µg mL^{-1}) and irradiated at 800 nm (3 × 1.57 s). The top of (A) shows pictures of living cells revealed by the MTT reagent. Scale bar: 100 µm. The bottom of (A) shows quantification of cell death. (B) Healthy cells (SK-1111) were incubated for 16 h with PMO (40 µg mL^{-1}) and irradiated at 800 nm (3 × 1.57 s). (C) RMS-YM were incubated for 4 h with PMO–AMFA (40 µg mL^{-1}) in the presence or absence of M6P (10 mM). (D) Confocal fluorescence imaging of RMS-YM cells incubated with PMO–AMFA (40 µg mL^{-1}) in the presence or absence of M6P (10 mM). The enlargement concerns merged stains of PMO–AMFA, the nuclei and phase contrast imaging. Scale bar: 10 µm. Data are mean values ± standard deviations from three independent experiments. *Statistically significant versus non-irradiated PMO ($p < 0.05$ from the Student's t test).

To study the subcellular localization of PMO–AMFA in RMS-YM cells, a confocal imaging experiment on living cells was performed at 2 incubation times (4 h and 16 h), in the presence of cell membrane (CellMask) and nucleus (Hoechst) staining. Fig. 12A showed that the 4 h incubation time was sufficient for PMO–AMFA detection mainly at the cell membranes.

After 16 h incubation time, PMO–AMFA were largely internalized inside the cells. This observation was confirmed by flow cytometry experiments of RMS-YM cells incubated with 40 µg mL^{-1} PMO–AMFA for 1 to 24 h. Fig. 12B shows the increasing number of stained cells, related to the incubation time.

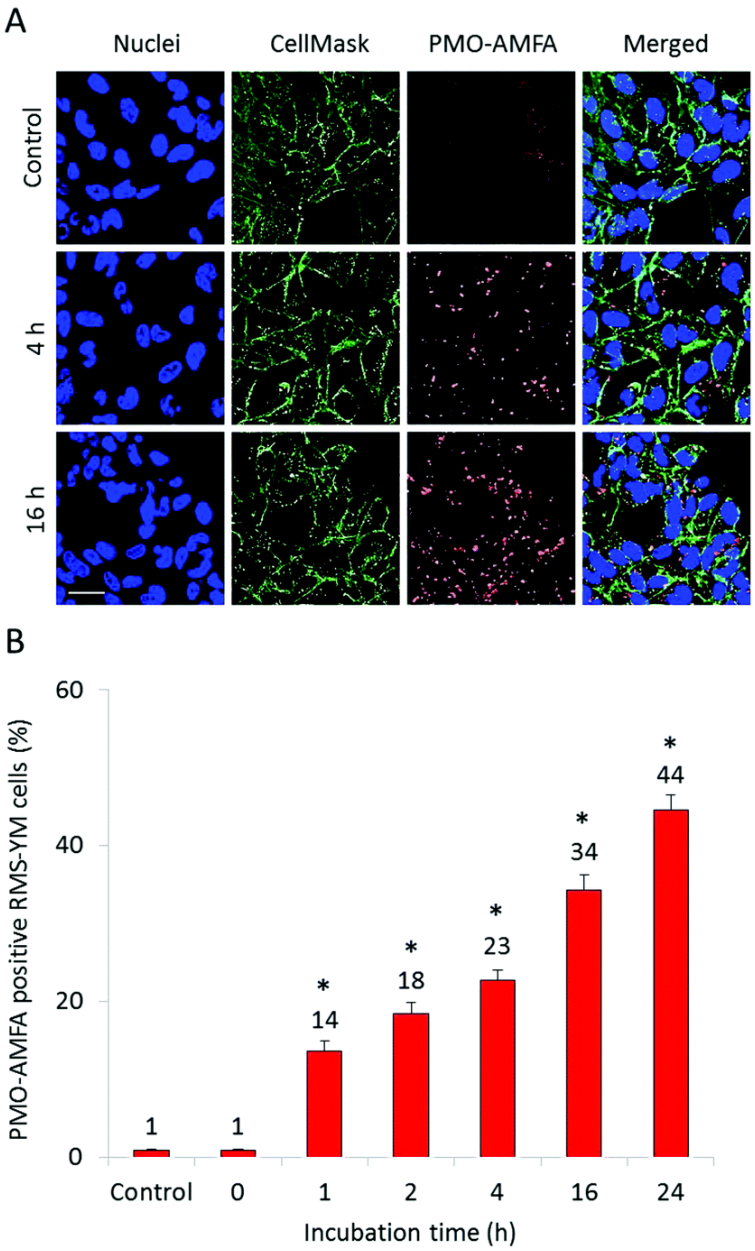

Figure 12. PMO–AMFA internalization in RMS-YM cells. (A) Confocal imaging on living cells in the presence of Hoechst (nuclei stained blue) and Cell mask (membranes stained green) after 4 h and 16 h of incubation time. Scale bar: 10 µm. (B) Quantification of PMO–AMFA in RMS-YM cells by flow cytometry experiments after increasing the incubation times (from 1 h to 24 h). Bar graphs are mean ± standard deviations of two experiments. *Statistically significant versus control ($p < 0.05$ from the Student's t test).

1.3. Conclusions

In this study, we have demonstrated that M6PR is a new target for rhabdomyosarcomas. In fact, we have observed an overexpression of this receptor in a panel of RMS cells of different subtypes (embryonal and alveolar) allowing differentiation between cancer cells and healthy cells. The targeting of M6PR was performed using AMFA and more precisely by the grafting of a carboxylate analog of mannose 6-phosphate on the PMO. Altogether, the results presented here show that PMO–AMFA was highly efficient for TPE-theranostics of RMS-YM cells through cell uptake involving M6PR. Moreover, PMO– AMFA did not show any effect on healthy cells, demonstrating the specificity of the targeting toward cancer cells. Targeted TPE-PDT could be considered as a new promising therapeutic strategy for rhabdomyosarcomas.

1.4. Perspectives

This work could be completed in two ways; first, we may consider studying the use of another carbohydrate such as dimannoside-carboxylate ethyl squarate. A higher affinity of the dimannoside for the CI-M6PR compared to the monosaccharide was reported in the bibliography. [222] We could expect even stronger TPE-PDT effect onto RMS cells. Second, we could envisage testing the PMO–AMFA *in vivo* in different models such as the CAM model or the zebrafish, which are alternatives to the traditional mammalian models. Their internalization, biodistribution as well as the TPE-PDT effect might be assessed.

Part II. Porphyrin-based periodic mesoporous organosilica nanoparticles for TPE-induced siRNA delivery on MCF-7 cells

Introduction

Gene silencing could be defined as the process of "turning off" a gene by the introduction of double-stranded RNA (dsRNA) into a cell.[223] This dsRNA is cut into small interfering RNAs (siRNAs) which will be integrated into the RNA-induced silencing complex (RISC). Afterward, silencing of the target mRNA *via* degradation and/or transcriptional repression is observed [224-225] Fire and coworkers described the RNA interference for the first time in 1998.[226] First example of gene knockdown in mammalian cells was shown by Tuschl and coworkers in 2001.[227]

Nevertheless, siRNA requires a delivery system to overcome the physical limitations of siRNA, such as its negative charge and its size (around 13 kDa). The siRNA cannot pass through cellular membranes and is degraded by endogenous nucleases. Non-viral vectors emerge as a tool for the protection and the delivery of nucleic acids, presenting advantages already mentioned in section 2.3.5 of chapter 1, for their use in different fields such as cancer treatment.[228-229] Together with the use of vectors, and among other options like proton sponge effect [230] or the use of fusogenic groups [231], photochemical internalization (PCI) appears as a technology to help in the delivery of siRNA or other macromolecules to cell cytosol. A controlled delivery since the release will take place in only light-exposed areas. In non-exposed areas, macromolecules tend to be degraded in the lysosomes. [232] As mentioned, this strategy is based on the irradiation of the PS, upon this irradiation, the photosensitizer located in the endocytic vesicles is activated. The activation of the PS produces reactive oxygen species responsible for the disruption of the endosomes-lysosomes membranes. This leads to the release of endocytosed compounds to the cytoplasm where they may act on their target directly or further translocate in the cytosol or to the nucleus.[233-234]

Hartono *et al*. synthesized large pore mesoporous silica nanoparticles functionalized with poly-L-lysine (PLL-LP-MSNs) for the delivery of functional siRNA against minibrain-related kinase and polo-like kinase 1 in osteosarcoma cancer cells, triggering a decrease in the cellular viability of the osteosarcoma cancer cells (KHOS cells). [235] Ekineker and coworkers described the synthesis of phthalocyanine-based porous organosilica NPs capable of complexing anti-Luc siRNA. Transfection experiments performed after NIR irradiation showed

an efficient internalization and a luciferase extinction of 65% in MCF-7 cancer cells expressing stable luciferase.[236] Salekdeh and colleagues prepared an aminoguanidine-PEGylated PMO (AGu@PEG1500- PMO) to employ as Cas9-sgRNA (RNP) complex nanocarrier. AGu@PEG1500-PMO was able to effectively transfer RNP in GFP-HT1080 cells, and cause the decrease of green protein fluorescent (GFP) in the cells.[237]

Here, we present the modification of the above-mentioned PMOsPOR-NPs with an aminosilane to perform anti-Luc siRNA complexation. A proof of concept of TPE-induced siRNA delivery and silencing effect on MCF-7-Luc cells is presented in this section.

2.1. Experimental part

Materials

Cetyltrimethylammonium bromide (CTAB, 99%), sodium hydroxide (NaOH, 97%), toluene, (3-Aminopropyl)triethoxysilane (APTES, 99%) and ammonium nitrate (NH_4NO_3) were purchased from Sigma-Aldrich. Ethanol (EtOH) was purchased from VWR. Aminoundecyltriethoxysilane and PEG-triethoxysilane were purchased from SIKEMIA. p-[N-(2-Ethoxy-3,4-dioxocyclobut-1-enyl)amino]phenyl 6 deoxy-7- hydroxycarbonyl-α-D-manno-heptopyranoside [M6C-PhSq] was synthesized following the protocol described by E. Bouffard *et al.*[139] Octapropargyl porphyrin derivative was prepared according to the synthesis described by M. Fathalla *et al.*[215]

Analytical techniques

^1H and ^{13}C solution NMR spectra were recorded on a Bruker AC 400 spectrometer. Chemical shifts (in δ units, ppm) are referenced to TMS using residual DMSO-d_6 (δ = 2.50 ppm) resonance as the internal standard for ^1H NMR spectra, and DMSO-d_6 (δ = 39.52 ppm) for ^{13}C NMR spectra. UV-vis absorption spectra were recorded on a Hewlett-Packard 8453 spectrophotometer using correction factors supplied by the manufacturer. TEM analysis was performed on a JEOL 1200 EXII instrument. Dynamic light scattering analyses were performed using a Cordouan Technologies DL 135 Particle Size Analyzer instrument and analyzed with NanoQ software. IR spectra were recorded on a PerkinElmer 100 FT spectrophotometer. Zeta potential measurements were performed with a Malvern Zetasizer NanoSeries Instrument. Click reaction was performed using a microwave CEM Discover-Explorer.

Nanomaterials synthesis and characterization

Synthesis of the octasilylated porphyrin derivative

A mixture of the octapropargyl porphyrin derivative (100 mg, 9.0 × 10^{-2} mmol), bromotris(triphenylphosphine)-copper(I) ([CuBr(PPh3)3], 13 mg, 1.5 × 10^{-2} mmol), and anhydrous THF (3 mL) was placed in a 10 mL sealable microwave reactor, and 3-azidopropyltriethoxysilane (178 mg, 7.1 × 10^{-1} mmol) was added. Then, the tube was flushed with argon and microwave irradiation was conducted for 30 min at 100 °C (maximum power 200 W). After evaporation of the solvent, octasilylated porphyrin was quantitatively obtained as a purple solid (225 mg, 7.25 × 10^{-2} mmol). ^{1}H NMR (400 MHz, DMSO-*d*^{6}, δ): 8.94 (s, 8H, H$\beta_{pyrrole}$), 8.35 (t, broad, 4H, H_4 aryl), 7.53 (d, $^{4}J_{H\text{-}H}$= 1.5 Hz, 8H, $H_{2,6}$ aryl), 7.28 (s, 8H, triazole), 5.41 (s, 16H, aryl-CH_2-triazole), 4.42 (t, 16H, $^{3}J_{H\text{-}H}$= 6.9 Hz, CH_2-CH_2- triazole), 3.76 (q, $^{3}J_{H\text{-}H}$= 7.0 Hz, 48H, O-CH_2-CH_3), 1.95 (m, 16H, CH_2-CH_2-CH_2-Si), 1.15 (t, $^{3}J_{H\text{-}H}$= 7.0 Hz, 72H, O-CH_2-CH_3), 0.58 (t, $^{3}J_{H\text{-}H}$ = 8 Hz, 16H, CH_2-Si); ^{13}C{1 H} NMR (400 MHz, DMSO-*d*^{6}, δ): 157.3, 149.1, 142.6, 131.9, 128.6, 124.5, 119.9, 114.6, 100.8, 61.6, 57.6, 51.7, 23.9, 17.8, 6.9; ^{13}C NMR (100 MHz, DMSO-*d*^{6}, δ): 157.3, 149.1, 142.6, 131.9, 128.6, 124.5, 119.9, 114.6, 100.8, 61.6, 57.6, 51.7, 23.9, 17.8, 6.9; ^{29}Si NMR (79 MHz, DMSO-*d*^{6}), δ : -46.5; FTIR (KBr): ν = 2973, 2931, 2900, 1600, 1446, 1402, 1357, 1183, 1165, 1125, 1100, 990, 940, 790, 709, 682 cm^{-1}; UV–vis (EtOH) : λ_{max} = 426, 559, 595 nm; Emission (EtOH): λ_{max} = 601, 651 nm ($\lambda_{excitation}$ = 420 nm); HRMS (MALDI-TOF): calcd for $C_{140}H_{212}N_{28}O_{32}Si_8Zn$, 3089.440, found 3089.329.

Synthesis of the porous porphyrin-based organosilica nanoparticles (PMO)

PMO were synthetized following the protocol previously described by C. Mauriello Jimenez *et al.*[46] A mixture of CTAB (120 mg, 0.39 mmol), distilled water (60 mL), and NaOH (0.2 M aqueous solution, 437 µL) was stirred at 80 °C for 2 hours at 750 rpm in a 250 mL three-neck round bottom flask. Then, the octasilylated porphyrin (55 mg, 0.018 mmol, in 1 mL of absolute ethanol) was added, and the mixture was stirred for 30 hours at 80 °C. Afterwards, the solution was cooled to room temperature while stirring. The crude mixture was centrifuged (20 000 rpm, 20 min). The supernatant was removed, and the PMO were washed with ethanol and stored at 4 °C.

Synthesis of the PMO-PEG/NH_2 nanoparticles

After centrifugation, PMO (48.8 mg) were resuspended in 6 ml of toluene at 100 °C. Then a mixture of 11-aminoundecyltriethoxysilane (29.3 mg – 87.8 µmoles) and PEG-triethoxysilane (MW = 410.62 – 36 mg – 87.8 µmoles) was dissolved in 1 mL of toluene and added to the PMO. 20 µL of water was added to the reaction. The reaction was kept under stirring 18 h at 100 °C. Then, it was cooled down to room temperature and centrifuged for 30 minutes at 20 000 rpm. The supernatant was removed and the solid was washed with EtOH leading to 40 mg of grafted PMO-PEG/NH_2 in EtOH.

Synthesis of PMO–AMFA nanoparticles

10 mg of PMO-PEG/NH_2 was resuspended in ethanol at 50 °C. A water solution (2 mL) of 3.6 mg of AMFA, more precisely a mannose 6-carboxylate with a phenyl squarate arm (M6C-PhSq), was added dropwise to the PMO. The reaction was kept under stirring at 50 °C, 18 h. Then, the resulting mixture was cooled down to room temperature and centrifuged. The supernatant was then removed and the solid washed with a solution of ammonium nitrate in ethanol (6 g L^{-1}), water, and ethanol leading to 9.3 mg of grafted PMO–AMFA in EtOH.

AMFA grafting quantification

The amount of AMFA grafted on PMO was determined by HPLC measurement in the supernatant using projection with a reference solution of AMFA at different concentrations. We calculated indirectly the grafting efficiency by separating the nanoparticles out of the suspension with ultracentrifugation at the end of the reaction, and measured the AMFA concentration in the supernatant with HPLC. We performed a calibration curve using HPLC and took a reading for our supernatant. One µL of the solution of subsequent dilutions from 0.84 to 0.1 µg mL^{-1} of AMFA, prepared in water/ethanol, was injected into HPLC Agilent 1260 infinity on a Kinetex EVO column C18 1.7 µM 100 Å 50 × 2.1 mm. One µL of the supernatant was injected and gave us the quantification of non-grafted AMFA. The amount of grafted AMFA is 66 µg of AMFA per mg of PMO. The mobile phase consisted of a mixture of acetonitrile and water with trifluoroacetic acid and was eluted at a flow rate of 0.5 mL min^{-1}. The analysis was performed at 298 nm, and the run time was about 11 min. The chromatographic data analysis was performed using Agilent OpenLAB Software. Linearity was determined through the construction of three calibration curves using five AMFA concentrations at three wavelengths specific to AMFA absorbance (298, 223 and 198 nm).

Linear least squares methodology was applied to calculate the calibration equation and correlation coefficient.

Synthesis of PMO–AMFA–APTES nanoparticles

9.75 mg of PMO–AMFA was resuspended in ethanol at 50 °C. Then 4.56 µL of APTES (MW = 221.372, 0.0195 mmoles) was added to the PMO. 20 µL of water was also added to the reaction. The reaction was kept under stirring 18 h at 50 °C. Then, it was cooled down to room temperature and centrifuged for 30 minutes at 20 000 rpm. The supernatant was removed and the solid was washed with EtOH leading to 7 mg of grafted PMO–AMFA–APTES in EtOH.

Biological studies

Cell culture

RMS-YM, MCF-7 and MCF-7-Luc cells from ATCC were used. RMS-YM cells were cultured in RPMI-1640 medium supplemented with 10% FBS and 1% penicillin/streptomycin. MCF-7 were cultured in DMEM medium supplemented with 10% FBS and 50 µg mL^{-1} gentamycin. MCF-7-luc were cultured in DMEM/F12 medium supplemented with 10% FBS and 1% geneticine. All cell types were allowed to grow in a humidified atmosphere at 37 °C under 5% CO_2.

Cytotoxicity measurement

For cytotoxicity analysis, RMS-YM cells were seeded into a 96 well plate, 2000 cells per well in 200 µL of culture medium and allowed to grow for 24 h. Then the cells were treated with increasing concentrations of nanoparticles from 0.01 to 100 µg mL^{-1}. Two days after treatment, a Hoechst assay was performed to determine the cell viability. Briefly, cells were incubated for 30 min with 0.1 mg mL^{-1} of Hoechst 33342 nuclear staining (2'-(4'-ethoxyphenyl)-5-(4-methylpiperazin-1-yl)-2,5'-bis-1H-benzimidazole trihydrochloride trihydrate; Promega) and then they were analyzed by microscopy. All values are reported in relation to the control values (without any treatment) which are considered as 100% living cells.

Two-photon excited photodynamic therapy

MCF-7 cells were seeded into a 384 multi-well glass-bottomed plate (thickness 0.17 mm) with a black polystyrene frame at a concentration of 1000 cells per well in 50 µL of culture medium, and allowed to grow for 24 h. Then, cells were treated with nanoparticles at 40 µg mL^{-1} for 16 h. The cells were submitted or not to laser irradiation with the LSM 780 live

confocal microscope (Carl Zeiss Microscope) at 800 nm by 3 scans of 1.57 s duration in 4 different areas of the well with a focused laser at a maximum laser power (laser power input 3 W). The laser beam was focused by a microscope objective lens (Carl Zeiss 10×/0.3 EC Plan-Neofluar). Cell death was assessed after 2 days and nuclear staining with Hoechst 33342. Image J allowed quantification of living cells. Values are the mean of three experiments and error bars represent standard deviation.

Gel retardation assay

Different amounts of PMO–AMFA–APTES and a fixed amount of siRNA Ctrl (1.8 µM) were mixed in a total volume of 22 µl and incubated in RNase free water for 60 min at 37°C to induce the formation of siRNA/PMO–AMFA–APTES complexes. After incubation, blue 6X loading dye (Fisher scientific) was added to the complex. Electrophoresis was carried out on a 2 % w/v agarose gel mixed with GelRed TM nucleic acid gel stain (Interchim, France) in 1X TBE buffer (90 mM Tris-borate/mM EDTA, pH 8.2). The gel was run in 0.5X TBE at 50V for 30'. A 100 bp DNA ladder from Sigma-Aldrich (Saint-Quentin-Fallavier, S4 France) was used as reference for the gel. The GelREd-stained siRNA was visualized using a TFX-20 M model-UV transilluminator (Vilber Lourmat, Mare-la-Vallée, France).

***In vitro* two-photon induced siRNA delivery**

MCF-7-Luc p19 were seeded at a density of 1000 cells per well in a 384 black multi-well glass-bottomed plate with a black polystyrene frame (Proteigene, France) one day before transfection. To control siRNA efficiency, transfection of siRNA was performed first with Lipofectamine RNAiMAX reagent (Invitrogen, France). Complex between anti-Luc siRNA and PMO–AMFA–APTES at a ratio of 1:50 (µL: µL) was freshly prepared and incubated for 1h at 37 °C for pairing. Then MCF-7-Luc cells were incubated for 18 h with the complex at 40 µg mL^{-1}. After incubation, the cells were submitted (or not) to laser irradiation using the Carl Zeiss Microscope (laser power input 3W). Half of the well was irradiated at 800 nm by three scans of 1.57 s duration in four different areas of the well. No supplementary scan can be performed without overlapping. A microscope objective lens (Carl Zeiss tenfold magnification/objective 0.3 EC Plan-Neofluar) was used to focus the laser beam. After 48h transfection, apoptosis efficacy was assessed by addition into the culture medium of luciferin (10^{-3} M, final concentration) purchased from Promega (France). Living cell luminescence was measured 10 min after by a multilabel plate reader CLARIOstar® at 562 nml. Results were corrected according to the following formula $Lum_{non\ irradiated} - 2\ (Lum_{non\ irradiated} - Lum_{irradiated})$,

where Lum is the luminescence emitted. Luciferase activity was normalized in accordance to the total number of living cells in each sample as determined by Hoechst assay.

Statistical analysis

Statistical analysis was performed using the Student's t test to compare paired groups of data. A p-value of <0.05 was considered to be statistically significant.

2.2. Results and discussion

Synthesis of PMO–AMFA–APTES nanoparticles

PMO–AMFA synthesis was already described in section 1.1 of this chapter. We then investigated their functionalization with APTES (Figure 13). APTES was grafted by silanization inside the pores of PMO–AMFA following a procedure already described by C. Mauriello Jimenez *et al.*[46] PMO–AMFA–APTES nanoparticles presented a hydrodynamic diameter of 360 nm (Figure 14A) and a positive value of zeta potential of 1.4 ± 0.2 mV. The positive value of zeta potential (pH =7) could be explained by the protonation of the amine groups on the surface and/or the pores of the nanoparticles. This charge reversal indicated the success of the grafting reaction. Potential release of AMFA after APTES grafting was verified by UV spectroscopy. Since these nanoparticles were to be used in gene delivery through an active endocytosis process already described, it was necessary to verify the stability of the AMFA molecules onto de NPs after the last coupling step. As it can be seen in Figure 14B, AMFA residues were not detected in the supernatant after the coupling reaction, confirming that no modification of the nanoparticle composition occurred.

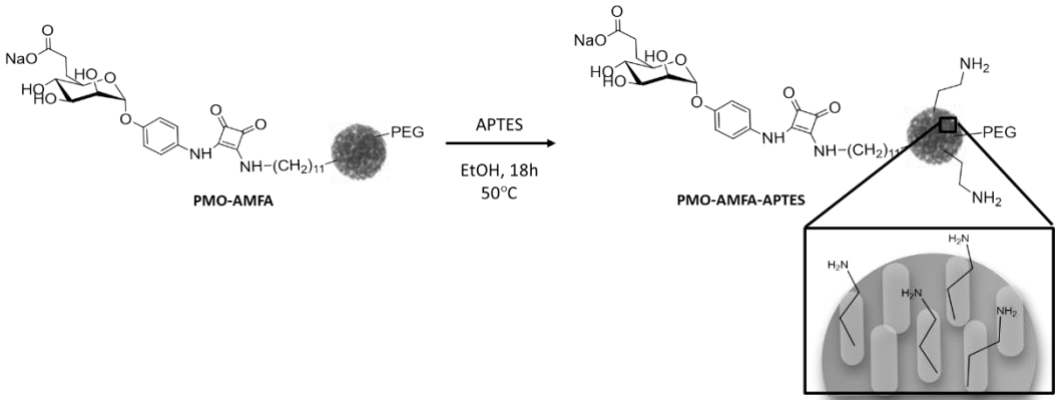

Figure 13. Synthesis of PMO–AMFA–APTES. Schematic representation of the grafting reaction to obtain PMO–AMFA–APTES.

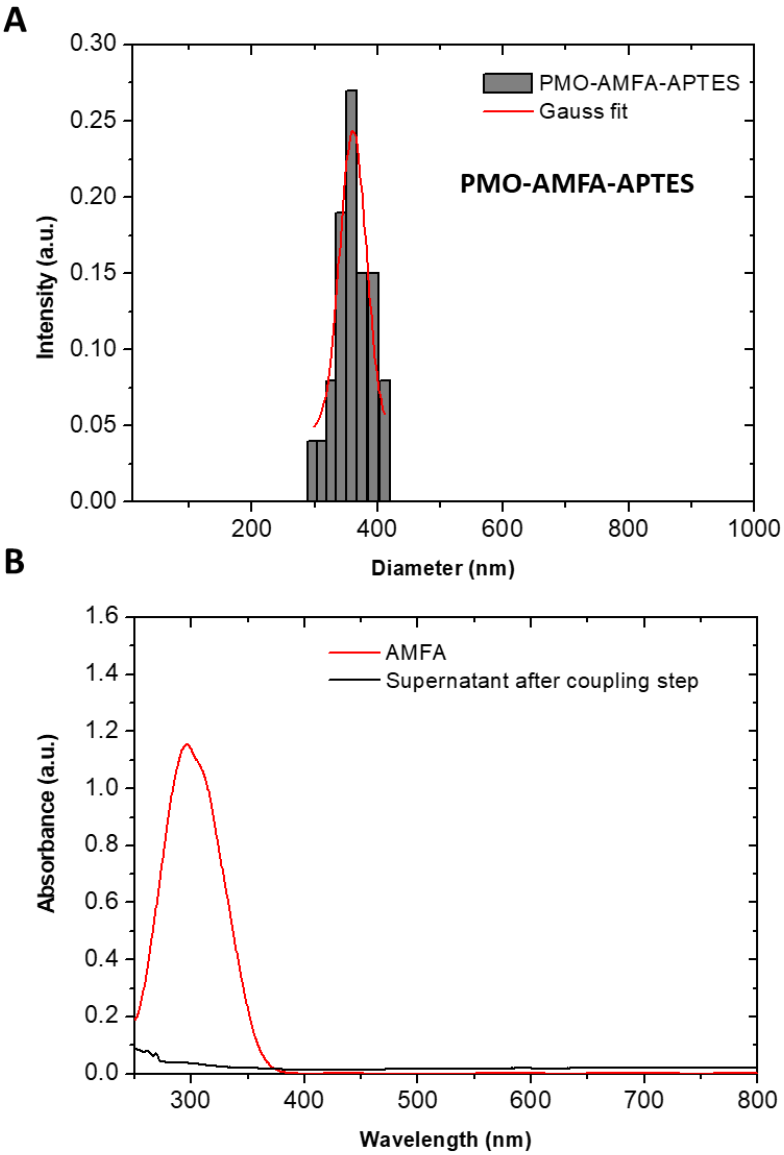

Figure 14. Characterizations of PMO–AMFA–APTES (A) DLS in intensity of PMO–AMFA–APTES. (B) UV-Vis spectrum of the supernatant after APTES grafting step.

Biocompatibility of PMO–AMFA–APTES on RMS-YM cell line

The cytotoxicity of PMO–AMFA–APTES was evaluated in RMS-YM cancer cells. Increasing concentrations of nanoparticles were added and incubated for 3 days. An increment of cellular death up to 30 % with NPs addition was observed until a concentration of 5 µg mL^{-1}. After this value, no significant toxicity was observed when NPs concentration was increased up to 100 µg mL^{-1}. Thus, 40 µg mL^{-1} was chosen for further biological experiments to be consistent with previous experiments.

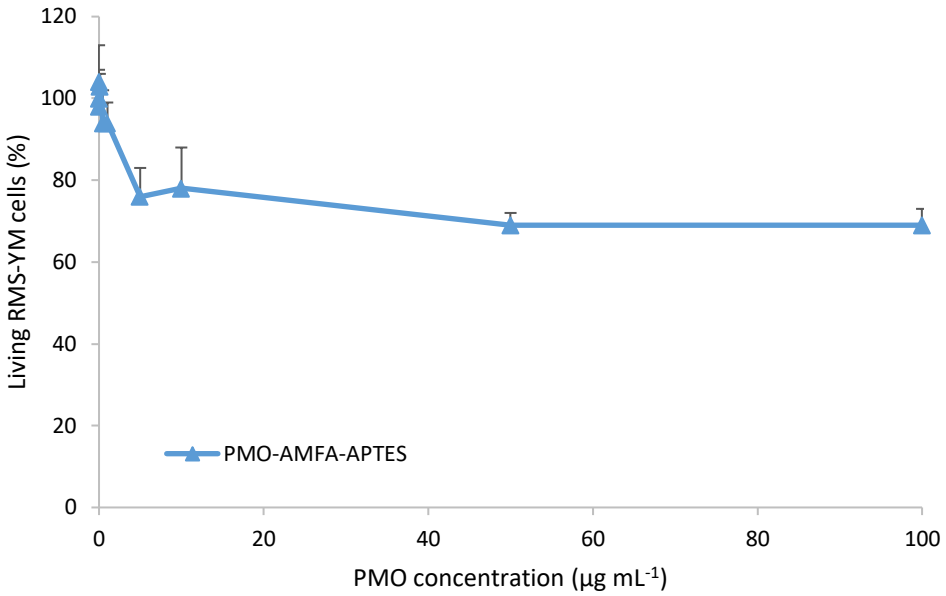

Figure 15. Cytotoxicity of PMO-AMFA-APTES on cancer cells. Cytotoxicity of PMO-AMFA-APTES on RMS-YM cells. Data are presented as mean ± SEM, of two independent experiments realized in triplicate.

Study of TPE-PDT

The efficacy of PMO–AMFA–APTES to target and kill MCF-7 cells under near-infrared two-photon excitation was assessed. MCF-7 cells were incubated with 40 µg mL^{-1} of PMO–AMFA–APTES for 16h and they were irradiated or not at 800 nm three times for 1.57 s at a maximal laser power. In the absence of laser irradiation, a certain mortality caused by toxicity of the nanoparticles themselves was observed. It is in agreement with the values presented in the plot describing the cytotoxicity. Two methods were used to quantify cell viability after TPE-PDT: In the case of using the MTT method (Figure 16A), an underestimation in the percentage of living cells was observed. The orange coloration of PMO–AMFA–APTES hampered and distorted the spectroscopic quantification of the living cells. According to this method, neither PMO–AMFA, which were already proved effective, nor PMO–AMFA–APTES induced any significant phototoxicity on cancer cells. Due to this inconsistent result, the Hoechst method was tested (Figure 16B). For PMO–AMFA, the results were consistent with previous experiences. PMO–AMFA–APTES induced 67 % MCF-7 cell death, being significantly effective against cancer cells. In addition, this result showed that the addition of APTES did not affect R6MP reconnaissance; these nanoparticles continue to be specific for targeting membrane receptors and for TPE-PDT.

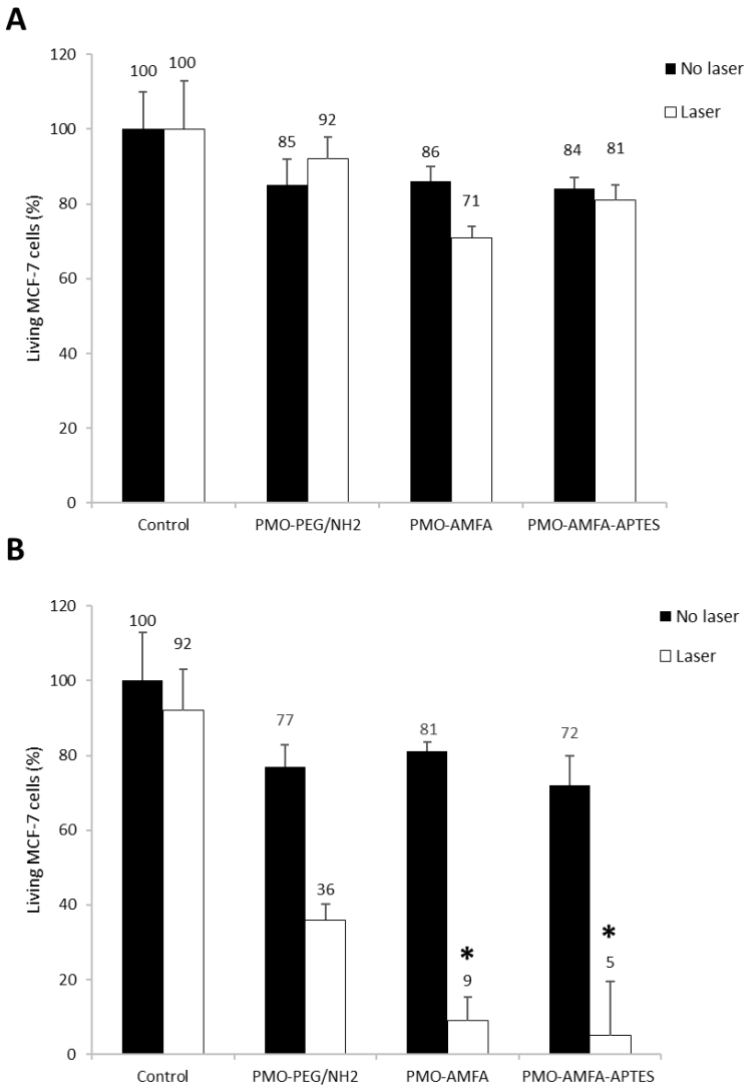

Figure 16. TPE-PDT with PMO-AMFA-APTES. (A) Human breast cancer cells (MCF-7) were incubated for 16h with PMO-AMFA-APTES (40 μg mL^{-1}) and irradiated at 800 nm (3 × 1.57 s). Cell death was assessed after 2 days by the MTT reagent. (B) Human breast cancer cells (MCF-7) were incubated for 16h with PMO-AMFA-APTES (40 μg mL^{-1}) and irradiated at 800 nm (3 × 1.57 s). Cell death was assessed after 2 days and nuclear staining with Hoechst 33345. Data are mean values ± standard deviations from three independent experiments. *Statistically significant versus non-irradiated PMO ($p < 0.05$ from the Student's t test).

In vitro two-photon induced siRNA Delivery

The complexation efficiency of PMO–AMFA–APTES was evaluated. Complexes between PMO–AMFA–APTES and siRNA at three ratios siRNA/NPs were tested (1/5, 1/20, and 1/50). No complexation was observed at a ratio of 1/5. A decrease in the intensity of the band at a ratio 1/20 was observed (Figure 17), and it became clearer at a ratio of 1/50. This suggested a partial complexation beyond 1/20 and an almost complete complexation at a ratio

of 1/50. Consequently, the ratio of 1/50 was chosen for further experiments. The halos observed inside the last two wells (yellow rectangle) are a sign of the successful complexation between the NPs and the siRNA, indicating that the siRNA got efficiently complexed.

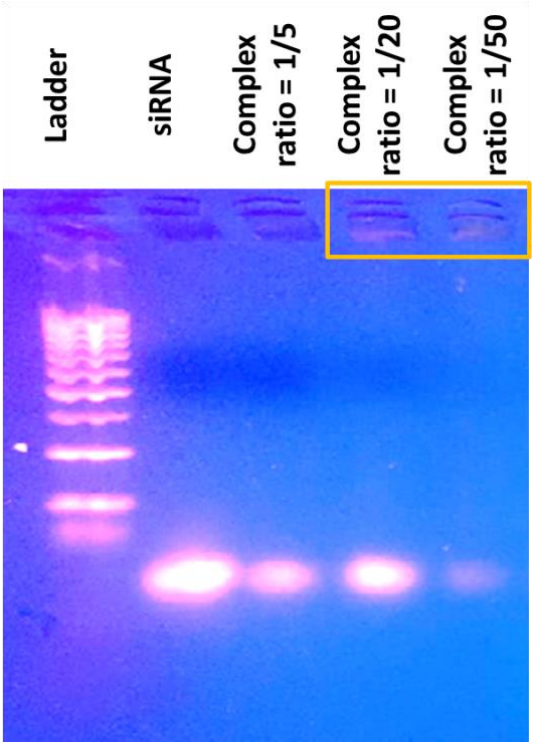

Figure 17. Gel retardation assay. siRNA and complexes at different ratios (1/5, 1/20, and 1/50) were migrated to evaluate the complexation efficiency of PMO–AMFA–APTES. Sign of complexation inside the yellow rectangle.

Then the delivery of siRNA induced by two-photon trigger was examined. As a proof of concept, luciferase-expressing MCF-7 breast cancer cells and anti-Luc siRNA were used. The complex between PMO–AMFA–APTES and siRNA targeting the luciferase gene at 40 µg mL^{-1} was incubated with MCF-7-Luc for 18h at RT. The addition of the lipofectamine helped to corroborate that siRNA was not deactivated along with the transfection experiments. Lipofectamine forces the siRNA to enter into cells inducing the silencing effect, which is not normally caused just by free siRNA. It was observed that siRNA alone induced a slight decrease in luminescence when incubated with MCF-7-Luc cells, probably due to the membrane destabilization caused by the TPE, allowing its subsequent entrance into the cytoplasm (Figure 18). In contrast, diminution of the luminescence was increased to 57% when the siRNA was immobilized onto the NPs. On one hand, nanoparticles facilitated the protection of the siRNA, avoiding its degradation and ensuring an efficient delivery to the cell. On the other hand, laser irradiation triggered the activation of the PS, which produced ROS responsible for endosomes-

lysosomes membranes disruption. This membrane destabilization contributed to the release of the endocytosed siRNA to the cytoplasm by a mechanism of PCI, where they may further translocate in the cytosol or to the nucleus.

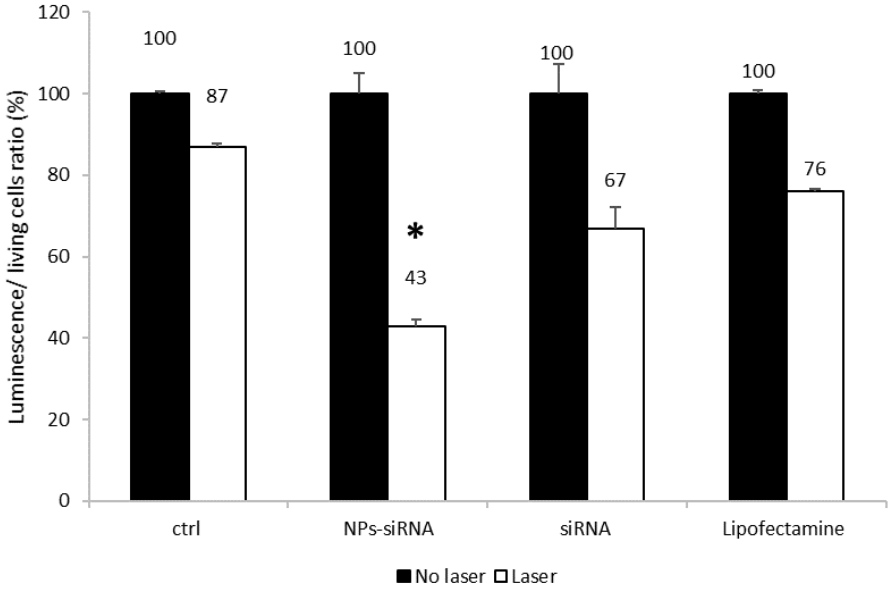

Figure 18. TPE-triggered siRNA delivery. Luciferase-expressing MCF-7 breast cancer cells were incubated with PMO–AMFA–APTES (40 μg mL^{-1}) and irradiated at 800 nm (3 × 1.57 s). Cell death was assessed after 2 days and nuclear staining with Hoechst 33345. Data are mean values ± standard deviations from three independent experiments. *Statistically significant versus non-irradiated PMO ($p < 0.05$ from the Student's t test).

2.3. Conclusions

The synthesis and the complexation capability of PMO–AMFA–APTES were described. After the grafting step, these nanoparticles have shown acceptable biocompatibility even a high concentration and the inclusion of APTES did not affect R6MP recognition. They maintained suitable efficiency in cancer cells targeting and in TPE-PDT *via* an active endocytosis mechanism. In addition, we assessed the potential of PMO–AMFA–APTES to be used in gene therapy. First attempts on MCF-7-Luc have shown the ability of these nanoparticles to deliver Anti-Luc siRNA *via* PCI mechanism using TPE, generating a remarkable silencing effect of the luciferase with the inhibition of the luminescence.

2.4. Perspectives

First, it will be necessary to evaluate the effect of targeted TPE-PDT *in vitro* onto RMS-YM cells, which is the cancer of study, using PMO–AMFA–APTES. MCF-7 cells were used as a model because they are easier to culture and allow to test the active targeting mechanism. It was already shown in the bibliography that MCF-7 overexpressed M6RP on their surface.[238] Second, the promising preliminary results achieved in gene inhibition should be optimized to improve the silencing effect caused by the complex PMO–AMFA–APTES@Anti-Luc siRNA. Once the protocol will be properly established, we intend to perform gene delivery in RMS cells to trigger the inhibition of PAX3-FOXO1, which is a transcription factor involved in the tumorigenesis of the most aggressive forms of RMS.

CHAPTER 3: pSiNPs as a platform for cancer theranostics

The aim of this chapter is to describe the use of pSiNPs as a platform for cancer theranostics. These nanoparticles have been used as PS in two-photon excitation photodynamic therapy because they are capable of absorbing light in the near-infrared generating $^1O_2$, and due to their large specific surface, they could load different molecules inside their pores as well as on their surface. These cargoes include therapeutic molecules like drugs or target molecules such as carbohydrates, peptides, or antibodies, which aid in the active endocytosis process for the NP uptake by the tumor cells. [134, 239]

- The first part of the chapter describes the functionalization of pSiNPs with a specific peptide (conotoxin) capable of targeting a membrane receptor (Fetal acetylcholine receptor) of RMS. The subcellular localization of these nanoparticles is presented.

- In the second part, we detail the functionalization of pSiNPs with a cationic porphyrin to enhance their ROS generation, and an analog of mannose-6 phosphate, capable of targeting another membrane receptor (RM6P-CI) overexpressed in RMS cells. Their efficacy in TPE-PDT on RMS cells is described.

- In the last part of the chapter, pSiNPs bearing ICPES-azobenzene@Lys has been employed in gene (siRNA) transfection triggered by bi-photonic excitation light. Transfection efficacy studied on MCF-7-luc cells is presented.

Part I. Rhabdomyosarcoma imaging by pSiNPs

Introduction

Rhabdomyosarcoma (RMS) is the most common sarcoma in children and represents the third most common extracranial solid tumor among pediatric cancers, after Wilm's tumor and neuroblastoma.[240-241] Current treatments involving chemotherapy (highly aggressive multidrug regimen [242]), surgery or radiotherapy, do not allow to improve the prognosis of RMS. Therefore, novel strategies based on treatments developed to act against specific tumor receptors are required.

Some examples of targeted therapies for pediatric tumors are already reported in the bibliography. Loi *et al* described liposomes bearing peptides for neuroblastoma (NB) targeting. They showed how these nanocarriers counteract NB progression in animal models, with a considerable improvement in their therapeutic efficacy, compared to both free drug and untargeted systems.[243] Pastorino and colleagues synthesized aGD2-immunoliposomes encapsulating DXR. They showed the targeting effectiveness and preferential cytotoxicity against GD2-positive NB cells *in vitro*, but also the total inhibition of metastatic growth of human NB in a xenograft model of nude mice.[244] In the case of RMS, several works have been centered on targeting the receptors tyrosine kinases, such as IGF1R[35], EGFR, or FGFR4[245]. The significant expression of the fetal acetylcholine receptor (fAChR) in RMS compared to normal tissues, was also proposed as a diagnostic marker for this tumor.[153] Associated with this receptor, Teichert and coworkers described a peptide toxin from the venom of the marine cone snail, showing the capacity of inhibiting the mammalian fAChR.[156]

Porous silicon nanoparticles (pSiNPs) offer benefits over other inorganic nanoparticles for their use as vehicles *in vitro* and *in vivo* applications.[246-247] They are particularly interesting because they are fully resorbable *in vivo* into non-toxic by-products such as oxyanions of orthosilicic acid ($Si(OH)_4$).[248] Orthosilicic acid is absorbed from the diet and it is naturally found in numerous tissues and efficiently excreted by the kidneys.[95] Furthermore, they present other properties such as high surface area[249], tunable pore diameter [249], high loading capacity, and they exhibit intrinsic photoluminescence, appropriate for imaging applications.[94] Here, we describe how we have taken advantage of these characteristics to functionalize pSiNPs with a PS and with the conotoxin to effectively target fAChR and monitor cellular uptake by RMS cancer cells.

1.1. Experimental part

Materials

Hydrofluoric acid (HF, 48%), N,N-Dimethylformamide (DMF, anhydrous 99.8%), 1-Pyrenecarboxaldehyde (99%), Allylamine (98%), Dichloromethane (DCM, anhydrous ≥99.8%) and Acetate buffer were purchased from Sigma-Aldrich. Ethanol (EtOH, 100%) was purchased from VWR. O-(undec-10-en-1-yl)-hydroxylamine was purchase from SIKEMA. Boron-doped p++-type Si (0.8-1.2 mΩ.cm resistivity, <100> orientation) was purchased from Siltronix (France). Conopeptide (sequence CCGVONAACPOCVCNKTCG) was modified by Melnyk *et al.* [250-251]

Analytical techniques

^{1}H and ^{13}C solution NMR spectra were recorded on a Bruker AC 400 spectrometer. Chemical shifts (in δ units, ppm) are referenced to TMS using residual DMSO-d_6 (δ = 2.50 ppm) resonance as the internal standard for ^{1}H NMR spectra, and DMSO-d_6 (δ = 39.52 ppm) for ^{13}C NMR spectra. UV-vis absorption spectra were recorded on a Hewlett-Packard 8453 spectrophotometer using correction factors supplied by the manufacturer. TEM analysis was performed on a JEOL 1200 EXII instrument. Dynamic light scattering analyses were performed using a Cordouan Technologies DL 135 Particle Size Analyzer instrument and analyzed with NanoQ software. IR spectra were recorded on a PerkinElmer 100 FT spectrophotometer. Zeta potential measurements were performed with a Malvern Zetasizer NanoSeries Instrument (pH = 7, NaCl 5 mM). N_2 adsorption isotherms were measured using a TRISTAR 3000 gas adsorption analyzer instrument, and the specific surface area was determined using the BET method.

Nanomaterials synthesis and characterization

Synthesis of 5-(4-iso-thiocyanatophenyl)-10,15,20-tris(4-N-1-methyl-4-pyridinio) porphyrin triiodide

The water-soluble 5-(4-iso-thiocyanatophenyl)-10,15,20-tris(4-N-1-methyl-4-pyridinio) porphyrin triiodide was prepared according method described by J. M. Sutton *et al.*[252] Succinctly, 5-(4-acetamidophenyl)-10,15,20-tri-(4-pyridyl)-porphyrin was obtained by Adler condensation. 5-(4-aminophenyl)-10,15,20-tri-(4-pyridyl)-porphyrin prepared from 5-(4-acetamidophenyl)-10,15,20-tri-(4-pyridyl)-porphyrin by acid hydrolysis (HCl 5 N), was

converted to 5-(4-iso-thiocyanatophenyl)-10,15,20-tri-(4-pyridyl)-porphyrin then methylated by methyl iodide.

Synthesis of pSiNPs

Boron-doped p++-type Si was electrochemically etched in a 3:1 (v:v) solution of aqueous 48% hydrofluoric acid (HF):absolute ethanol. Etching was performed in a Teflon cell with a platinum ring counter electrode. A constant current of 179 mA cm^{-2} was applied for 160 s, and the sample was rinsed 3 times with absolute ethanol. The porous layer was then removed from the substrate by application of a constant current of 1.57 mA cm^{-2} for 240 s in an electrolyte solution containing 1:13.5 (v:v) aqueous 48% hydrofluoric acid: absolute ethanol. After 3 rinses with absolute ethanol, the porous layer was placed in ethanol in a glass vial. After degassing the sample for 20 min under a nitrogen stream, the porous silicon film was fractured by ultrasonication during 21 h (Ultrasonic cleaner Fisher Transsonic TI-H-10). The largest particles were removed by spinning them down by centrifugation at 3 000 rpm for 3 min. In order to remove the smallest particles, the solution was finally centrifuged at 14 000 rpm for 30 min. The pellet was then redispersed in absolute ethanol.

Vinylation of the 5-(4-Isothiocyanatophenyl)-10,15,20-tri-(4-N-methylpyridinio)-porphyrin triiodide

Under inert atmosphere, allylamine was added to a mixture of 5-(4-Isothiocyanatophenyl)-10,15,20-tri-(4-N-methylpyridinio)-porphyrin triiodide in DCM/DMF (1:1). The mixture was stirred 20h at RT in presence of NEt_3 in catalytic amounts. After solvent evaporation, the residue was washed several times with hexane, and then dried under vacuum.

O-(undec-10-en-1-yl)-hydroxylamine grafting onto pSiNPs by hydrosilylation

Freshly prepared pSiNP were centrifuged at 14 000 rpm for 20 minutes in ethanol, then 37 mg of pSiNP were redispersed in 1 mL of O-(undec-10-en-1-yl)-hydroxylamine and reacted for 1h (to avoid total functionalization) at 70°C under inert atmosphere. Once the reaction is finished, the pSiNPs–ONH_2 were centrifuged at 14 000 rpm for 20 minutes and washed three times with absolute ethanol to remove the O-(undec-10-en-1-yl)-hydroxylamine adsorbed onto their surface. The pSiNPs–ONH_2 were finally redispersed in 10 mL ethanol.

Vinyl porphyrin grafting onto pSiNPs–ONH_2

1 mg of vinyl porphyrin solution (2 mg/mL) in EtOH/DMF (1:1) was added to 35 mg of pSiNPs–ONH_2, previously centrifuged at 14 000 rpm for 20 minutes. The reaction was kept under stirring for 2 h at 70°C. Thereafter, the mixture was centrifuged at 14 000 rpm for 20 minutes and washed three times with absolute ethanol. The pSiNPs–ONH_2–porphyrin were finally redispersed in 10 mL ethanol.

1-Pyrenecarboxaldehyde grafting onto pSiNPs–ONH_2–porphyrin

16 mg of pSiNPs–ONH_2–porphyrin were centrifuged at 14 000 rpm for 20 minutes. After removing the EtOH, 1 mL of a solution 0.1 mM of 1-Pyrenecarboxaldehyde in acetate buffer/DMF (pH = 5) was added. The reaction was kept under stirring for 18 h at 37°C. After the reaction, the mixture was centrifuged at 14 000 rpm for 40 minutes and washed three times with absolute ethanol to remove the 1-Pyrenecarboxaldehyde adsorbed on their surface. The pSiNPs–pyrenecarboxaldehyde–porphyrin were finally redispersed in 10 mL ethanol.

Conopeptide grafting onto pSiNPs–ONH_2–porphyrin

6 mg of pSiNPs–ONH_2–porphyrin were centrifuged at 14 000 rpm for 20 minutes. After removing the EtOH and dispersion of the pSiNPs–ONH_2–porphyrin in 4.3 mL of buffer, 970 µL of a solution 1 mg/mL of Conopeptide (OIVB) in acetate buffer/DMF (pH = 5) was added. The reaction was kept under stirring for 48 h at 37°C. Afterward, the mixture was centrifuged at 14 000 rpm for 20 minutes, and the nanoparticles were washed three times with buffer solution. The pSiNPs–conopeptide–porphyrin were finally redispersed in 10 mL ethanol.

Biological studies

Cell culture

RMS-YM cells from ATCC were cultured in RPMI-1640 medium supplemented with 10% FBS and 1% penicillin/streptomycin and were allowed to grow in a humidified atmosphere at 37 °C under 5% CO_2.

Two-photon fluorescence imaging

RMS-YM cells were grown on a tissue culture dish with cover glass bottom (FluoroDish from WPI) in complete culture medium. The cells were incubated or not with pSiNPs, pSiNPs–ONH_2–porphyrin and pSiNPs–porphyrin–conopeptide (50 µg mL^{-1}) for 24 h. Fifteen minutes before the end of incubation, cells were loaded with green Cell Mask (5 µg mL^{-1}, Invitrogen)

for membrane staining. Before visualization, cells were washed three times with cell media. Cells were examined under an LSM 780 live confocal microscope (Carl Zeiss Microscope), and excited at 561 nm for membranes and at 800 nm for nanoparticles. All images were performed with a high magnification (63×/1.4 OIL DIC Plan-Apo).

Statistical analysis

Statistical analysis was performed using the Student's t test to compare paired groups of data. A p-value of <0.05 was considered to be statistically significant.

1.2. Results and discussion

O-(undec-10-en-1-yl)-hydroxylamine grafting onto pSiNPs by hydrosilylation

pSiNPs were first synthesized following the protocol described in the experimental section. We obtained nanoparticles with a hydrodynamic diameter of 276 nm and zeta potential of -21.4 ± 0.5 mV. We then investigated their functionalization with O-(undec-10-en-1-yl)-hydroxylamine by hydrosilylation through the silicon hydride (Si-H) available on the siNPs surface (Fig. 19A), according to a method we published in 2016.[138] pSiNPs– ONH_2 presented a hydrodynamic diameter of 277 nm and zeta potential of -4.61 ± 1.28 mV (Figure. 19B). Covalent grafting of O-(undec-10-en-1-yl)-hydroxylamine onto pSiNPs was confirmed by infrared spectroscopy. Figure 19C showed FTIR spectra of pSiNPs and pSiNPs– ONH_2. The band between 1000 and 1200 cm^{-1} was assigned to the stretching vibration mode of Si-O bonds, indicating the partial oxidation of pSiNPs surface. The disappearance of the stretching band of Si-H at 2100 cm^{-1} (Spectrum of pSiNPs) and the appearance of the asymmetric and symmetric stretching vibration mode of aliphatic carbons (ν_{CH2}) between 2996 and 2880 cm^{-1} (Spectrum of pSiNPs–ONH_2) confirmed the coupling of the O-(undec-10-en-1-yl)-hydroxylamine onto the pSiNPs. Between 1500 and 1300 cm^{-1} the asymmetric and symmetric bending modes of alkanes (δ_{CH2}) were detected. Another representative band, which also helped to confirm the grafting, was the stretching vibration mode of the N-H bond from the hydroxylamine at 3300 cm^{-1}.

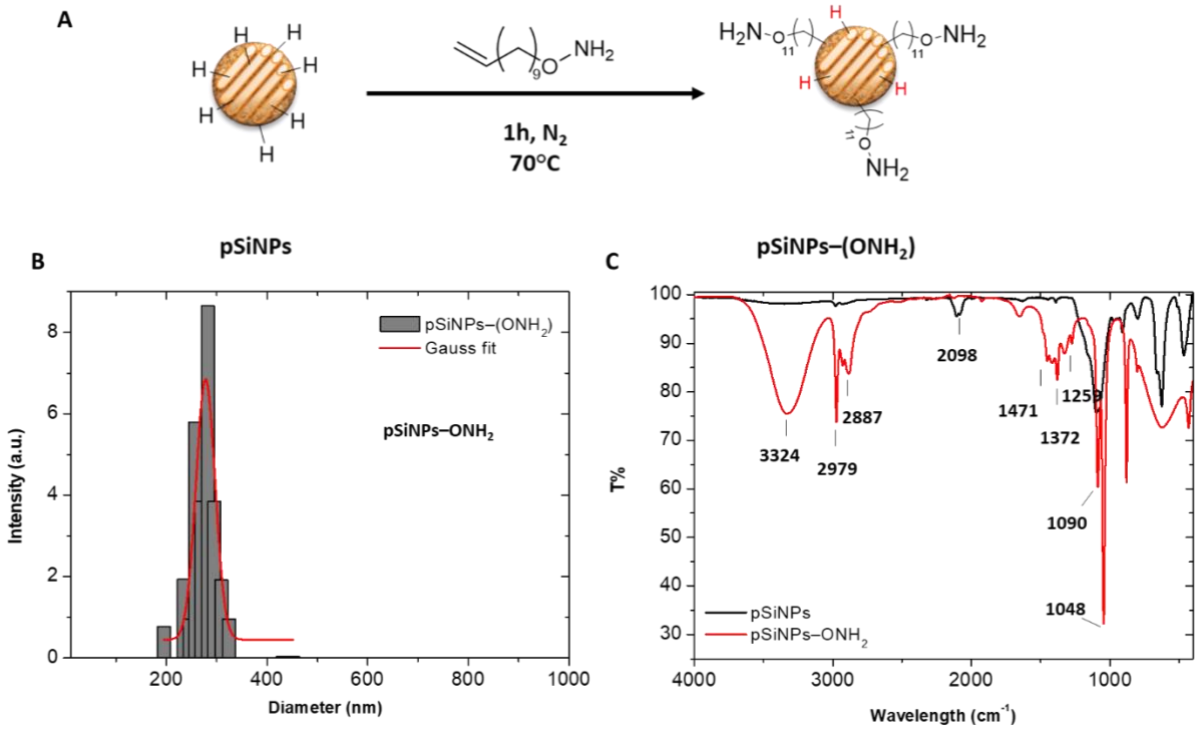

Figure 19. Synthesis and characterization of pSiNPs–ONH₂. (A) Schematic representation of the hydroxylamine grafting to obtain pSiNPs–ONH₂. (B) DLS in intensity of pSiNPs–ONH₂. (C) Infrared spectra of pSiNPs (black line) and pSiNPs–ONH₂ (red line).

Cationic porphyrin grafting onto pSiNPs–ONH₂

5-(4-iso-thiocyanatophenyl)-10,15,20-tris(4-N-1-methyl-4-pyridinio) porphyrin triiodide (porphyrin-NCS) was synthesized, and modified with a vinyl arm following the protocol described in the experimental section (Figure 20A). The vinyl arm allowed the reaction between the porphyrin and the pSiNPs–ONH₂, by hydrosilylation chemistry leading to a covalent attachment of the porphyrin on the surface of the pSiNPs. These pSiNPs–ONH₂–porphyrin presented a hydrodynamic diameter of 326 nm and zeta potential of -7.7 ± 2.7 mV. The effective grafting of the porphyrin derivative was confirmed by the UV-Vis spectroscopy of pSiNPs–ONH₂–porphyrin (figure 20C). The characteristic Soret band and two Q bands of the porphyrin appeared at 440 nm and between 560 and 650 nm, respectively.

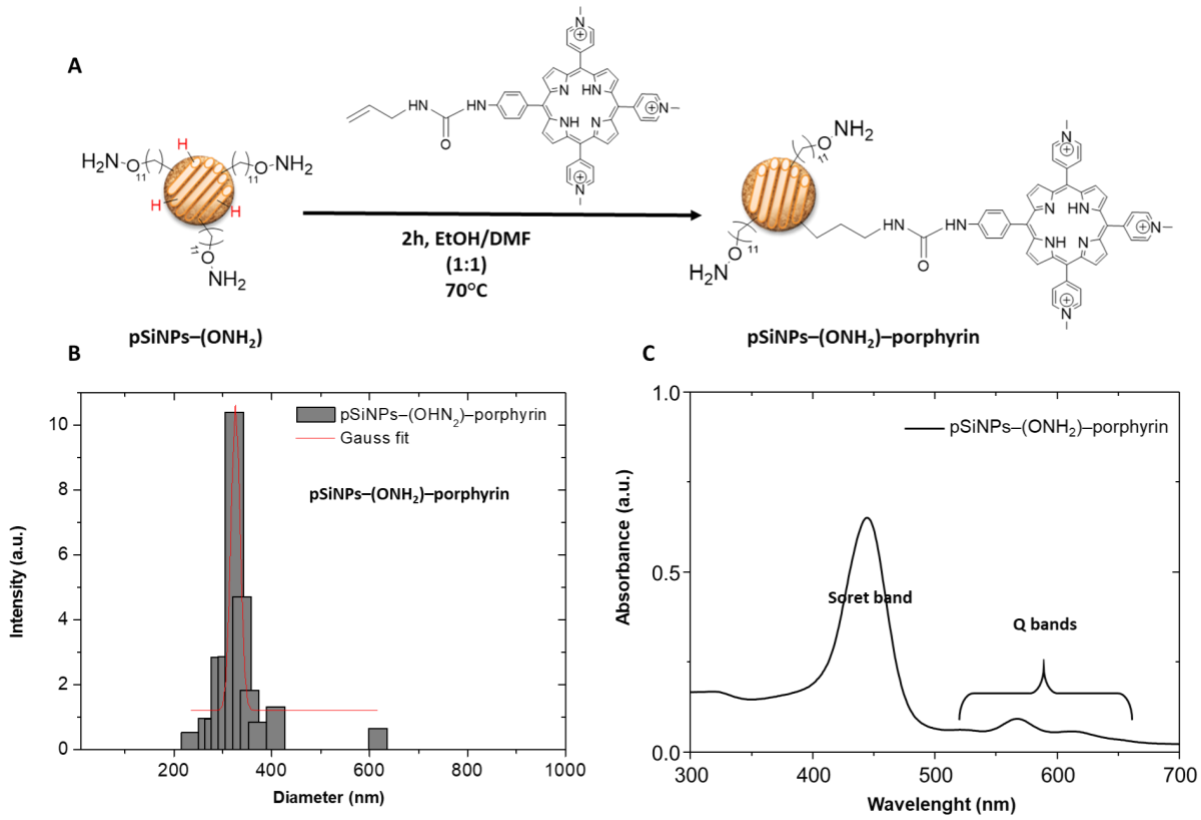

Figure 20. Synthesis and characterization of pSiNPs–ONH_2–porphyrin. (A) Schematic representation of the porphyrin grafting to obtain pSiNPs–ONH_2–porphyrin. (B) DLS in intensity of pSiNPs–ONH_2–porphyrin. (C) UV-Vis absorbance spectrum of pSiNPs–ONH_2–porphyrin.

1-Pyrenecarboxaldehyde grafting onto pSiNPs–ONH_2–porphyrin

1-Pyrenecarboxaldehyde was grafted on pSiNPs–ONH_2–porphyrin according to the protocol described in the experimental part. We used this chromophore for testing peptide-grafting conditions. Hydroxylamine groups (–ONH_2) selectively binds aldehydes or ketones in acidic conditions, consequently in this case, the reaction between –ONH_2 and the aldehyde took place leading to an oxime bond formation. (Figure 21).

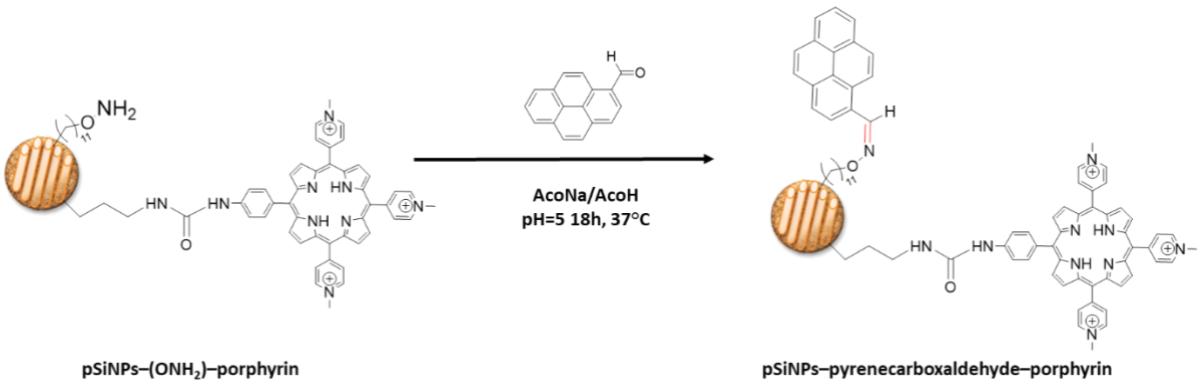

Figure 21. Schematic representation of the 1-Pyrenecarboxaldehyde grafting to obtain pSiNPs–pyrenecarboxaldehyde–porphyrin.

The UV-Vis spectra of pSiNPs—pyrenecarboxaldehyde—porphyrin and 1-pyrenecarboxaldehyde were showed in Figure 22. Comparing both spectra, the characteristic bands of the chromophore (≈ 278, 285, 348, and 363 nm) were observed in the spectrum of pSiNPs—pyrenecarboxaldehyde—porphyrin, confirming the successful grafting of the chromophore onto the pSiNPs.

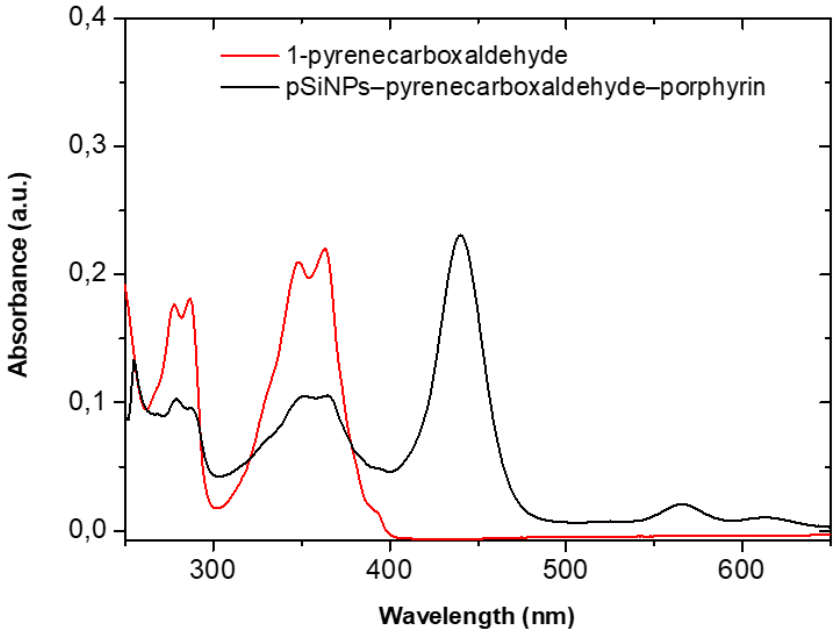

Figure 22. UV-Vis spectra of 1-pyrenecarboxaldehyde (red line) and pSiNPs—pyrenecarboxaldehyde—porphyrin (black line).

The grafting conditions to bond the peptide were successfully established. The hydroxylamine allowed efficiently to attach the chromophore, proving that oxime bond is suitable for peptide grafting.

Conopeptide grafting onto pSiNPs–ONH_2–porphyrin and study of the internalization of pSiNPs–conopeptide–porphyrin

The conotoxin peptide was synthesized by Dr Oleg Melnyk's group (Institut de Biologie/Institut Pasteur Lille). The active sequence is CCGVONAACPOCVCNKTCG, where O is a hydroxyproline. [253] Dr O. Melnyk's group developed an innovative approach for accessing the folded conopeptide, whose production by classical methods is extremely low yielding. The key is to reversible modify the N-terminal cysteine produced by conventional solid phase peptide synthesis by an acetoacetyl group (AcAc), [250] a modification that dramatically simplifies the disulfide pattern distribution upon folding. Indeed, two conformations (OIVBpic1 and OIVBpic2) were obtained. The covalent grafting of the conopeptide (AcAcOIVBpic2) to the pSiNPs–ONH_2–porphyrin was described in the experimental section. The oxime bond was formed after the reaction between the –ONH_2 and the acetoacetyl group present in the peptide (Figure 23).

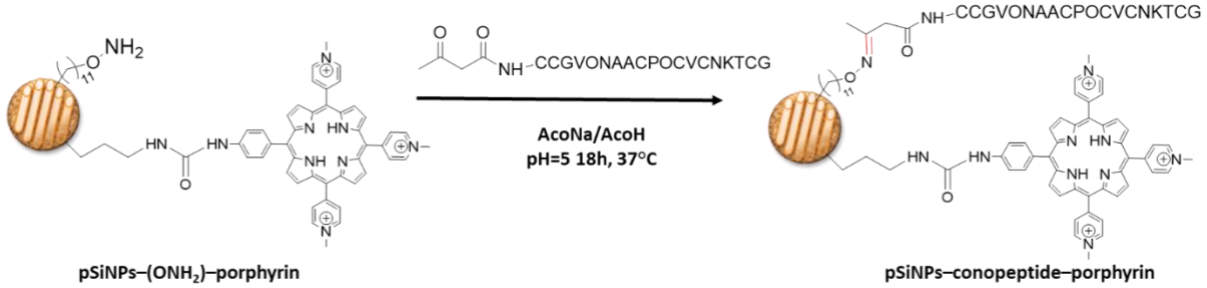

Figure 23. Schematic representation of the conopeptide grafting to obtain pSiNPs–conopeptide–porphyrin.

The pSiNPs–conopeptide–porphyrin presented a zeta potential of -3.6 ± 1.5 mV. To study the subcellular localization of pSiNPs–conopeptide–porphyrin and verify fAChR involvement in the active endocytosis, confocal imaging experiments on RMS-YM cells were performed. Figure 24 showed confocal images of RMS-YM cells incubated with pSiNPs, pSiNPs–ONH_2–porphyrin, and pSiNPs–conopeptide–porphyrin. Cell membranes appeared in green and pSiNPs in red.

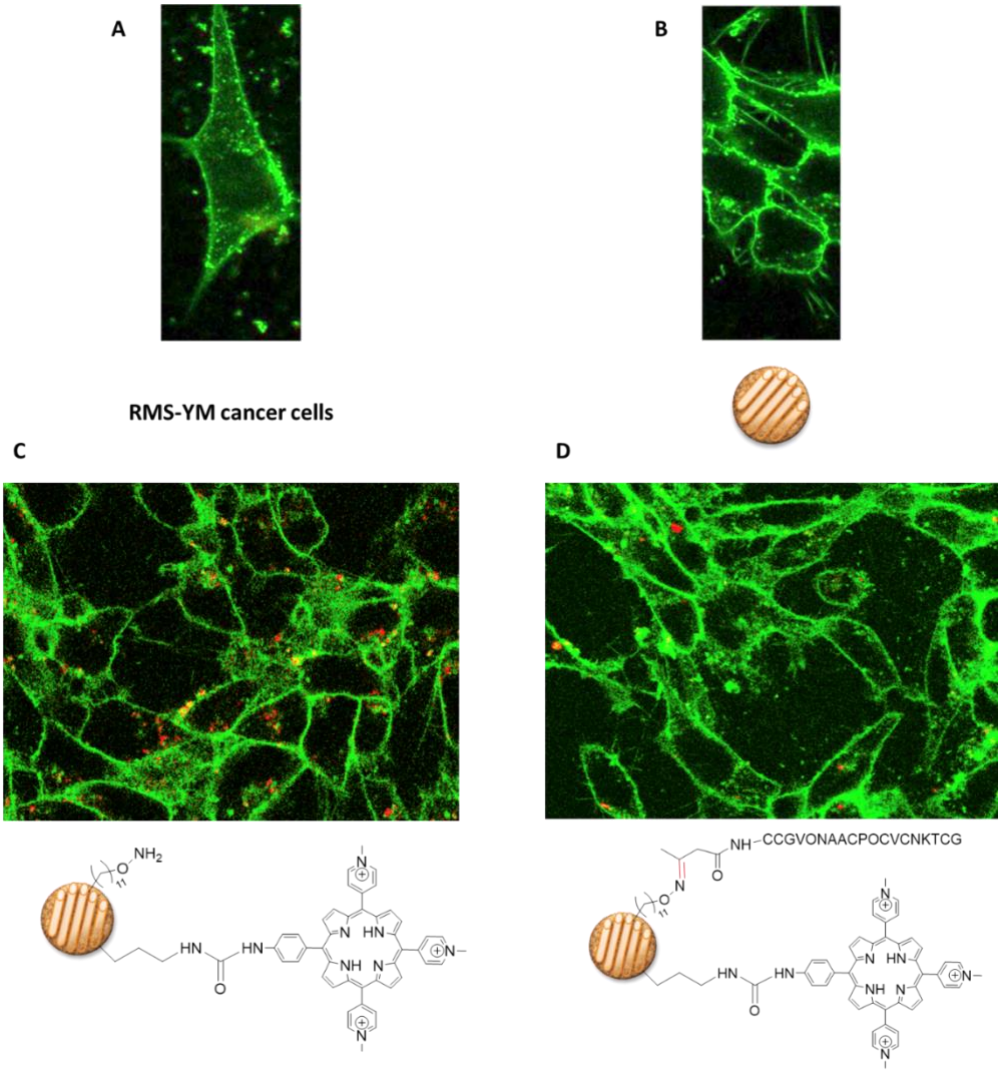

Figure 24. Nanoparticles internalization in RMS-YM cells. Confocal imaging on living cells in the presence of Cell mask (membranes stained in green) after 24 h of incubation time. (A)RMS-YM cells as control (B) pSiNPs (as control) (C) pSiNPs–ONH_2–porphyrin, and (D) pSiNPs–conopeptide–porphyrin.

We observed that pSiNPs–ONH_2–porphyrin without peptide were internalized through endocytosis. The luminescence observed was attributed to the porphyrin after energy transfer from the pSiNp to the porphyrin under NIR-TPE at 800 nm. Unexpectedly, the pSiNPs grafted with the peptide were weakly internalized in the cells. It seems that the endocytosis of the NPs was blocked, and they remained in the cell membrane. In order to understand this result, we performed a ligand-binding assay. This study allowed to verify the affinity of the different formulations for the fAChR receptor. A plot representing the percentage of response as a function of the peptide concentration is displayed in Figure 25. Four formulations were tested: two conformations of the conopeptide (OIVBpic1 and OIVBpic2) and two conformations of acetoacetyl-conopeptide (AcAcOIVBpic1 and AcAcOIVBpic2). The acetoacetyl function allowed peptide grafting onto the pSiNPs.

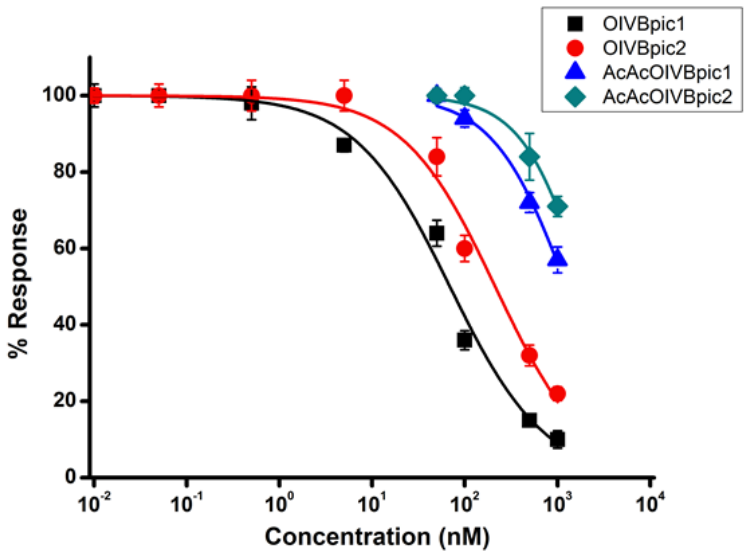

Figure 25. Dose response curve for the four different formulations.

At the same concentration (10^3 nM), we observed an inhibition of 90% caused by OIVBpic1 and an inhibition of 75% caused by OIVBpic2. However, the introduction of the acetoacetyl function provoked a diminution in the inhibition capability, obtaining only 40% of inhibition with AcAcOIVBpic1 and 30% inhibition with AcAcOIVBpic2 (peptide used in the grafting). The introduction of the chemical group makes the peptide loose its affinity for the receptor.

1.3. Conclusions

We have described the synthesis of different nanoparticle formulations bearing a photosensitizer and a target peptide (pSiNPs–ONH_2–porphyrin, and pSiNPs–conopeptide–porphyrin). Biological studies showed that the nanoparticles were stable enough when incubated for 24 hours in RMS cells. The average incubating time for other types of porous silicon-based nanoparticles being 5 hours.

According to the bibliography (section 2.2.2 of chapter 1), there is an overexpression of fAChR in RMS-YM cells compared to healthy cells. Therefore, we decided to evaluate the active endocytosis of pSiNPs–conopeptide–porphyrin involving this receptor. Internalization results in RMS-YM cells were not conclusive; membrane receptor recognition by the peptide was not ensured. In addition, the introduction of the acetoacetyl group to attach it to the pSiNPs provoked a reduction of the inhibition capability of the conopeptide.

1.4. Perspectives

We may consider developing another strategy for attaching the conopeptide to the nanoparticles, such as another chemical function. Aminooxy acetyl group will be preferred because of its improved reactivity.

Part II. The mannose 6-phosphate receptor targeted with pSiNPs for rhabdomyosarcoma theranostics

Introduction

The association of two-photon excitation photodynamic therapy (TPE-PDT) and nanoparticles offers several advantages in the treatment of cancer among other illnesses, being nowadays an important research area in cancer treatments. On one hand, photodynamic therapy, which was already described in section 2.3 of chapter 1, allows a more localized and less invasive treatment diminishing the side effects induced by conventional treatments. The photosensitizer (PS), which is administrated either systemically, locally, or topically, is illuminated with appropriate irradiation. Under irradiation, the PS transfer its energy to the surrounding oxygen (in its triplet state) which generate singlet oxygen and other cytotoxic species that conduct to cell death. [254-255] On the other hand, the employment of nanoparticles makes it possible to overcome certain inherent limitations of the PS used in PDT such as poor pharmacokinetic profile and low specificity for tumors. Then, the use of NPs as vehicles can protect the PS during systemic circulation and facilitate the selective accumulation at the tumor site. [255]

Gold nanorods, CdSe, or Qdots are examples of inorganic nanoparticles used in TPE-PDT however, they present limitations in terms of toxicity[256-258] and non-biodegradability[259]. Porous silicon nanoparticles (pSiNPs) emerge as an appropriate substitute because they have already shown their suitability for other biological applications such as drug delivery, [102, 260] and can be excited by two-photon near infrared light. [94] Xiao and colleagues first showed the use of pSiNPs for singlet oxygen production and PDT. After irradiating HeLa and NIH-3T3 cells incubated with pSiNPs with a 60 J/cm^2 white light for 10 min, a 45% cell death was observed. Control assay with the same cells in absence of nanoparticles showed between 10 – 25 % of cell death.[261] Nevertheless, the PDT efficacy could be improved not only by the attachment of PSs to the nanoparticles, inducing an increase in the singlet oxygen generation, but also by grafting target molecules to specifically target the malignant tissue. Secret and coworkers described nanosystems that consist of pSiNPs covalently functionalized with porphyrins and mannose as a target molecule, resulting in a better cell-killing effect compared to the use of free porphyrin and non-target nanoparticles. The pSiNPs were able to transfer part of their energy to the porphyrin via a resonant energy transfer mechanism. [138, 262]

In this part of the chapter, we describe the functionalization of the pSiNPs with an analog of mannose-6-phosphate and a porphyrin derivative, and we discuss the efficacy of the formulations in TPE-PDT, and in TPE-assisted delivery of siRNA on RMS cells. In TPE-assisted delivery of siRNA, the release of the endocytosed genetic material to the cytoplasm is due to a PCI mechanism. Upon irradiation and activation of the PS, there is a production of reactive oxygen species. ROS are responsible for the disruption of the endosomes-lysosomes membranes.[232] Our hypothesis is that the employment of pSiNPs–AMFA–porphyrin will improve the TPE-PDT effectiveness due to both: the AMFA, which favors the internalization of pSiNPs via mannose receptors overexpressed in RMS cells, and the energy transfer between the pSiNPs and the porphyrin, which induces the ROS production.

2.1. Experimental part

Materials

Hydrofluoric acid (HF, 48%), Allylamine (98%), and Diethylether (≥ 97.5%) were purchased from Sigma-Aldrich. Ethanol (EtOH, 100%) was purchased from VWR. p-[N- (2-Ethoxy-3,4-dioxocyclobut-1-enyl)amino]phenyl 6 deoxy-7- hydroxycarbonyl-α-D-manno-heptopyranoside [M6C-PhSq] was synthesized according to the synthesis described by E. Bouffard *et al.*[139] Boron-doped p++-type Si (0.8-1.2 mΩ.cm resistivity, <100> orientation) was purchased from Siltronix (France).

Analytical techniques

^{1}H and ^{13}C solution NMR spectra were recorded on a Bruker AC 400 spectrometer. Chemical shifts (in δ units, ppm) are referenced to TMS using residual DMSO-d_6 (δ = 2.50 ppm) resonance as the internal standard for ^{1}H NMR spectra, and DMSO-d_6 (δ = 39.52 ppm) for ^{13}C NMR spectra. UV-vis absorption spectra were recorded on a Hewlett-Packard 8453 spectrophotometer using correction factors supplied by the manufacturer. TEM analysis was performed on a JEOL 1200 EXII instrument. Dynamic light scattering analyses were performed using a Cordouan Technologies DL 135 Particle Size Analyzer instrument and analyzed with NanoQ software. IR spectra were recorded on a PerkinElmer 100 FT spectrophotometer. Zeta potential measurements were performed with a Malvern Zetasizer NanoSeries Instrument (pH=7 NaCl 5 mM).

Nanomaterials synthesis and characterization

Synthesis of 5-(4-iso-thiocyanatophenyl)-10,15,20-tris(4-N-1-methyl-4-pyridinio) porphyrin triiodide

The water-soluble 5-(4-iso-thiocyanatophenyl)-10,15,20-tris(4-N-1-methyl-4-pyridinio) porphyrin triiodide was prepared according method described by J. M. Sutton *et al.*[252] Succinctly, 5-(4-acetamidophenyl)-10,15,20-tri-(4-pyridyl)-porphyrin was obtained by Adler condensation. 5-(4-aminophenyl)-10,15,20-tri-(4-pyridyl)-porphyrin prepared from by 5-(4-acetamidophenyl)-10,15,20-tri-(4-pyridyl)-porphyrin by acid hydrolysis (HCl 5 N), was converted to 5-(4-iso-thiocyanatophenyl)-10,15,20-tri-(4-pyridyl)-porphyrin then methylated by methyl iodide.

Synthesis of pSiNPs

Boron-doped p++-type Si was electrochemically etched in a 3:1 (v:v) solution of aqueous 48% hydrofluoric acid (HF):absolute ethanol. Etching was performed in a Teflon cell with a platinum ring counter electrode. A constant current of 179 mA cm^{-2} was applied for 160 s, and the sample was rinsed 3 times with absolute ethanol. The porous layer was then removed from the substrate by application of a constant current of 1.57 mA cm^{-2} for 240 s in an electrolyte solution containing 1:13.5 (v:v) aqueous 48% hydrofluoric acid: absolute ethanol. After 3 rinses with absolute ethanol, the porous layer was placed in ethanol in a glass vial. After degassing the sample for 20 min under a nitrogen stream, the porous silicon film was fractured by ultrasonication during 21 h (Ultrasonic cleaner Fisher Transsonic TI-H-10). The largest particles were removed by spinning them down by centrifugation at 3 000 rpm for 3 min. In order to remove the smallest particles, the solution was finally centrifuged at 14 000 rpm for 30 min. The pellet was then redispersed in absolute ethanol.

Allylamine grafting onto pSiNPs by hydrosilylation

Freshly prepared pSiNPs were centrifuged at 14 000 rpm for 10 minutes in ethanol, then 44.5 mg of pSiNP were redispersed in 13 mL of allylamine and reacted for 3 h at 70°C under inert atmosphere. After the reaction, the aminated pSiNPs (pSiNPs–NH_2) were centrifuged at 14 000 rpm for 20 minutes and washed 5 times with absolute ethanol to remove the allylamine adsorbed onto their surface. The pSiNP–NH_2 were finally redispersed in 10 mL ethanol.

One-Pot reaction between the pSiNP–NH_2, the cationic porphyrin and the M6CPhSq

For the simultaneous grafting of the cationic porphyrin and the M6C-PhSq, 330 µL of a solution of M6C-PhSq at 16 mM in 1:1 (v:v) ethanol/water mixture and 167 µL of a solution of the cationic porphyrin at 1 mg mL^{-1} in ethanol were added to 10 mg of suspension of the pSiNP–NH_2 . The reaction was performed under stirring during 18 h at room temperature. The obtained nanoparticles were centrifuged at 14 000 rpm during 20 min and rinsed twice with absolute ethanol, twice with deionized water, twice with absolute ethanol, twice with diethylether, twice with absolute ethanol, producing 8 mg of pSiNPs–M6CPhSq–Porph in absolute ethanol.

Biological studies

Cell culture

RMS-YM cells from ATCC and SK-1111 normal myoblasts from CookMyoSite were used. RMS-YM cells were cultured in RPMI-1640 medium supplemented with 10% FBS and 1% penicillin/streptomycin. SK-1111 were cultured in Ham F10 medium plus 20% FBS, 1% insulin, 25 ng mL^{-1} FGF, 10 ng mL^{-1} EGF and 1% penicillin/streptomycin. All cell types were allowed to grow in a humidified atmosphere at 37 °C under 5% CO_2.

Cytotoxicity measurement

For cytotoxicity analysis, RMS-YM and SK-1111 cells were seeded into a 96 well plate, 2000 cells per well in 200 µL of culture medium and allowed to grow for 24 h. Then the cells were treated with increasing concentrations of pSiNPs–M6CPhSq–Porph (from 0.1 to 100 µg mL^{-1}). Three days after treatment, an MTT assay was performed to determine the cell viability. Briefly, cells were incubated for 4 h with 0.5 mg mL^{-1} of MTT (3-(4,5-dimethylthiazol-2-yl)-2,5-diphenyltetrazolium bromide, Promega) in media. The MTT/media solution was then removed and the precipitated crystals were dissolved in EtOH/ DMSO (v/v). The solution absorbance was read at 540 nm in a microplate reader. All values are reported in relation to the control values (without any treatment) which are considered as 100% living cells.

Two-photon excited photodynamic therapy

RMS-YM cells were seeded into a 384 multi-well glass-bottomed plate (thickness 0.17 mm) with a black polystyrene frame at a concentration of 1000 cells per well in 50 µL of culture medium, and allowed to grow for 24 h. After seeding, dispersed pSiNPs–M6CPhSq–Porph

were added on cells at a concentration of 80 µg mL^{-1} for 5 h. After this incubation cells were submitted or not to laser irradiation with the LSM 780 live confocal microscope (Carl Zeiss Microscope) at 800 nm by 3 scans of 1.57 s duration in 4 different areas of the well with a focused laser at a maximum laser power (laser power input 3 W). The laser beam was focused by a microscope objective lens (Carl Zeiss 10×/0.3 EC Plan-Neofluar). After 2 days, the MTT assay was performed as previously described and was corrected according to the following formula: Abs "No laser" − 2 × (Abs "No laser" − Abs "Laser"). Values are the mean of three experiments and error bars represent standard deviation.

Gel retardation assay

Different amounts of pSiNPs–M6CPhSq–Porph and a fixed amount of siRNA Ctrl (1.8 µM) were mixed in RNase free water in a total volume of 11 µl and incubated for 60 min at 37°C to induce the formation of siRNA/pSiNPs–M6CPhSq–Porph complexes. After incubation, blue 6X loading dye (Fisher scientific) was added to the complex. Electrophoresis was carried out on a 2 % w/v agarose gel mixed with GelRed TM nucleic acid gel stain (Interchim, France) in 1X TBE buffer (90 mM Tris-borate/mM EDTA, pH 8.2). The gel was run in 0.5X TBE at 50V for 30'. A 100 bp DNA ladder from Sigma-Aldrich (Saint-Quentin-Fallavier, S4 France) was used as reference for the gel. The GelREd-stained siRNA was visualized using a TFX-20 M model-UV transilluminator (Vilber Lourmat, Mare-la-Vallée, France).

Statistical analysis

Statistical analysis was performed using the Student's t test to compare paired groups of data. A p-value of <0.05 was considered to be statistically significant.

2.2. Results and discussion

Synthesis of pSiNPs grafted with allylamine

The pSiNPs were synthesized according to the protocol described in the experimental section; we then investigated subsequent functionalization with allylamine (Figure 26A). Allylamine was grafted by hydrosilylation onto the surface as well as inside the pores of pSiNPs following a procedure already described by Chaix *et al.*[138] pSiNPs–allylamine presented a hydrodynamic diameter of 348 nm (Figure 26B) and a negative value of zeta potential of -23.9 ± 0.3 mV. Due to the partial oxidation of pristine pSiNPs, deprotonated silanol groups were

present on their surface, leading to a negative value of zeta potential (-38.8 ± 0.2 mV). After the grafting of the allylamine, the surface charge changed to positive values. In theory, the amine groups on the surface were protonated, balancing the negative charges of silanol groups and giving rise to a positive surface charge. In our case, we supposed that the negative value of zeta potential (pH =7) was due to a partial functionalization of the nanoparticles by allylamine. This partial functionalization could not compensate for the negative charge of the silanol groups.

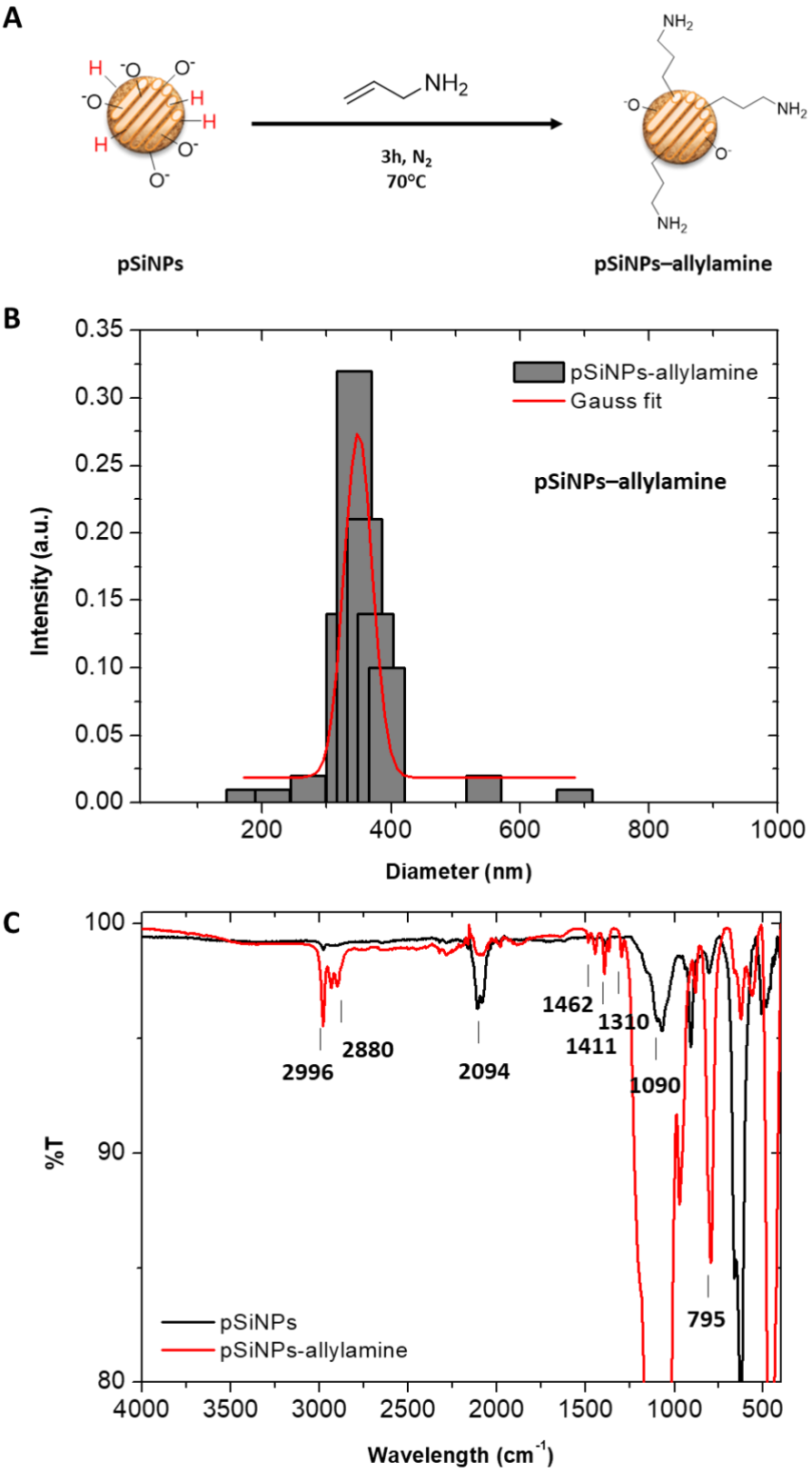

Figure 26. Synthesis and characterization of pSiNPs–allylamine. (A) Schematic representation of the grafting reaction in order to obtain pSiNPs–allylamine. (B) DLS in intensity of pSiNPs–allylamine. (C) Infrared spectra of pSiNPs (black line) and pSiNPs–allylamine (red line).

Bands corresponding to the covalent grafting of allylamine onto pSiNPs were identified in infrared spectroscopy. Figure 26C showed FTIR spectra of pSiNPs and pSiNPs–allylamine. The intense band between 1000 and 1270 cm^{-1} was assigned to the stretching vibration mode of Si-O bonds, explaining the partial oxidation of pSiNPs surface. Between 2996 cm^{-1} and 2880 cm^{-1} were detected the asymmetric and symmetric stretching vibration modes of the aliphatic carbons (ν_{CH2}) and between 1500 and 1300 cm^{-1} the asymmetric and symmetric bending modes of C-H (δ_{CH2}), all of them likely related to the ethanol absorbed inside de pores of the nanoparticles. In the spectrum of the pSiNPs–allylamine (red), the disappearance of the stretching band of Si-H at 2100 cm^{-1} and the increase of the ν_{CH2} stretching vibration modes indicated that the coupling of the allylamine onto the pSiNPs has certainly occurred.

One-pot synthesis of pSiNPs–AMFA–porphyrin

5-(4-iso-thiocyanatophenyl)-10,15,20-tris(4-N-1-methyl-4-pyridinio) porphyrin triiodide (porphyrin-NCS) and the M6CPhSq (AMFA) were synthesized following the protocol reported in the experimental section. After the hydrosilylation step, the amine group reacted with the squarate moiety of the M6CPhSq and the thiocyanate group of the porphyrin-NCS leading to a covalent attachment of both molecules on the surface of the pSiNPs (Figure 27).[262]

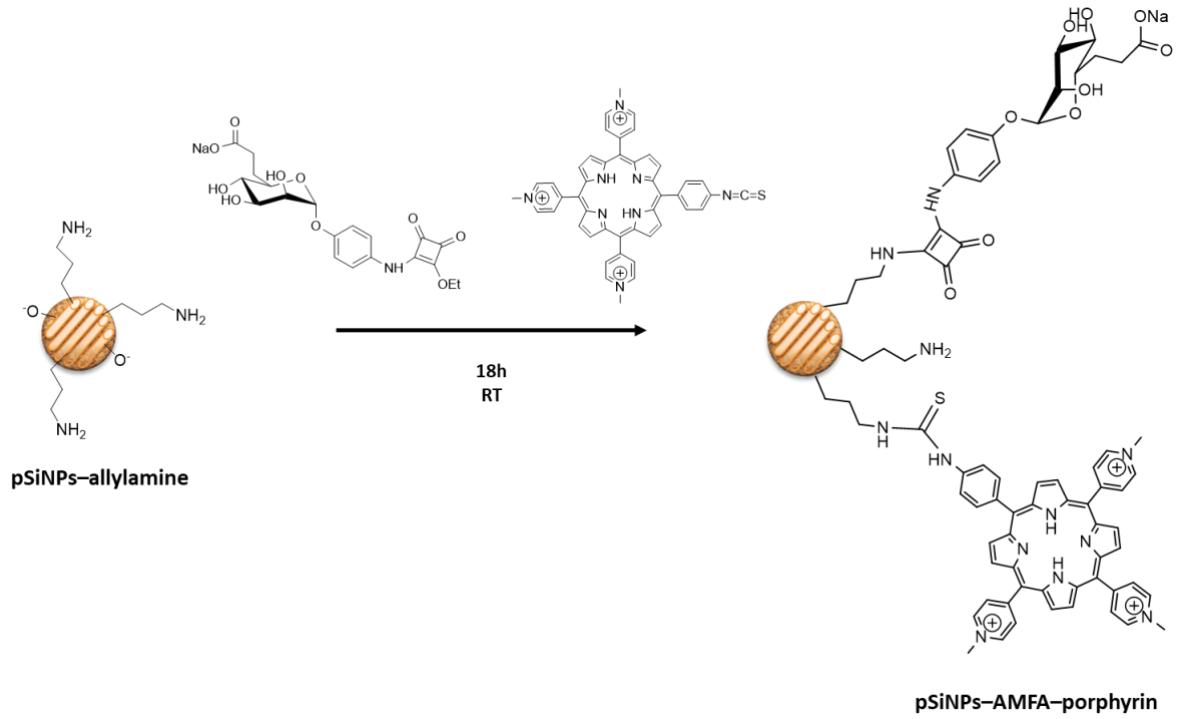

Figure 27. One-pot synthesis of pSiNPs–AMFA–porphyrin.

pSiNPs–AMFA–porphyrin presented a hydrodynamic diameter of 434 nm (Figure 28A) and zeta potential of -26.3 ± 0.4 mV. We expected a positive value of zeta potential after the functionalization with the porphyrin and the AMFA. Given the value obtained, we supposed that the amount of porphyrin covalently attached was too low to balance the effect of the negatively charged AMFA, resulting in a global negative charge on pSiNPs surface. The infrared spectrum of pSiNPs–AMFA–porphyrin is displayed in figure 28B. After the second reaction step, covalent attachment of the porphyrin was confirmed by the formation of a band at 1640 cm^{-1}, corresponding to stretching vibration modes of C=S of the thiourea. The stretching vibration modes of aromatic C=C around 1480 and 1300 cm^{-1} and asymmetric and symmetric stretching vibration modes of CH_2 between 2996 and 2893 cm^{-1}, belonging to the AMFA and to the porphyrin were observed. The UV-Vis spectrum of the pSiNPs–AMFA–porphyrin was showed in figure 28C. The Soret band and four Q bands corresponding to the porphyrin appeared at 436 nm and between 555, 520, 610 and 650 nm, respectively. These bands confirmed the presence of the porphyrin onto the pSiNPs. It was not possible to observe the absorption band of the AMFA, which should appear around 300 nm, due to the large scattering of the pSiNPs in this spectral region.

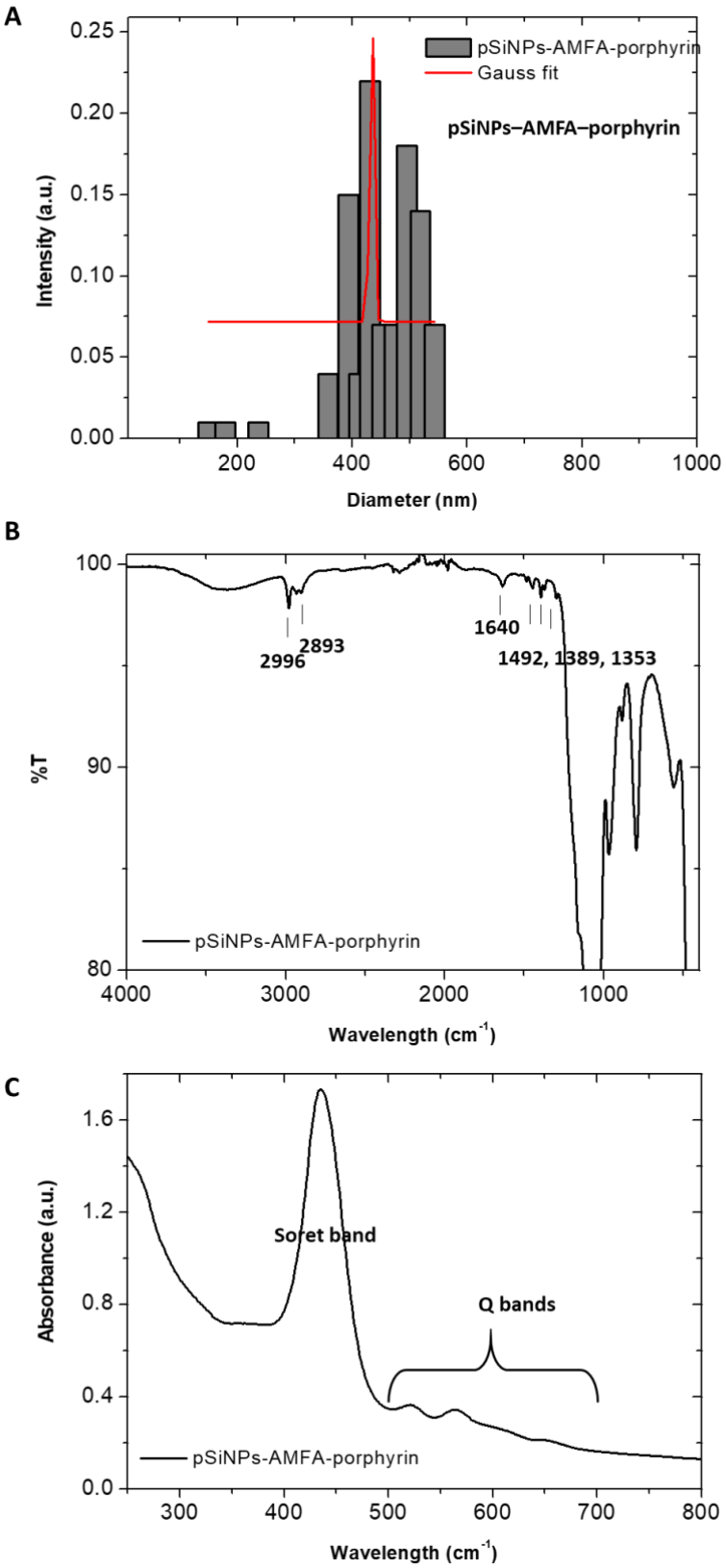

Figure 28. Characterization of pSiNPs–AMFA–porphyrin. (A) DLS in intensity of pSiNPs–AMFA–porphyrin (B) Infrared spectrum of pSiNPs–AMFA–porphyrin (C) UV-Vis absorbance spectrum of pSiNPs–AMFA–porphyrin.

Biocompatibility of pSiNPs–AMFA–porphyrin on different cell lines

The cytotoxicity of pSiNPs–AMFA–porphyrin was evaluated in RMS-YM cancer cells and SK-1111 normal myoblasts. Increasing concentrations of nanoparticles were added, and incubated for 3 days. These data demonstrated that pSiNPs–AMFA–porphyrin were non-toxic to RMS-YM cells and slightly toxic to normal myoblasts (Figure 29). In the case of normal myoblasts, an increase of cellular death up to 30 % upon NPs addition until a concentration of 5 µg mL^{-1} was observed. Over this value, cellular death increased to 50% for a concentration of 100 µg mL^{-1}. Given these results and to be consistent with previous experiments performed on pSiNPs, a concentration of 80 µg mL^{-1} was chosen for further biological experiments.

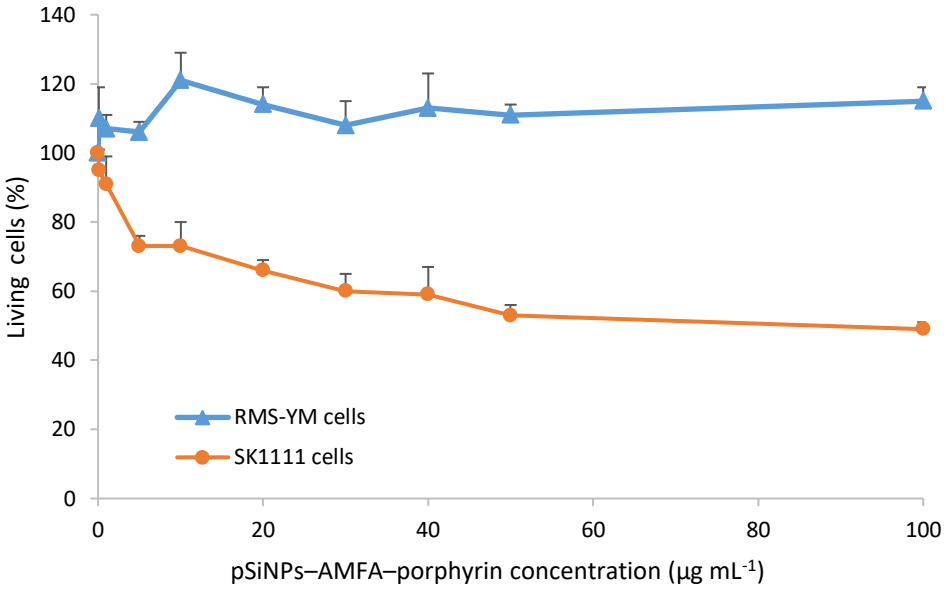

Figure 29. Cytotoxicity of pSiNPs–AMFA–porphyrin on cancer and normal cells. Cytotoxicity of pSiNPs–AMFA–porphyrin on RMS-YM cells (blue line) and on SK-1111 cells (orange line). Data are presented as mean ± SEM, of two independent experiments realized in triplicate.

Study of TPE-PDT

The photodynamic efficacy of pSiNPs–AMFA–porphyrin was studied on RMS-YM cells under near-infrared two-photon excitation (Figure 30). RMS-YM and SK-1111 were incubated with pSiNPs–AMFA–porphyrin for 5h. Then, they were irradiated or not at 800 nm three times for 1.57 s at a maximal laser power. In the absence of laser irradiation, toxicity due to the nanoparticles themselves was observed for both cell types. Moreover, pSiNPs–AMFA–porphyrin induced 36% RMS-YM cell death after TPE. In contrast, they did not induce any significant phototoxicity on healthy cells. Although these results could be improved in terms of

cell kill efficiency, they demonstrated that the use of a target molecule improved the specificity of the nanoparticles formulation for cancer cells, while being ineffective against healthy cells.

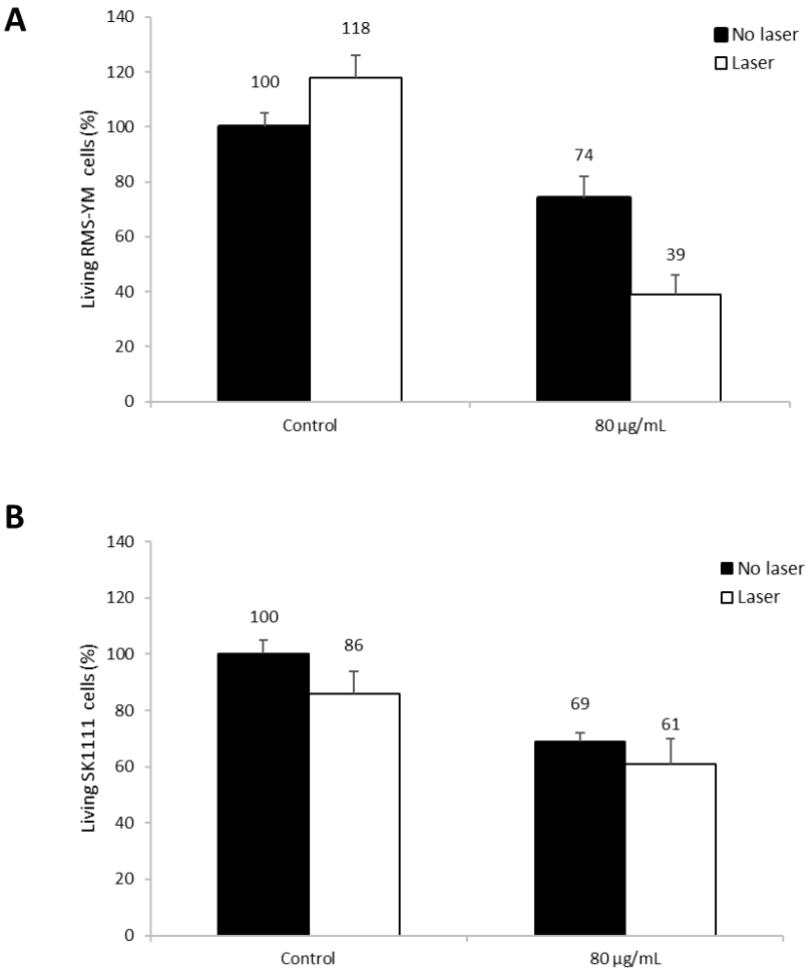

Figure 30. TPE-PDT with pSiNPs–AMFA–porphyrin. (A) Embryonal rhabdomyosarcoma cancer cells (RMS-YM) were incubated for 5h with pSiNPs–AMFA–porphyrin (80 µg mL^{-1}) and irradiated at 800 nm (3 × 1.57 s). Cell death was assessed after 2 days by the MTT reagent. (B) Human normal myoblasts cells (SK1111) were incubated for 5h with pSiNPs–AMFA–porphyrin (80 µg mL^{-1}) and irradiated at 800 nm (3 × 1.57 s). Cell death was assessed after 2 days by the MTT reagent. Control are the cancer cells and the healthy cells without incubating with nanoparticles. Data are mean values ± standard deviations from three independent experiments.

In vitro two-photon induced siRNA Delivery

siRNA complexation was evaluated, although pSiNPs–AMFA–porphyrin presented a negative value of zeta potential, not favorable for complexing positively charged siRNA. The siRNA presents negative charges due to the phosphate groups, promoting an electrostatic interaction between the positive charge of the porphyrin and the negative charges of the phosphate groups. Complexes between pSiNPs–AMFA–porphyrin and siRNA at siRNA/NPs

two ratios were tested (1/78 and 1/178), and no complexation was observed at neither of the ratios. In both cases, the migration of the siRNA was observed in the electrophoresis gel (Figure 31). Certainly, the negative value of zeta potential made these nanoparticles unsuitable for siRNA complexation, and consequently, performing the delivery of siRNA induced by two-photon excitation was not possible with this formulation.

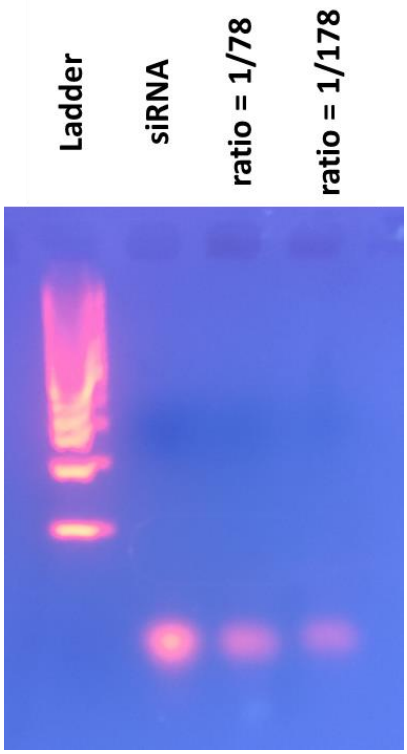

Figure 31. Gel retardation assay. siRNA and complexes at different ratios (1/78 and 1/178) were migrated to evaluate the complexation capacity of the pSiNPs–AMFA–porphyrin formulation.

2.3. Conclusion

In this part of the chapter, the synthesis, TPE-PDT effect, and the complexation capability of pSiNPs–AMFA–porphyrin were described. Based on the work described in the part I of chapter 2 about the overexpression of M6PR in RMS-YM cells, we decided to evaluate the targeting effectiveness of this formulation.

pSiNPs–AMFA–porphyrin were capable to specifically target and kill RMS-YM cancer cells due to the active endocytosis involving M6PR, and they did not show any effect on healthy cells under TPE irradiation. Here, the mechanism of $^1O_2$ and ROS generation was similar to what previously described Secret and coworkers[262], by mean of energy transfer between the excited pSiNPs to the attached porphyrin. Due to the non-suitable characteristics of the

formulations obtained, such as the negative value of zeta potential, it was not possible to complex the siRNA molecule.

2.4. Perspectives

This second part could be improved in several aspects. The optimization of the formulation to achieve a better TPE-PDT effect *in vitro* may be appropriate. For example, we could consider modifying the AMFA/porphyrin ratio to observe how can influence on ROS generation, or studying singlet oxygen production after TPE. In case of using it *in vivo*, we should tailor the formulation by grafting some PEGylated molecules to protect silicon nanoparticles from degradation and make them stealth. Subcellular localization of the nanoparticles could be verified by confocal imaging to have further proof of the uptake of pSiNPs–AMFA–porphyrin. Concerning the complexation experiments, we might study the ratio AMFA/porphyrin to obtain nanoparticles with a positive surface charge. We already observed in part II of chapter 2 that positive formulations were able to efficiently complex siRNA.

Part III. pSiNPs–ICPES-azobenzene@Lys for TPE-induced siRNA delivery on MCF-7 cells

Introduction

Gene therapy is a rapidly evolving therapeutic treatment consisting in the delivery of exogenous nucleic acid sequences designed specifically to target the diseased tissues. Gene delivery has been originally efficiently performed with viral systems.[263] However, they may exert immunologic and oncogenic adverse effects. Non-viral gene delivery systems, despite their current lower efficiency in terms of transfection, offer to overcome most of the shortcomings displayed by viral vectors, i.e. immune severe responses, low carrying capacity, small scale production, and high costs.[229, 264] In particular inorganic nanoparticles and their intrinsic physical properties at the nanoscale are intensively being assessed.[265-266]

pSiNPs may be a suitable option for cellular transfection due to their bioresorbability, biocompatibility, and their low toxicity *in vivo*.[94] Some examples of the use of pSiNPs are described below. Joo *et al.* developed graphene oxide nanosheets (GO-pSiNPs) conjugated to a targeting peptide derived from the rabies virus (RVG) and loaded with siRNA. This system showed greater cellular uptake and gene silencing in mouse neuroblastoma cell lines *in vitro*. After injection into brain-injured mice, the nanoparticles showed a significant accumulation in the tumor site.[267] Mann and coworkers synthesized short peptide-coated pSiNPs (CAQK-pSiNPs) encapsulating siRNA to use them in gene silencing in injured brain parenchyma.[268] The Voelcker group developed polyethyleneimine-pSiNPs (PEI-pSiNPs) for MRP1 silencing *in vitro* and *in vivo*. [269-270] In addition pSiNP can be excited by near infrared (NIR) two-photon excitation (TPE) light[262] thus offering additional possibilities for light triggered treatment, based on tissue-penetrable NIR light response.

Indeed, few examples of cell transfection using light triggered nucleic acid delivery systems have been described. The major works reported so far use UV-Vis light; [271-280] that does not penetrate deep into tissues and can damage cells. In this field, cationic azobenzene-based systems were shown to be efficient for enhancing gene transfection[281] or to photocontrol the transcription/translation of nucleic acids.[282-283] Unlike UV-Vis light, TPE provides a high temporal and tri-dimensional spatial resolution at the micron scale, thus a potent mean for the selective delivery of genes, while the combination with NIR excitation enhances safer tissue penetration, with less scattering than UV/Visible light.

Therefore recent works tuned to the NIR including up-converting systems based on nitrobenzyl group cleavage, [284-287] or host-guest interactions between cyclodextrin and azobenzene covalently linked to siRNA.[288] Plasmonic systems have been described for NIR light-induced photothermal control of gene silencing with siRNA;[289-295] and the direct two-photon cleavage of 4,5-dimethoxy-2-nitrobenzyl group[280, 296] has been reported, but since this group possesses a very low two-photon decaying cross-section,[297] very long times of irradiation were needed.

In this part, we present pSiNPs functionalized with ICPES-azobenzene@Lys to efficiently complex siRNA by non-covalent interactions. A reversible *trans-cis* isomerization of the azobenzene after UV-Vis irradiation (365 nm) was described in the literature. The conformation exchange went along with a change in the affinity for the nucleic acid. [283] Based on this, we suggest that the pSiNPs after NIR-TPE irradiation could transfer their energy to the grafted azobenzene molecule, triggering the *trans-cis* conformation exchange expected. This isomerization is expected to provoke membrane disruption and the siRNA delivery in the cytoplasm.

3.1. Experimental part

Materials

Hydrofluoric acid (HF, 48%), toluene, tetrahydrofuran (anhydrous, THF ≥99%) trifluoroacetic acid (TFA, ≥99%) and triethoxy(3-isocyanatopropyl)silane (95%) were purchased from Sigma-Aldrich. Ethanol (EtOH, 100%) was purchased from VWR. Dichloromethane (DCM, RE technical) was purchased from Carlo Erba. Boron-doped p++-type Si (0.8-1.2 mΩ.cm resistivity, <100> orientation) was purchased from Siltronix (France).

Analytical techniques

^{1}H solution NMR spectra were recorded on a Bruker AC 400 spectrometer. Chemical shifts (in δ units, ppm) are referenced to TMS using residual DMSO-d_6 (δ = 2.50 ppm) resonance as the internal standard for ^{1}H NMR spectra. TEM analysis was performed on a JEOL 1200 EXII instrument. Dynamic light scattering analyses were performed using a Cordouan Technologies DL 135 Particle Size Analyzer instrument and analyzed with NanoQ software. IR spectra were recorded on a PerkinElmer 100 FT spectrophotometer. Zeta potential

measurements were performed with a Malvern Zetasizer NanoSeries Instrument (pH = 7, NaCl 5 mM).

Nanomaterials synthesis and characterization

Synthesis of ICPES-azobenzene@Lys(diBoc)

ICPES-azobenzene@Lys-diBoc was prepared according to the method described by M. K. Abdul Rahim *et al.*[298] Concisely, Aminoazobenzene@Boc-Lys-(Boc)-OH was obtained by the reaction between Boc-Lys(Boc)-OH (Dicyclohexylammonium) Salt with 4,4'-diaminoazobenzene under Ar atmosphere in anhydrous DMF overnight at RT. Then it was silylated by reacting with triethoxysilyl isocyanate under reflux of anhydrous THF during 24h. The residue was washed several times with pentane and then dried under vacuum.

Synthesis of pSiNPs

Boron-doped p++-type Si was electrochemically etched in a 3:1 (v:v) solution of aqueous 48% hydrofluoric acid (HF):absolute ethanol. Etching was performed in a Teflon cell with a platinum ring counter electrode. A constant current of 179 mA cm^{-2} was applied for 160 s, and the sample was rinsed 3 times with absolute ethanol. The porous layer was then removed from the substrate by application of a constant current of 1.57 mA cm^{-2} for 240 s in an electrolyte solution containing 1:13.5 (v:v) aqueous 48% hydrofluoric acid: absolute ethanol. After 3 rinses with absolute ethanol, the porous layer was placed in ethanol in a glass vial. After degassing the sample for 20 min under a nitrogen stream, the porous silicon film was fractured by ultrasonication during 18 h (Ultrasonic cleaner Fisher Transsonic TI-H-10). The largest particles were removed by spinning them down by centrifugation at 3 000 rpm for 3 min. In order to remove the smallest particles, the solution was finally centrifuged at 14 000 rpm for 30 min. The pellet was then redispersed in absolute ethanol.

Grafting of ICPES-azobenzene@Lys(diBoc) onto pSiNPs

20 mg of ICPES-azobenzene@Lys(diBoc) was added to a suspension of 25 mg of pSiNPs in 3 ml of Toluene. The reaction was carried out at 50°C for 18 h under inert atmosphere. The pSiNPs–ICPES-azobenzene@Boc-Lys-(Boc)-OH were centrifuged 14 000 rpm during 20 min and rinsed three times with absolute ethanol, and then redispersed in 10 mL of absolute ethanol.

Deprotection of pSiNPs– ICPES-azobenzene@Lys(diBoc)

pSiNPs–ICPES-azobenzene@Lys(diBoc) were dispersed in 3 mL of dichloromethane. 1 mL of TFA was added dropwise to the mixture. The reaction was kept under stirring at RT for 30 min. The pSiNPs–ICPES-azobenzene@Lys were centrifuged 14 000 rpm during 20 min and rinsed four times with absolute ethanol, leading to 25 mg of pSiNPs–ICPES-azobenzene@Lys in absolute ethanol.

Biological studies

Cell culture

MCF-7 and MCF-7-luc cells from ATCC were used. MCF-7 were cultured in DMEM medium supplemented with 10% FBS and 50 µg mL^{-1} gentamycin. MCF-7-luc were cultured in DMEM/F12 medium supplemented with 10% FBS and 1% geneticine. All cell types were allowed to grow in a humidified atmosphere at 37 °C under 5% CO_2.

Gel retardation assay

In RNase free water, different amounts of pSiNPs–ICPES-azobenzene@Lys and a fixed amount of siRNA Ctrl (1.8 µM) were mixed in a total volume of 22 µl and incubated for 30 min at 37°C to induce the formation of siRNA/pSiNPs–ICPES-azobenzene@Lys complexes. After incubation, blue 6X loading dye (Fisher scientific) was added to the complex. Electrophoresis was carried out on a 2 % w/v agarose gel mixed with GelRed TM nucleic acid gel stain (Interchim, France) in 1X TBE buffer (90 mM Tris-borate/mM EDTA, pH 8.2). The gel was run in 0.5X TBE at 50V for 30'. A 100 bp DNA ladder from Sigma-Aldrich (Saint-Quentin-Fallavier, S4 France) was used as reference for the gel. The GelREd-stained siRNA was visualized using a TFX-20 M model-UV transilluminator (Vilber Lourmat, Mare-la-Vallée, France).

In vitro two-photon induced siRNA delivery

MCF-7-luc were seeded at a density of 1000 cells per well in a 384 black multi-well glass-bottomed plate with a black polystyrene frame (Proteigene, France) one day before transfection. To control siRNA efficiency, transfection of siRNA was performed first with Lipofectamine RNAiMAX reagent (Invitrogen, France). Complex between anti-Luc siRNA and pSiNPs–ICPES-azobenzene@Lys at a ratio of 1:30 (µL:µL) was freshly prepared and incubated for 30 min at 37 °C for pairing. Then MCF-7-luc cells were incubated for 5 h with

the complex at 40 µg mL^{-1}. After incubation, the cells were submitted (or not) to laser irradiation using the Carl Zeiss Microscope (laser power input 3 W). Half of the well was irradiated at 800 nm by three scans of 1.57 s duration in four different areas of the well. No supplementary scan can be performed without overlapping. A microscope objective lens (Carl Zeiss tenfold magnification/objective 0.3 EC Plan-Neofluar) was used to focus the laser beam. After 48h transfection, apoptosis efficacy was assessed by addition into the culture medium of luciferin (10^{-3} M, final concentration) purchased from Promega (France). Living cell luminescence was measured 10 min after by a multilabel plate reader CLARIOstar® at 562 nml. Results were corrected according to the following formula $Lum_{non\ irradiated} - 2\ (Lum_{non\ irradiated} - Lum_{irradiated})$, where Lum is the luminescence emitted. Luciferase activity was normalized in accordance to the total number of living cells in each sample as determined by MTT assay.

Statistical analysis

Statistical analysis was performed using the Student's t test to compare paired groups of data. A p-value of <0.05 was considered to be statistically significant.

3.2. Results and discussion

Synthesis of pSiNPs–ICPES-azobenzene@Lys

pSiNPs and ICPES-azobenzene@Lys(diBoc) were first synthesized following the protocol reported in the experimental section, then ICPES-azobenzene@Lys(diBoc) was grafting onto the pSiNPs by silanization chemistry through the hydroxyl groups available on their surface (Figure 32). pSiNPs– ICPES-azobenzene@Lys(diBoc) presented a hydrodynamic diameter of 282 nm and zeta potential of -3.37 ± 0.05 mV. The last step of the synthesis was the deprotection of the BOC group (tert-butoxycarbonyl), leading to the pSiNPs–ICPES-azobenzene@Lys with a hydrodynamic diameter of 307 nm (Figure 33) and zeta potential of 31.9 ± 0.6 mV.

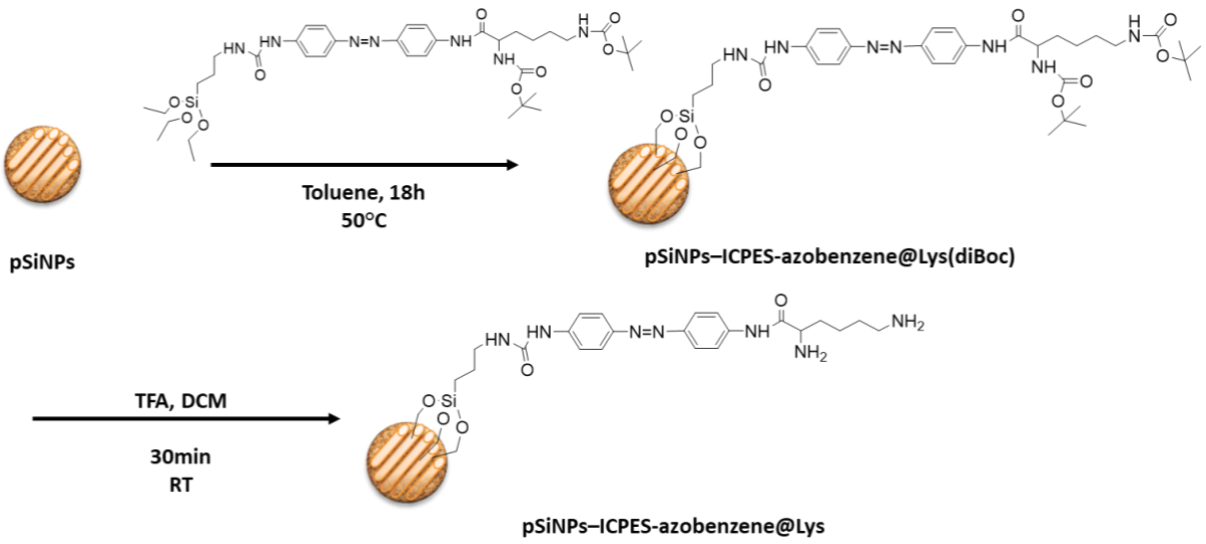

Figure 32. Synthesis of pSiNPs–ICPES-azobenzene@Lys. Schematic representation of the different steps of the synthesis to obtain the desired formulation.

DLS and zeta potential values at each step were listed in Figure 33. The pSiNPs and pSiNPs– ICPES-azobenzene@Lys(diBoc) presented a negative value of zeta potential due to the partial oxidation of their surfaces, which was in agreement with the presence of silanol groups. On the other hand, after the deprotection step, there was a charge reversal due to the amino acids grafted onto the nanoparticles. This charge reversal to positive values suggested the successful functionalization of the pSiNPs and was appropriate for further complexation of siRNA onto the nanoparticles. The siRNA presents negative charges due to the phosphate groups, promoting an electrostatic interaction between the positive charges of lysine groups and the negative charges of the phosphate groups.

	DLS /nm	Z-potentials /mV
pSiNPs	276 ± 49	-38.8 ± 0.2
pSiNPs–ICPES-azobenzene@Lys(diBoc)	282 ± 54	-3.37 ± 0.05
pSiNPs–ICPES-azobenzene@Lys	307 ± 37	31.9 ± 0.6

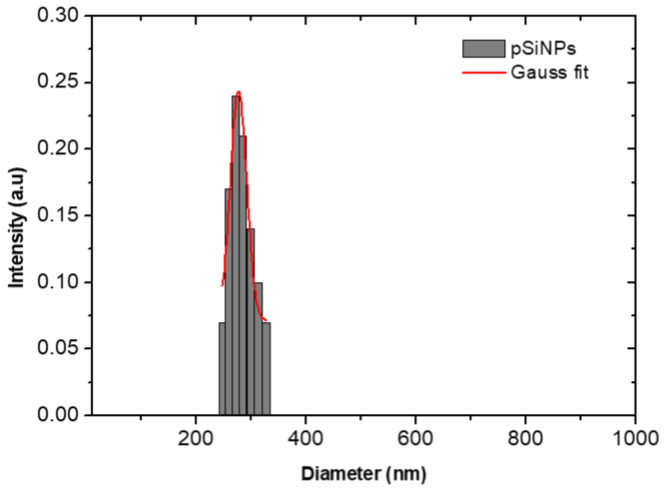

pSiNPs

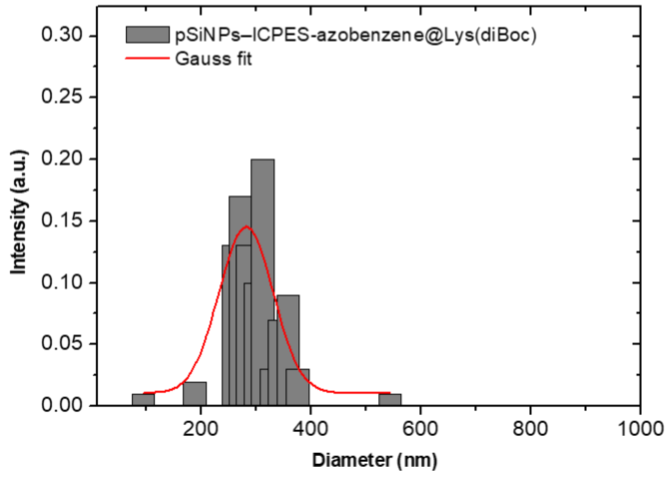

pSiNPs–ICPES-azobenzene@Lys(diBoc)

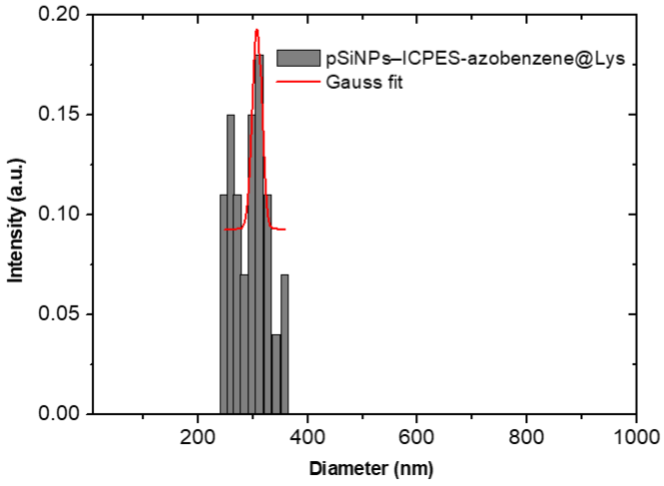

pSiNPs–ICPES-azobenzene@Lys

Figure 33. Characterization of different formulations. DLS in intensity and zeta potential of pSiNPs, pSiNPs–ICPES-azobenzene@Lys(diBoc) and pSiNPs–ICPES-azobenzene@Lys.

Covalent grafting of ICPES-azobenzene@Lys(diBoc) onto pSiNPs was confirmed not only by zeta potential measurements but also by infrared spectroscopy. Figure 34 showed FTIR spectra of pSiNPs and pSiNPs–ICPES-azobenzene@Lys. The intense band between 1000 and 1270 cm^{-1} was assigned to the stretching vibration mode of Si-O bonds, explaining the partial oxidation of pSiNPs surface. This large band could hamper the observation of the stretching vibration mode of the C-N bond that appeared around 1250 cm^{-1}. After the first coupling step (red line), thiourea characteristic vibrations modes of ICPES-azobenzene@Lys(diBoc) covalently attached to the nanoparticles were observed, specifically, $\nu_{C=O}$ = 1685 cm^{-1} δ_{NH} = 1557 cm^{-1}, confirming the successful grafting of the linker.

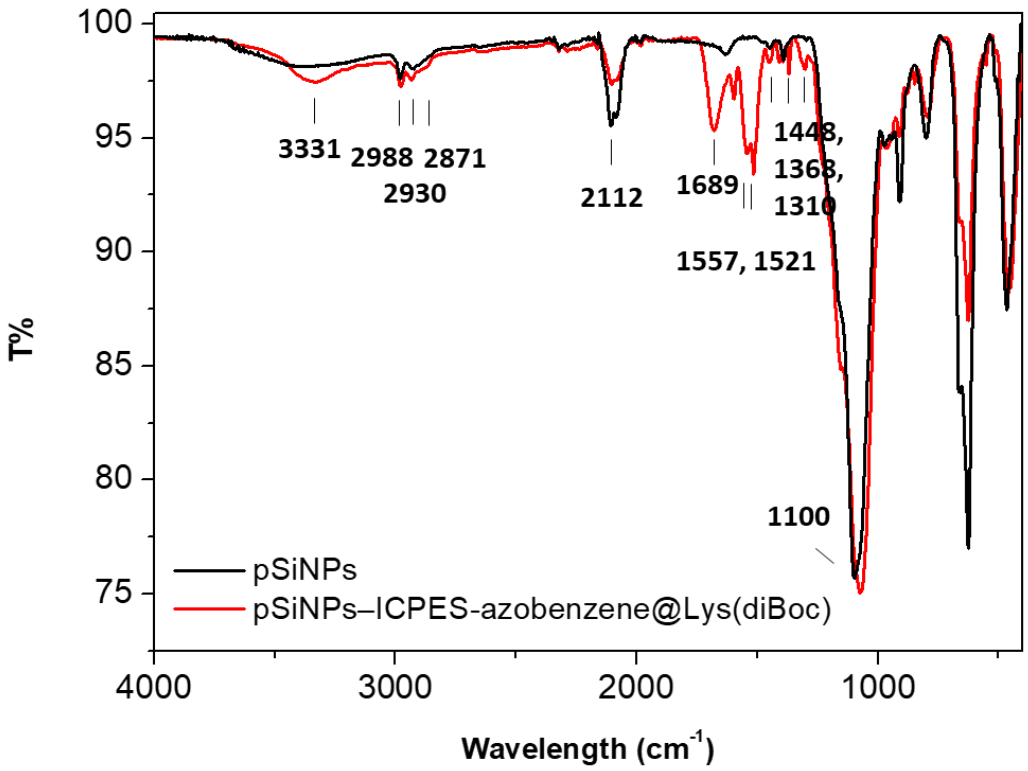

Figure 34. Infrared spectra of pSiNPs (black line) and pSiNPs–ICPES-azobenzene@Lys (red line).

Another representative band, which also helped to confirm the grafting, is the stretching vibration mode of the N=N bond from the azobenzene at 1444 cm^{-1}. Between 2990 and 2875 cm^{-1}, three bands corresponding to stretching modes of alkanes (ν_{CH3} and ν_{CH2}) were observed. Finally, the band at 3342 cm^{-1} corresponds to the stretching vibration mode of secondary NH_2.

In vitro two-photon induced siRNA Delivery

The complexation efficiency of pSiNPs–ICPES-azobenzene@Lys, which showed a favorable surface charge for siRNA complexation was evaluated. Complexes between pSiNPs–ICPES-azobenzene@Lys and siRNA at three ratios siRNA/NPs were tested (1/5, 1/30, and

1/90). No complexation was observed at a ratio of 1/5, while a disappearance of migration bands was observed from a ratio of 1/30 (Figure 35), suggesting a complete complexation at 1/30 and 1/90. Therefore, the ratio of 1/30 was chosen for further experiments. The halos observed inside the last two wells (yellow rectangle) were a sign of the successful complexation between the NPs and the siRNA, demonstrating that siRNA was complexed.

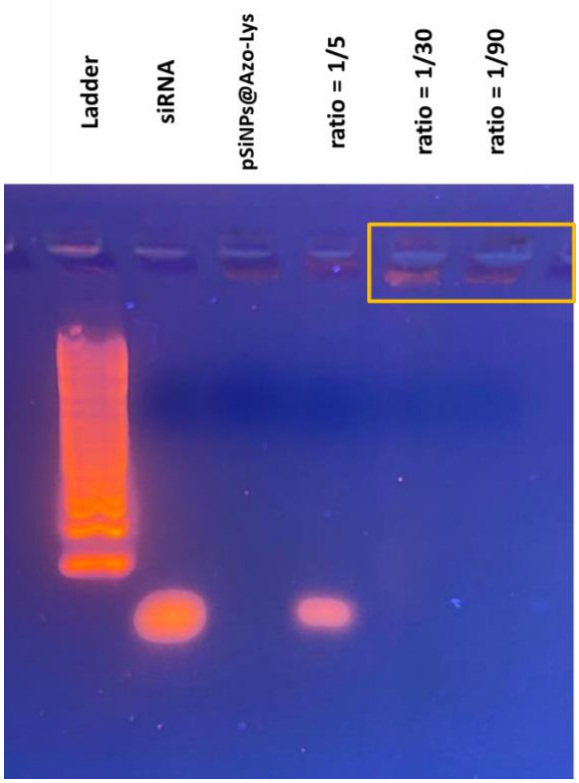

Figure 35. Gel retardation assay. siRNA and complexes at different ratios (1/5, 1/30, and 1/90) were migrated to evaluate the complexation efficiency of pSiNPs–ICPES-azobenzene@Lys. Sign of complexation inside the yellow rectangle.

The delivery of siRNA triggered by two-photon excitation was then examined. As a proof of concept, luciferase-expressing MCF-7 breast cancer cells and anti-Luc siRNA were used. The complex between pSiNPs–ICPES-azobenzene@Lys and anti-Luc siRNA at 40 µg mL^{-1} was incubated with MCF-7-Luc for 5h at Room Temperature. The free anti-Luc siRNA did not affect luciferase expression when incubated with MCF-7-Luc cells after TPE, probably because the molecule was not able to cross the membrane and get to the cytosol. In contrast, in this preliminary experiment, the complex between siRNA and the functionalized pSiNP with azobenzene moieties possessing a lysine, showed effective endocytosis in MCF-7 cells expressing luciferase (Figure 37). In addition, after two-photon irradiation of the cells, we observed luciferase gene silencing (38%) compared to 0% in the absence of irradiation (Figure

36A). Unfortunately, and unexpectedly, despite the successful complexation observed in our latest experiments, we were not able to reproduce the luciferase gene silencing. There was no transfection effect after TPE irradiation of the siRNA/pSiNPs–ICPES-azobenzene@Lys complex (Figure 36B).

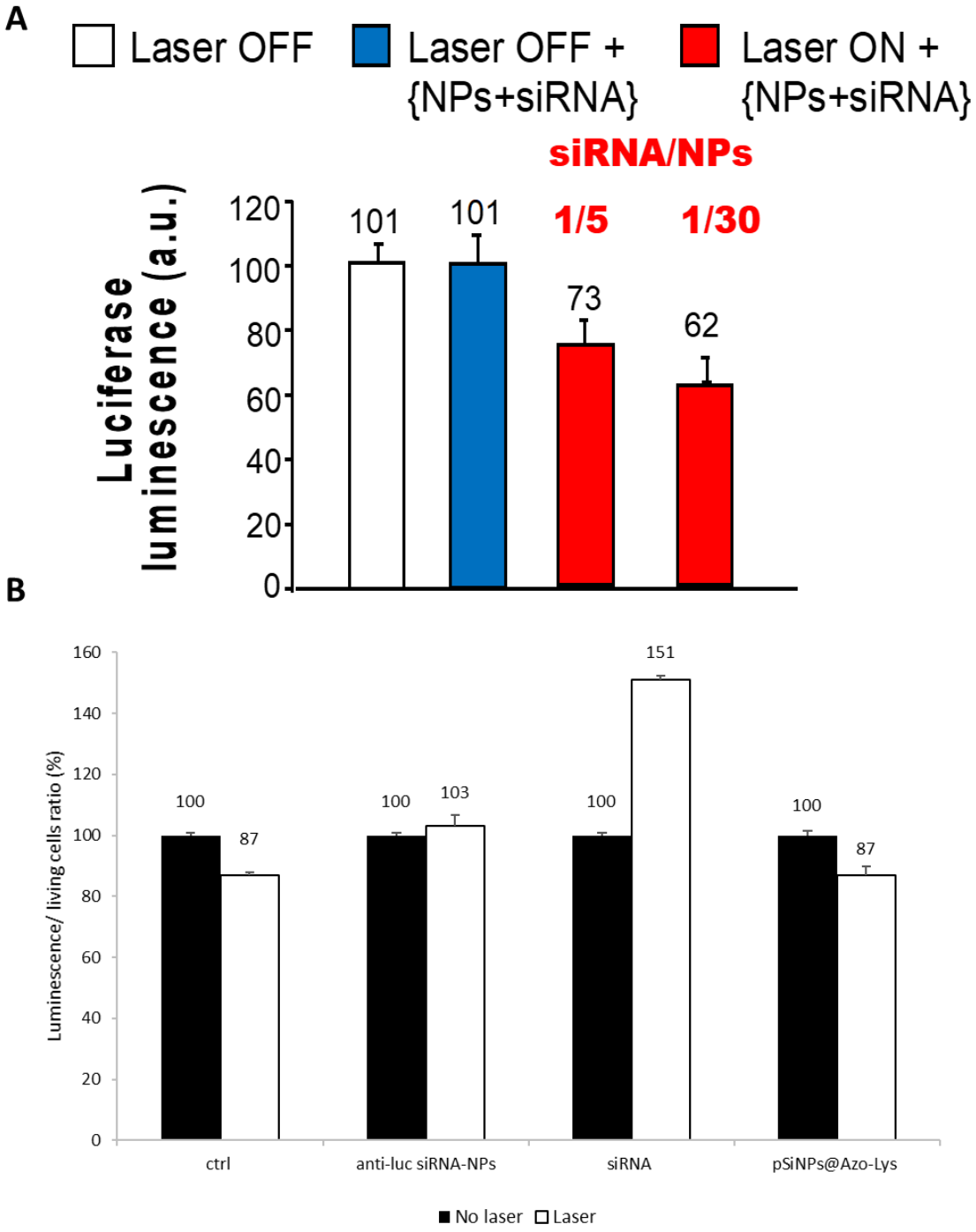

Figure 36. TPE-triggered siRNA delivery. (A) Preliminary experiments (B) Experiment performed during the thesis work. Luciferase-expressing MCF-7 breast cancer cells were incubated with pSiNPs–ICPES-

azobenzene@Lys (40 μg mL^{-1}) and irradiated at 800 nm (3 × 1.57 s). Cell death was assessed after 2 days and MTT assay. Data are mean values ± standard deviations from three independent experiments.

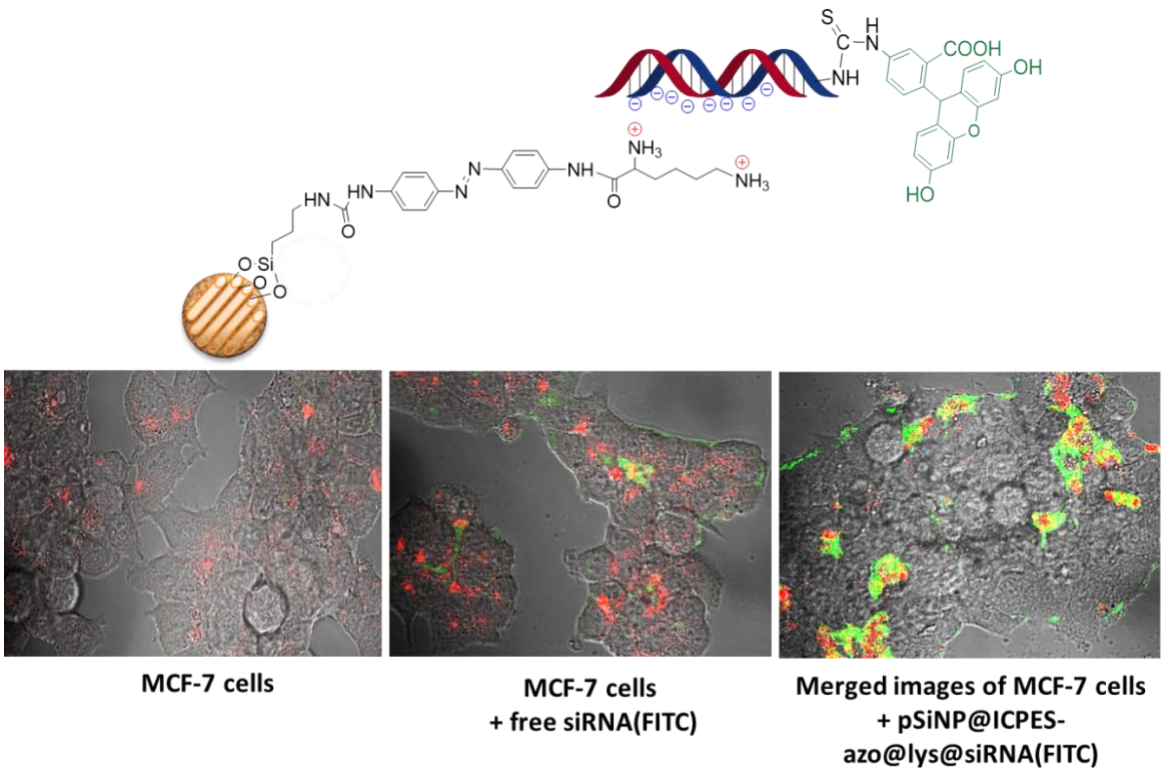

Figure 37. Preliminary results of nanoparticles internalization in MCF-7. Cells were stained with lysotracker and incubated with free siRNA (160 nM) and siRNA complexed with pSiNPs–ICPES-azobenzene@Lys (ratio 1/25, siRNA/pSiNp) for 24 hours.

In previous work, it has been shown that pSiNPs can absorb TPE light and transfer their energy to attached absorbing molecules.[262] Thus, we hypothesized that the siRNA release mechanism is due to the photo-isomerization of the azobenzene groups upon TPE. The irradiation generated resonance energy transfer from the pSiNPs to azobenzene. In our case, we believe that a lock of the *trans-cis* isomerization was produced, hampering the membrane disruption and then the release of the siRNA (Figure 38). Since there was no light trigger siRNA delivery, it was not possible to observe the expected gene silencing effect.

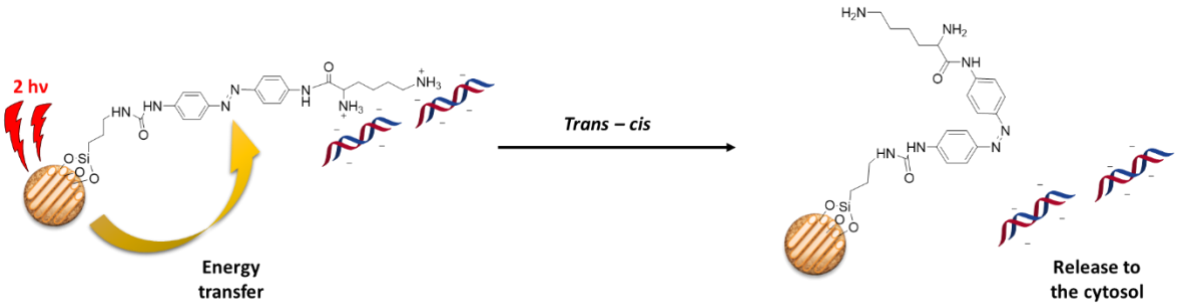

Figure 38. Schematic representation of the reversible *trans-cis* isomerization of the azobenzene after irradiation and subsequently siRNA release mechanism.

3.3. Conclusion

Here we described the synthesis, complexation efficiency, and TPE-triggered siRNA delivery ability of pSiNPs–ICPES-azobenzene@Lys. We successfully synthesized the azobenzene derivative and grafted it onto pSiNPs to obtain suitable nanoparticles for siRNA complexation. First attempts in gene therapy on MCF-7-Luc have not been successful. These nanoparticles presented an efficient complexation capacity, but the gene delivery failed to happen. We hypothesized that an isomerization problem between *trans-cis* conformations occurred, making impossible the destabilization of the membrane and thus the subsequent siRNA release.

3.4. Perspectives

This work should be improved in some aspects. First, the process of gene delivery by TPE irradiation might be optimized. We can conceive performing the grafting reaction with several amounts of ICPES-azobenzene@Lys(diBoc). The aim will be to verify whether there could be a steric encumbrance caused by an excess of functionalization with the ICPES-azobenzene@Lys. We speculate that this steric encumbrance could hamper the *trans-cis* isomerization. In addition, we might consider studying the endocytosis and internalization of the complexes using fluorescence confocal microscopy.

CHAPTER 4: General conclusion and outlooks

Pediatric cancer continues to be one of the major causes of childhood mortality worldwide; consequently, the development of target therapies as alternatives to conventional ones is a public health affair. Treatments based on more personalized and tailored therapies might help in specifically targeting diseased tissues avoiding the healthy ones. This manner of treating patients might aid in the reduction of the short and long-term side effects and increase the therapeutic effectiveness.

Although the number of clinical tests performed is increasing, the formulations place on the market are still scarce. My thesis project was centered on this problematic: The aim was to develop multifunctional nanoparticles, porphyrin-based organosilica nanoparticles (PMOsPOR-NPs) and porous silicon nanoparticles (pSiNPs). We have used them in a triple targeting approach based on the combination including targeting ligands, photodynamic therapy or/and gene delivery. These three elements as well as the cancer of study, the Rhabdomyosarcoma were detailed in chapter 1. The next chapters were devoted to the applications of these approaches to practical cases.

In chapter 2 part I, we have described the synthesis and application of Porphyrin-based organosilica nanoparticles (PMOsPOR-NPs) functionalized with a target biomolecule as a platform for RMS theranostics. This biomolecule was an analog of mannose 6-phosphate capable of efficiently targeting M6PRs, a receptor overexpressed in other cancers such as breast or prostate. Our collaborators have proven their overexpression in three cell lines of RMS. Indeed, the expression of the receptor was seven times higher in RMS cells than in healthy myoblasts, suggesting that CI-RM6P could be considered as a biomarker for the development of RMS. The nanoparticles have shown their biocompatibility and a high TPE-PDT effect. Non-functionalized PMO-NPs induced up to 60 % of cellular death in both cell lines, while PMO−AMFA induced almost 100% of cellular death on RMS-YM cells and no toxicity on healthy myoblast after TPE-PDT. These results indicated the involvement of CI-RM6P in active endocytosis pathway of the PMO−AMFA, demonstrating that this receptor is a potential therapeutic target for RMS. In part II, we described the modification of PMO−AMFA to use them in TPE-induced siRNA delivery in MCF-7 breast cancer cells. siRNA is a small interfering RNAs that can bind specifically to a messenger RNA sequence to block the expression of the target gene. The novel formulation showed acceptable biocompatibility and maintained its efficacy in TPE-PDT as well as in cancer targeting after APTES inclusion. First attempts in gene delivery led to a remarkable silencing effect. As a proof of concept, complexes between anti-Luc siRNA/ PMO−AMFA−APTES were tested on MCF-7-Luc cells, producing

a diminution in the luminescence up to 57% compared to the use of free anti-Luc siRNA. PMO−AMFA−APTES allowed not only the protection of the genetic material, guaranteeing the delivery to the cells, but also the generation of ROS. The reactive oxygen species were responsible for endosomes-lysosomes membranes disruption, giving rise to the release of the endocytosed siRNA.

In chapter 3, the synthesis of pSiNPs as well as their functionalization with two target biomolecules, the analog of mannose 6-phosphate and a conotoxin peptide, were described. In the bibliography, the use of a conopeptide to specifically target another receptor overexpressed on RMS cancer cells was reported. These multifunctional nanoparticles offered two ways of surface modification, either silanization or hydrosilylation, and they were used in different applications according to the molecule grafted on their surface. In part I, we have detailed the modification of the pSiNPs with a conopeptide, obtaining a formulation with better stability than other silicon-based nanoparticles. We envisaged targeting the fetal acetylcholine receptor (fAChR), another biological marker of RMS cancer cells. Preliminary results did not show a good internalization of the nanoparticles, so we assumed that there was a recognition problem between the receptor and the conotoxin peptide. In part II, the pSiNPs were functionalized with the analog of mannose and a photosensitizer (a cationic porphyrin). They efficiently targeted M6PR, being internalized in RMS-YM cells, and showed effectiveness in TPE-PDT. We have proposed an energy transfer mechanism between the porous silicon and the porphyrin to explain the $^1O_2$ generation. In the last part of this chapter, after modification of pSiNPs by grafting an azobenzene derivative, the formulation was tested for TPE-induced siRNA delivery in MCF-Luc-7 cells. We have also suggested an energy transfer mechanism between the porous silicon and the azobenzene derivative. In this case, it induced the *trans-cis* isomerization of the azobenzene promoting the release of the complexed siRNA. Nanoparticles showed anti-Luc siRNA efficient complexation, but the process of gene delivery did not take place. We presumed that there was an isomerization problem, which hampered the destabilization of the membrane and the release of the genetic material to the cytoplasm.

Nevertheless, this work could be improved in different manners. The use of PDT for RMS treatment in clinical practice presents some limitations because sarcomas are deep and hardly accessible tumors. As an alternative of PDT, we could consider modifying the nanoparticles to make them stimuli-responsive. We could efficiently target RMS receptors by AMFA molecules and induce the delivery of encapsulated drugs, and/or siRNA by changes in the pH, or in the cellular environment. An example is the modification of the structure to

introduce tetrasulfide bonds, which can be degraded in a reducing medium[90]. Another example could be the introduction of a pH-responsive valve system, which will be closed at the physiological pH and would release the endocytosed molecule under acidic conditions characteristic of endosomal/lysosomal vesicles.[299-300] As previously mentioned, the PAX3 FOXO1a fusion gene is present in the alveolar rhabdomyosarcoma (ARMS). Blocking or down-regulating this fusion gene would, significantly inhibit cell proliferation, and subsequently RMS development. Considering the work developed by Rengaswamy and coworkers, [204] where they encapsulated anti-PAX3-FOXO1a siRNA inside liposomes, we could envisage anti-PAX3-FOXO1a siRNA encapsulation inside the nanoparticles described in this thesis work. We might take advantage of the active targeting of RMS, to specifically deliver the nanoparticles and facilitate siRNA action.

Bibliography

1. World Health Organization. https://www.who.int/news-room/fact-sheets/detail/cancer (accessed 13th April).

2. Ferlay J, E. M., Lam F, Colombet M, Mery L, Piñeros M, Znaor A, Soerjomataram I, Bray F Global Cancer Observatory: Cancer Tomorrow. Lyon, France: International Agency for Research on Cancer. https://gco.iarc.fr/today (accessed 13th April 2021).

3. Sung, H.; Ferlay, J.; Siegel, R. L.; Laversanne, M.; Soerjomataram, I.; Jemal, A.; Bray, F., Global cancer statistics 2020: GLOBOCAN estimates of incidence and mortality worldwide for 36 cancers in 185 countries. *CA: A Cancer Journal for Clinicians* **2021**, *0*, 1-41.

4. Steliarova-Foucher, E.; Colombet, M.; Ries, L. A. G.; Moreno, F.; Dolya, A.; Bray, F.; Hesseling, P.; Shin, H. Y.; Stiller, C. A.; Bouzbid, S.; Hamdi-Cherif, M.; Hablas, A.; Chirpaz, E.; Buziba, N.; Chesumbai, G. C.; Manraj, S. S.; Reynders, D.; Wabinga, H. R.; Chokunonga, E.; Moreno, F.; Lima, C. A.; Asturian Laporte, C.; de Oliveira, J. C.; de Aquino, J. A. P.; Gallagher, S. M. V.; Uribe, C. J.; Bravo, L. E.; Yepez Chamorro, M. C.; Torres Alvarado, G.; Galán Alvarez, Y. H.; Martinez Reyes, F. C.; Castillo Calvas, J. C.; Mendoza Alava, M.; Cueva Ayala, P.; Hanchard, B.; Fajardo-Gutiérrez, A.; Zavala Zegarra, D. E.; Barrios, E.; Nikiforuk, C.; Woods, R.; Turner, D.; MacIntyre, M.; Corriveau, A.; Navaneelan, T.; Bertrand, C.; Stuart-Panko, H.; Wilson, R. J.; Kosary, C.; Shen, X.; Brockhouse, J.; Yee, G. A.; Mitchell, T. C.; Snipes, K.; West, D.; Rao, C.; Bolick, S.; Rycroft, R. K.; Mueller, L.; Zheng, Y.; Dosch, K.; Brown, H.; Vargas, A.; Levin, G. M.; Bayakly, R.; Johnson, C.; Shen, T.; Ruppert, L.; Lynch, C. F.; Lai, S. M.; Tucker, T. C.; Wu, X. C.; Schwenn, M.; Stern, K.; Gershman, S.; Copeland, G.; Bushhouse, S.; Rogers, D. B.; Jackson Thompson, J.; Lemons, D.; Frederick, S.; Harris, J. A.; Riddle, B.; Stroup, A.; Wiggins, C.; Schymura, M. J.; Giljahn, L. K.; Sheikh, A.; Schubert, S.; Aldinger, W.; Fulton, J. P.; Whiteside, M.; Nogueira, L.; Sweeney, C.; Johnson, A.; Martin, J.; Farley, S.; Harrelson, D.; Malicki, R.; Espinoza, J. R.; Hernandez, B. Y.; Abulfateh, N.; Wang, N.; Ngan, R. K. C.; Lingegowda, K. B.; Swaminathan, R.; Koyande, S. S.; Silverman, B.; Ozasa, K.; Kanemura, S.; Soda, M.; Miyashiro, I.; Shibata, A.; Nimri, O.; Won, Y. J.; Kim, C. H.; Hong, N. S.; Nam, H. S.; Kweon, S.; Kim, W. C.; Huh, J. S.; Jung, K. W.; Yoo, C. I.; Elbasmy, A.; Laudico, A. V.; Lumague, M. R.; AlMutlag, H.; Buasom, R.; Srisukho, S.; Tanabodee, J.; Wiangnon, S.; Pongnikorn, D.; Sriplung, H.; Dirican, O.; Eser, S.; Le Hoang, M.; Hackl, M.; Zborovskaya, A.; Dimitrova, N.; Valerianova, Z.; Sekerija, M.; Pavlou, P.; Dušek, M.; Mägi, M.; Clavel, J.; Lacour, B.; Guizard, A. V.; Bouvier, V.; Troussard, X.; Woronoff, A. S.; Tretarre, B.; Colonna, M.; Molinié, F.; Bara, S.; Velten, M.; Marrer, E.; Ganry, O.; Grosclaude, P.; Kaatsch, P.; Zeissig, S. R.; Holleczek, B.; Katalinic, A.; Jakab, Z.; Birgisson, H.; Walsh, P. M.; Mangone, L.; Merletti, F.; Magoni, M.; Mangone, L.; Ferretti, S.; Serraino, D.; Spagnoli, G.; Fusco, M.; Michiara, M.; Tumino, R.; Falcini, F.; Sensi, F.; Tisano, F.; Piffer, S.; Stracci, F.; Tagliabue, G.; Smailyte, G.; Agius, D.; Visser, O.; Ursin, G.; Didkowska, J.; Trojanowski, M.; Wojciechowska, U.; Forjaz de Lacerda, G.; Silva, M. A.; Laranja Pontes, J.; da Costa Miranda, A.; Kaiserova, E.; Primic Žakelj, M.; Peris-Bonet, R.; Vicente Raneda, M. L.; Almar Marqués, E.; Quirós Garcia, J. R.; Ramos Monserrat, M.; Errezola Saizar, M.; Alemán Herrera, A.; Díaz García, J. M.; Marcos-Gragera, R.; Sanchez-Perez, M. J.; Ardanaz Aicua, E.; Galceran, J.; Klint, A.; Kuehni, C. E.; Bouchardy, C.; Levi, F.; Bordoni, A.; Konzelmann, I.; Rohrmann, S.; Stiller, C. A.; Gavin, A. T.; Brewster, D. H.; Phung, H.; Rushton, S.; Guthridge, S.; Aitken, J.; D'Onise, K.; Venn, A.; Farrugian, H.;

Threlfall, T. J.; Laumond, S.; Yen Kai Sun, L.; Hendrix, J.; Ballantine, K.; Colombet, M.; Dolya, A.; Masuyer, E.; Steliarova-Foucher, E., International incidence of childhood cancer, 2001–10: a population-based registry study. *The Lancet Oncology* **2017,** *18* (6), 719-731.

5. Lam, C. G.; Howard, S. C.; Bouffet, E.; Pritchard-Jones, K., Science and health for all children with cancer. *Science* **2019,** *363* (6432), 1182.

6. Siegel, R. L.; Miller, K. D.; Fuchs, H. E.; Jemal, A., Cancer Statistics, 2021. *CA: A Cancer Journal for Clinicians* **2021,** *71* (1), 7-33.

7. American Cancer Society. Risk Factors and Causes of Childhood Cancer https://www.cancer.org/cancer/cancer-in-children/risk-factors-and-causes.html (accessed 15th April).

8. National Cancer Institute. Cancer in Children and Adolescents https://www.cancer.gov/types/childhood-cancers/child-adolescent-cancers-fact-sheet (accessed 15th April).

9. Shern, J. F.; Yohe, M. E.; Khan, J., Pediatric Rhabdomyosarcoma. *Crit Rev Oncog* **2015,** *20* (3-4), 227-243.

10. Arndt, C. A. S.; Crist, W. M., Common Musculoskeletal Tumors of Childhood and Adolescence. *The New England Journal of Medicine* **1999,** *341* (5), 342-352.

11. Amankwah, E. K.; Conley, A. P.; Reed, D. R., Epidemiology and therapies for metastatic sarcoma. *Clin Epidemiol* **2013,** *5*, 147-162.

12. Diller, L.; Sexsmith, E.; Gottlieb, A.; Li, F. P.; Malkin, D., Germline p53 mutations are frequently detected in young children with rhabdomyosarcoma. *Journal of Clinical Investigation* **1995,** *95* (4), 1606-1611.

13. F P Li, J. F. F. J., Soft-Tissue Sarcomas, Breast Cancer, and Other Neoplasms. *Annals of Internal Medicine* **1969,** *71* (4), 747-752.

14. Steenman, M.; Westerveld, A.; Mannens, M., Genetics of Beckwith-Wiedemann syndrome-associated tumors: common genetic pathways. *Genes, chromosomes & cancer* **2000,** *28* (1), 1-13.

15. Li, M.; Squire, J. A.; Weksberg, R., Molecular genetics of Beckwith-Wiedemann syndrome. *Current opinion in pediatrics* **1997,** *9* (6), 623-9.

16. Hernandez Tejada, F. N.; Zamudio, A.; Marques-Piubelli, M. L.; Cuglievan, B.; Harrison, D., Advances in the Management of Pediatric Sarcomas. *Current oncology reports* **2020,** *23* (1), 3.

17. Chen, C.; Dorado Garcia, H.; Scheer, M.; Henssen, A. G., Current and Future Treatment Strategies for Rhabdomyosarcoma. *Frontiers in Oncology* **2019,** *9* (1458).

18. Dziuba, I.; Kurzawa, P.; Dopierała, M.; Larque, A. B.; Januszkiewicz-Lewandowska, D., Rhabdomyosarcoma in children - current pathologic and molecular classification. *Polish journal of pathology : official journal of the Polish Society of Pathologists* **2018,** *69* (1), 20-32.

19. Barr, F. G., Gene fusions involving PAX and FOX family members in alveolar rhabdomyosarcoma. *Oncogene* **2001,** *20* (40), 5736-5746.

20. Gabriela, E. M.; Frederic, G. B., Fusions Involving PAX and FOX Genes in the Molecular Pathogenesis of Alveolar Rhabdomyosarcoma: Recent Advances. *Current Molecular Medicine* **2007,** *7* (1), 47-61.

21. Visser, M.; Sijmons, C.; Bras, J.; Arceci, R. J.; Godfried, M.; Valentijn, L. J.; Voûte, P. A.; Baas, F., Allelotype of pediatric rhabdomyosarcoma. *Oncogene* **1997,** *15* (11), 1309-1314.

22. American Cancer Society. Treating Rhabdomyosarcoma. https://www.cancer.org/cancer/rhabdomyosarcoma/treating.html (accessed 19th April).

23. National Cancer Institut. Childhood Rhabdomyosarcoma Treatment. https://www.cancer.gov/types/soft-tissue-sarcoma/patient/rhabdomyosarcoma-treatment-pdq (accessed 19th, April).

24. Bompas, E.; Campion, L.; Italiano, A.; Le Cesne, A.; Chevreau, C.; Isambert, N.; Toulmonde, M.; Mir, O.; Ray-Coquard, I.; Piperno-Neumann, S.; Saada-Bouzid, E.; Rios, M.; Kurtz, J.-E.; Delcambre, C.; Dubray-Longeras, P.; Duffaud, F.; Karanian, M.; Le Loarer, F.; Soulié, P.; Penel, N.; Blay, J.-Y., Outcome of 449 adult patients with rhabdomyosarcoma: an observational ambispective nationwide study. *Cancer Medicine* **2018,** *7* (8), 4023-4035.

25. Walterhouse, D.; Watson, A., Optimal management strategies for rhabdomyosarcoma in children. *Paediatric drugs* **2007,** *9* (6), 391-400.

26. Nurgali, K.; Jagoe, R. T.; Abalo, R., Editorial: Adverse Effects of Cancer Chemotherapy: Anything New to Improve Tolerance and Reduce Sequelae? *Frontiers in Pharmacology* **2018,** *9* (245).

27. Kearns, G. L.; Abdel-Rahman, S. M.; Alander, S. W.; Blowey, D. L.; Leeder, J. S.; Kauffman, R. E., Developmental Pharmacology — Drug Disposition, Action, and Therapy in Infants and Children. *New England Journal of Medicine* **2003,** *349* (12), 1157-1167.

28. Kattner, P.; Strobel, H.; Khoshnevis, N.; Grunert, M.; Bartholomae, S.; Pruss, M.; Fitzel, R.; Halatsch, M. E.; Schilberg, K.; Siegelin, M. D.; Peraud, A.; Karpel-Massler, G.; Westhoff, M. A.; Debatin, K. M., Compare and contrast: pediatric cancer versus adult malignancies. *Cancer Metastasis Rev* **2019,** *38* (4), 673-682.

29. Sosnik, A.; Carcaboso, A. M., Nanomedicines in the future of pediatric therapy. *Advanced Drug Delivery Reviews* **2014,** *73*, 140-61.

30. Barone, A.; Casey, D.; McKee, A. E.; Reaman, G., Cancer drugs approved for use in children: Impact of legislative initiatives and future opportunities. *Pediatric Blood & Cancer* **2019,** *66* (8), e27809.

31. van Erp, A. E. M.; Versleijen-Jonkers, Y. M. H.; van der Graaf, W. T. A.; Fleuren, E. D. G., Targeted Therapy–based Combination Treatment in Rhabdomyosarcoma. *Molecular Cancer Therapeutics* **2018,** *17* (7), 1365-1380.

32. Pui, C.-H.; Gajjar, A. J.; Kane, J. R.; Qaddoumi, I. A.; Pappo, A. S., Challenging issues in pediatric oncology. *Nature Reviews Clinical Oncology* **2011,** *8* (9), 540-549.

33. Crose, L. E. S.; Linardic, C. M., Receptor tyrosine kinases as therapeutic targets in rhabdomyosarcoma. *Sarcoma* **2011,** *2011*, 756982-756982.

34. Cao, L.; Yu, Y.; Bilke, S.; Walker, R. L.; Mayeenuddin, L. H.; Azorsa, D. O.; Yang, F.; Pineda, M.; Helman, L. J.; Meltzer, P. S., Genome-wide identification of PAX3-FKHR binding sites in rhabdomyosarcoma reveals candidate target genes important for development and cancer. *Cancer research* **2010,** *70* (16), 6497-508.

35. Martins, A. S.; Olmos, D.; Missiaglia, E.; Shipley, J., Targeting the insulin-like growth factor pathway in rhabdomyosarcomas: rationale and future perspectives. *Sarcoma* **2011,** *2011*, 209736.

36. Miwa, S.; Yamamoto, N.; Hayashi, K.; Takeuchi, A.; Igarashi, K.; Tsuchiya, H., Recent Advances and Challenges in the Treatment of Rhabdomyosarcoma. *Cancers* **2020,** *12* (7), 1758.

37. Tran, S.; DeGiovanni, P.-J.; Piel, B.; Rai, P., Cancer nanomedicine: a review of recent success in drug delivery. *Clinical and Translational Medicine* **2017,** *6* (1), 44.

38. Rizzo, L. Y.; Theek, B.; Storm, G.; Kiessling, F.; Lammers, T., Recent progress in nanomedicine: therapeutic, diagnostic and theranostic applications. *Current Opinion in Biotechnology* **2013,** *24* (6), 1159-1166.

39. Sinha, R.; Kim, G. J.; Nie, S.; Shin, D. M., Nanotechnology in cancer therapeutics: bioconjugated nanoparticles for drug delivery. *Molecular Cancer Therapeutics* **2006,** *5* (8), 1909-1917.

40. Yang, S.; Wallach, M.; Krishna, A.; Kurmasheva, R.; Sridhar, S., Recent Developments in Nanomedicine for Pediatric Cancer. *Journal of Clinical Medicine* **2021,** *10* (7), 1437.

41. Blanco, E.; Shen, H.; Ferrari, M., Principles of nanoparticle design for overcoming biological barriers to drug delivery. *Nature Biotechnology* **2015,** *33* (9), 941-51.

42. Rodriguez-Nogales, C.; Gonzalez-Fernandez, Y.; Aldaz, A.; Couvreur, P.; Blanco-Prieto, M. J., Nanomedicines for Pediatric Cancers. *ACS Nano* **2018,** *12* (8), 7482-7496.

43. Hoshyar, N.; Gray, S.; Han, H.; Bao, G., The effect of nanoparticle size on in vivo pharmacokinetics and cellular interaction. *Nanomedicine (London, England)* **2016,** *11* (6), 673-92.

44. Salvioni, L.; Rizzuto, M. A.; Bertolini, J. A.; Pandolfi, L.; Colombo, M.; Prosperi, D., Thirty Years of Cancer Nanomedicine: Success, Frustration, and Hope. *Cancers (Basel)* **2019,** *11* (12).

45. Dib, S.; Aggad, D.; Mauriello Jimenez, C.; Lakrafi, A.; Hery, G.; Nguyen, C.; Durand, D.; Morère, A.; El Cheikh, K.; Sol, V.; Chaleix, V.; Dominguez Gil, S.; Bouchmella, K.; Raehm, L.; Durand, J. O.; Boufatit, M.; Cattoën, X.; Wong Chi Man, M.; Bettache, N.; Gary-Bobo, M., Porphyrin-based bridged silsesquioxane nanoparticles for targeted two-photon photodynamic therapy of zebrafish xenografted with human tumor. *Cancer Reports* **2019,** *2* (5).

46. Mauriello Jimenez, C.; Aggad, D.; Croissant, J. G.; Tresfield, K.; Laurencin, D.; Berthomieu, D.; Cubedo, N.; Rossel, M.; Alsaiari, S.; Anjum, D. H.; Sougrat, R.; Roldan-Gutierrez, M. A.; Richeter, S.; Oliviero, E.; Raehm, L.; Charnay, C.; Cattoën, X.; Clément, S.; Wong Chi Man, M.; Maynadier, M.; Chaleix, V.; Sol, V.; Garcia, M.; Gary-Bobo, M.; Khashab, N. M.; Bettache, N.; Durand, J.-O., Porous Porphyrin-Based Organosilica Nanoparticles for NIR Two-Photon Photodynamic Therapy and Gene Delivery in Zebrafish. *Advanced Functional Materials* **2018,** *28* (21).

47. Albanese, A.; Tang, P. S.; Chan, W. C. W., The Effect of Nanoparticle Size, Shape, and Surface Chemistry on Biological Systems. *Annual Review of Biomedical Engineering* **2012,** *14* (1), 1-16.

48. Choi, H. S.; Liu, W.; Misra, P.; Tanaka, E.; Zimmer, J. P.; Itty Ipe, B.; Bawendi, M. G.; Frangioni, J. V., Renal clearance of quantum dots. *Nature Biotechnology* **2007,** *25* (10), 1165-70.

49. Moghimi, S. M.; Hunter, A. C., Recognition by Macrophages and Liver Cells of Opsonized Phospholipid Vesicles and Phospholipid Headgroups. *Pharmaceutical Research* **2001,** *18* (1), 1-8.

50. Perrault, S. D.; Walkey, C.; Jennings, T.; Fischer, H. C.; Chan, W. C. W., Mediating Tumor Targeting Efficiency of Nanoparticles Through Design. *Nano Letters* **2009,** *9* (5), 1909-1915.

51. Owens, D. E.; Peppas, N. A., Opsonization, biodistribution, and pharmacokinetics of polymeric nanoparticles. *International Journal of Pharmaceutics* **2006,** *307* (1), 93-102.

52. Aghebati-Maleki, A.; Dolati, S.; Ahmadi, M.; Baghbanzhadeh, A.; Asadi, M.; Fotouhi, A.; Yousefi, M.; Aghebati-Maleki, L., Nanoparticles and cancer therapy: Perspectives for application of nanoparticles in the treatment of cancers. *Journal of Cellular Physiology* **2020,** *235* (3), 1962-1972.

53. Bangham, A. D.; Standish, M. M.; Watkins, J. C., Diffusion of univalent ions across the lamellae of swollen phospholipids. *Journal of Molecular Biology* **1965,** *13* (1), 238-IN27.

54. Bangham, A. D.; Horne, R. W., Negative staining of phospholipids and their structural modification by surface-active agents as observed in the electron microscope. *Journal of Molecular Biology* **1964,** *8* (5), 660-IN10.

55. Barenholz, Y., Doxil® — The first FDA-approved nano-drug: Lessons learned. *Journal of Controlled Release* **2012,** *160* (2), 117-134.

56. Safra, T.; Muggia, F.; Jeffers, S.; Tsao-Wei, D. D.; Groshen, S.; Lyass, O.; Henderson, R.; Berry, G.; Gabizon, A., Pegylated liposomal doxorubicin (doxil): reduced clinical

cardiotoxicity in patients reaching or exceeding cumulative doses of 500 mg/m2. *Annals of Oncology* **2000,** *11* (8), 1029-33.

57. Chan, S.; Davidson, N.; Juozaityte, E.; Erdkamp, F.; Pluzanska, A.; Azarnia, N.; Lee, L. W., Phase III trial of liposomal doxorubicin and cyclophosphamide compared with epirubicin and cyclophosphamide as first-line therapy for metastatic breast cancer. *Annals of Oncology* **2004,** *15* (10), 1527-1534.

58. Nicola, G.; Christina-Maria, H.; Renato, B.; Heinz-Gerd, D.; Herve, D.; Richard, G.; Jesus-Maria, H.-R.; Francoise, H.; Tamara, I.; Eric, J.; Christian, J.; Lothar, L.; Maria-Jose, M.; Albrecht, R.; Josep, R.; Matthias, S.; Hubert, S.; Matthias, S.; Reingard, S.; Dieter, H., Liposomal cytarabine is effective and tolerable in the treatment of central nervous system relapse of acute lymphoblastic leukemia and very aggressive lymphoma. *Haematologica* **2011,** *96* (2), 238-244.

59. O'Brien, S.; Schiller, G.; Lister, J.; Damon, L.; Goldberg, S.; Aulitzky, W.; Ben-Yehuda, D.; Stock, W.; Coutre, S.; Douer, D.; Heffner, L. T.; Larson, M.; Seiter, K.; Smith, S.; Assouline, S.; Kuriakose, P.; Maness, L.; Nagler, A.; Rowe, J.; Schaich, M.; Shpilberg, O.; Yee, K.; Schmieder, G.; Silverman, J. A.; Thomas, D.; Deitcher, S. R.; Kantarjian, H., High-Dose Vincristine Sulfate Liposome Injection for Advanced, Relapsed, and Refractory Adult Philadelphia Chromosome–Negative Acute Lymphoblastic Leukemia. *Journal of Clinical Oncology* **2013,** *31* (6), 676-683.

60. Meyers, P. A.; Schwartz, C. L.; Krailo, M. D.; Healey, J. H.; Bernstein, M. L.; Betcher, D.; Ferguson, W. S.; Gebhardt, M. C.; Goorin, A. M.; Harris, M.; Kleinerman, E.; Link, M. P.; Nadel, H.; Nieder, M.; Siegal, G. P.; Weiner, M. A.; Wells, R. J.; Womer, R. B.; Grier, H. E., Osteosarcoma: The Addition of Muramyl Tripeptide to Chemotherapy Improves Overall Survival—A Report From the Children's Oncology Group. *Journal of Clinical Oncology* **2008,** *26* (4), 633-638.

61. Morita, K.; Zywietz, F.; Kakinuma, K.; Tanaka, R.; Katoh, M., Efficacy of doxorubicin thermosensitive liposomes (40 degrees C) and local hyperthermia on rat rhabdomyosarcoma. *Oncology reports* **2008,** *20* (2), 365-72.

62. Kong, G.; Anyarambhatla, G.; Petros, W. P.; Braun, R. D.; Colvin, O. M.; Needham, D.; Dewhirst, M. W., Efficacy of Liposomes and Hyperthermia in a Human Tumor Xenograft Model: Importance of Triggered Drug Release. *Cancer research* **2000,** *60* (24), 6950-6957.

63. Derycke, A. S. L.; de Witte, P. A. M., Liposomes for photodynamic therapy. *Advanced Drug Delivery Reviews* **2004,** *56* (1), 17-30.

64. Letchford, K.; Burt, H., A review of the formation and classification of amphiphilic block copolymer nanoparticulate structures: micelles, nanospheres, nanocapsules and polymersomes. *European Journal of Pharmaceutics and Biopharmaceutics* **2007,** *65* (3), 259-269.

65. Hawkins, M. J.; Soon-Shiong, P.; Desai, N., Protein nanoparticles as drug carriers in clinical medicine. *Advanced Drug Delivery Reviews* **2008,** *60* (8), 876-885.

66. Zhang, L.; Marrano, P.; Kumar, S.; Leadley, M.; Elias, E.; Thorner, P.; Baruchel, S., Nab-Paclitaxel Is an Active Drug in Preclinical Model of Pediatric Solid Tumors. *Clinical Cancer Research* **2013,** *19* (21), 5972-5983.

67. Elazar, V.; Adwan, H.; Bäuerle, T.; Rohekar, K.; Golomb, G.; Berger, M. R., Sustained delivery and efficacy of polymeric nanoparticles containing osteopontin and bone sialoprotein antisenses in rats with breast cancer bone metastasis. *International Journal of Cancer* **2010,** *126* (7), 1749-1760.

68. Matsumura, Y.; Hamaguchi, T.; Ura, T.; Muro, K.; Yamada, Y.; Shimada, Y.; Shirao, K.; Okusaka, T.; Ueno, H.; Ikeda, M.; Watanabe, N., Phase I clinical trial and pharmacokinetic evaluation of NK911, a micelle-encapsulated doxorubicin. *British Journal of Cancer* **2004,** *91* (10), 1775-1781.

69. Attawia, M. A.; Borden, M. D.; Herbert, K. M.; Katti, D. S.; Asrari, F.; Uhrich, K. E.; Laurencin, C. T., Regional drug delivery with radiation for the treatment of Ewing's sarcoma: In vitro development of a taxol release system. *Journal of Controlled Release* **2001,** *71* (2), 193-202.

70. Schluep, T.; Hwang, J.; Cheng, J.; Heidel, J. D.; Bartlett, D. W.; Hollister, B.; Davis, M. E., Preclinical Efficacy of the Camptothecin-Polymer Conjugate IT-101 in Multiple Cancer Models. *Clinical Cancer Research* **2006,** *12* (5), 1606-1614.

71. Patri, A. K.; Majoros, I. J.; Baker, J. R., Dendritic polymer macromolecular carriers for drug delivery. *Current Opinion in Chemical Biology* **2002,** *6* (4), 466-471.

72. Gillies, E. R.; Fréchet, J. M. J., Dendrimers and dendritic polymers in drug delivery. *Drug Discovery Today* **2005,** *10* (1), 35-43.

73. Cheng, Y.; Wang, J.; Rao, T.; He, X.; Xu, T., Pharmaceutical applications of dendrimers: promising nanocarriers for drug delivery. *Frontiers in Bioscience-Landmark* **2008,** *13* (4), 1447-1471.

74. Tomalia, D. A.; Baker, H.; Dewald, J.; Hall, M.; Kallos, G.; Martin, S.; Roeck, J.; Ryder, J.; Smith, P., A New Class of Polymers: Starburst-Dendritic Macromolecules. *Polymer Journal* **1985,** *17* (1), 117-132.

75. Newkome, G. R.; Yao, Z.; Baker, G. R.; Gupta, V. K., Micelles. Part 1. Cascade molecules: a new approach to micelles. A [27]-arborol. *The Journal of Organic Chemistry* **1985,** *50* (11), 2003-2004.

76. Nanjwade, B. K.; Bechra, H. M.; Derkar, G. K.; Manvi, F. V.; Nanjwade, V. K., Dendrimers: Emerging polymers for drug-delivery systems. *European Journal of Pharmaceutical Sciences* **2009,** *38* (3), 185-196.

77. Taratula, O.; Garbuzenko, O. B.; Kirkpatrick, P.; Pandya, I.; Savla, R.; Pozharov, V. P.; He, H.; Minko, T., Surface-engineered targeted PPI dendrimer for efficient intracellular and intratumoral siRNA delivery. *Journal of Controlled Release* **2009,** *140* (3), 284-293.

78. Alfei, S.; Marengo, B.; Zuccari, G.; Turrini, F.; Domenicotti, C., Dendrimer Nanodevices and Gallic Acid as Novel Strategies to Fight Chemoresistance in Neuroblastoma Cells. *Nanomaterials* **2020,** *10* (6), 1243.

79. Kang, S. J.; Durairaj, C.; Kompella, U. B.; O'Brien, J. M.; Grossniklaus, H. E., Subconjunctival nanoparticle carboplatin in the treatment of murine retinoblastoma. *Archives of Ophthalmology* **2009,** *127* (8), 1043-7.

80. Mizoshita, N.; Tani, T.; Inagaki, S., Syntheses, properties and applications of periodic mesoporous organosilicas prepared from bridged organosilane precursors. *Chemical Society Reviews* **2011,** *40* (2), 789-800.

81. Hoffmann, F.; Fröba, M., Vitalising porous inorganic silica networks with organic functions—PMOs and related hybrid materials. *Chemical Society Reviews* **2011,** *40* (2), 608-620.

82. Yang, B.; Chen, Y.; Shi, J., Mesoporous silica/organosilica nanoparticles: Synthesis, biological effect and biomedical application. *Materials Science and Engineering: R: Reports* **2019,** *137*, 66-105.

83. Inagaki, S.; Guan, S.; Fukushima, Y.; Ohsuna, T.; Terasaki, O., Novel Mesoporous Materials with a Uniform Distribution of Organic Groups and Inorganic Oxide in Their Frameworks. *Journal of the American Chemical Society* **1999,** *121* (41), 9611-9614.

84. Melde, B. J.; Holland, B. T.; Blanford, C. F.; Stein, A., Mesoporous Sieves with Unified Hybrid Inorganic/Organic Frameworks. *Chemistry of Materials* **1999,** *11* (11), 3302-3308.

85. Zhang, L.; Wang, L.; Yao, H.; Xu, F.; Chen, Y., Biodegradable and biocompatible monodispersed hollow mesoporous organosilica with large pores for delivering biomacromolecules. *Journal of Materials Chemistry B* **2017,** *5* (39), 8013-8025.

86. Teng, Z.; Li, W.; Tang, Y.; Elzatahry, A.; Lu, G.; Zhao, D., Mesoporous Organosilica Hollow Nanoparticles: Synthesis and Applications. *Advanced Materials* **2019,** *31* (38), 1707612.

87. Chen, Y.; Shi, J., Chemistry of Mesoporous Organosilica in Nanotechnology: Molecularly Organic–Inorganic Hybridization into Frameworks. *Advanced Materials* **2016,** *28* (17), 3235-3272.

88. Vu, B. T.; Shahin, S. A.; Croissant, J.; Fatieiev, Y.; Matsumoto, K.; Le-Hoang Doan, T.; Yik, T.; Simargi, S.; Conteras, A.; Ratliff, L.; Jimenez, C. M.; Raehm, L.; Khashab, N.; Durand, J.-O.; Glackin, C.; Tamanoi, F., Chick chorioallantoic membrane assay as an in vivo model to study the effect of nanoparticle-based anticancer drugs in ovarian cancer. *Scientific Reports* **2018,** *8* (1), 8524.

89. Daurat, M.; Rahmani, S.; Bouchal, R.; Akrout, A.; Budimir, J.; Nguyen, C.; Charnay, C.; Guari, Y.; Richeter, S.; Raehm, L.; Bettache, N.; Gary-Bobo, M.; Durand, J.-O.; Hesemann, P., Organosilica Nanoparticles for Gemcitabine Monophosphate Delivery in Cancer Cells. *ChemNanoMat* **2019,** *5* (7), 888-896.

90. Mai, N. X. D.; Birault, A.; Matsumoto, K.; Ta, H. K. T.; Intasa-ard, S. G.; Morrison, K.; Thang, P. B.; Doan, T. L. H.; Tamanoi, F., Biodegradable Periodic Mesoporous Organosilica (BPMO) Loaded with Daunorubicin: A Promising Nanoparticle-Based Anticancer Drug. *ChemMedChem* **2020,** *15* (7), 593-599.

91. Rahmani, S.; Chaix, A.; Aggad, D.; Hoang, P.; Moosa, B.; Garcia, M.; Gary-Bobo, M.; Charnay, C.; AlMalik, A.; Durand, J.-O.; Khashab, N. M., Degradable gold core–mesoporous organosilica shell nanoparticles for two-photon imaging and gemcitabine monophosphate delivery. *Molecular Systems Design & Engineering* **2017,** *2* (4), 380-383.

92. Lin, V. S. Y.; Motesharei, K.; Dancil, K.-P. S.; Sailor, M. J.; Ghadiri, M. R., A Porous Silicon-Based Optical Interferometric Biosensor. *Science* **1997,** *278* (5339), 840.

93. Park, Y.; Yoo, J.; Kang, M. H.; Kwon, W.; Joo, J., Photoluminescent and biodegradable porous silicon nanoparticles for biomedical imaging. *Journal of Materials Chemistry B* **2019,** *7* (41), 6271-6292.

94. Park, J. H.; Gu, L.; von Maltzahn, G.; Ruoslahti, E.; Bhatia, S. N.; Sailor, M. J., Biodegradable luminescent porous silicon nanoparticles for in vivo applications. *Nature Materials* **2009,** *8* (4), 331-6.

95. Popplewell, J. F.; King, S. J.; Day, J. P.; Ackrill, P.; Fifield, L. K.; Cresswell, R. G.; di Tada, M. L.; Liu, K., Kinetics of uptake and elimination of silicic acid by a human subject: a novel application of 32Si and accelerator mass spectrometry. *Journal of inorganic biochemistry* **1998,** *69* (3), 177-80.

96. Jin, Y.; Kim, D.; Roh, H.; Kim, S.; Hussain, S.; Kang, J.; Pack, C. G.; Kim, J. K.; Myung, S. J.; Ruoslahti, E.; Sailor, M. J.; Kim, S. C.; Joo, J., Tracking the Fate of Porous Silicon Nanoparticles Delivering a Peptide Payload by Intrinsic Photoluminescence Lifetime. *Advanced Materials* **2018,** *30* (35), e1802878.

97. Canham, L. T., Bioactive silicon structure fabrication through nanoetching techniques. *Advanced Materials* **1995,** *7* (12), 1033-1037.

98. Alvarez, S. D.; Derfus, A. M.; Schwartz, M. P.; Bhatia, S. N.; Sailor, M. J., The compatibility of hepatocytes with chemically modified porous silicon with reference to in vitro biosensors. *Biomaterials* **2009,** *30* (1), 26-34.

99. Alvarez, S. D.; Schwartz, M. P.; Migliori, B.; Rang, C. U.; Chao, L.; Sailor, M. J., Using a porous silicon photonic crystal for bacterial cell-based biosensing. *physica status solidi (a)* **2007,** *204* (5), 1439-1443.

100. Bayliss, S. C.; Heald, R.; Fletcher, D. I.; Buckberry, L. D., The Culture of Mammalian Cells on Nanostructured Silicon. *Advanced Materials* **1999,** *11* (4), 318-321.

101. Kim, B.; Yang, Q.; Chan, L. W.; Bhatia, S. N.; Ruoslahti, E.; Sailor, M. J., Fusogenic porous silicon nanoparticles as a broad-spectrum immunotherapy against bacterial infections. *Nanoscale Horizons* **2021,** *6* (4), 330-340.

102. Anglin, E. J.; Cheng, L.; Freeman, W. R.; Sailor, M. J., Porous silicon in drug delivery devices and materials. *Advanced Drug Delivery Reviews* **2008,** *60* (11), 1266-1277.

103. Buriak, J. M., Organometallic chemistry on silicon and germanium surfaces. *Chemical reviews* **2002,** *102* (5), 1271-1308.

104. Saffie, R.; Canham, L. T.; Dormer, J. C.; Chow, P. K. H.; Kai, Z.; Ng Teck, H. R. Methods for the treatment of cancer. 2005.

105. Wang, C.-F.; Mäkilä, E. M.; Kaasalainen, M. H.; Hagström, M. V.; Salonen, J. J.; Hirvonen, J. T.; Santos, H. A., Dual-drug delivery by porous silicon nanoparticles for improved cellular uptake, sustained release, and combination therapy. *Acta Biomaterialia* **2015,** *16*, 206-214.

106. Landgraf, M.; Lahr, C. A.; Kaur, I.; Shafiee, A.; Sanchez-Herrero, A.; Janowicz, P. W.; Ravichandran, A.; Howard, C. B.; Cifuentes-Rius, A.; McGovern, J. A.; Voelcker, N. H.; Hutmacher, D. W., Targeted camptothecin delivery via silicon nanoparticles reduces breast cancer metastasis. *Biomaterials* **2020,** *240*, 119791.

107. Secret, E.; Smith, K.; Dubljevic, V.; Moore, E.; Macardle, P.; Delalat, B.; Rogers, M. L.; Johns, T. G.; Durand, J. O.; Cunin, F.; Voelcker, N. H., Antibody-functionalized porous silicon nanoparticles for vectorization of hydrophobic drugs. *Advanced Healthcare Materials* **2013,** *2* (5), 718-27.

108. Bimbo, L. M.; Sarparanta, M.; Santos, H. A.; Airaksinen, A. J.; Mäkilä, E.; Laaksonen, T.; Peltonen, L.; Lehto, V.-P.; Hirvonen, J.; Salonen, J., Biocompatibility of Thermally Hydrocarbonized Porous Silicon Nanoparticles and their Biodistribution in Rats. *ACS Nano* **2010,** *4* (6), 3023-3032.

109. Correia, A.; Shahbazi, M.-A.; Mäkilä, E.; Almeida, S.; Salonen, J.; Hirvonen, J.; Santos, H. A., Cyclodextrin-Modified Porous Silicon Nanoparticles for Efficient Sustained Drug Delivery and Proliferation Inhibition of Breast Cancer Cells. *ACS Applied Materials & Interfaces* **2015,** *7* (41), 23197-23204.

110. He, H.; Liu, L.; Morin, E. E.; Liu, M.; Schwendeman, A., Survey of Clinical Translation of Cancer Nanomedicines—Lessons Learned from Successes and Failures. *Accounts of Chemical Research* **2019,** *52* (9), 2445-2461.

111. Marcato, P. D.; Durán, N., New aspects of nanopharmaceutical delivery systems. *Journal of nanoscience and nanotechnology* **2008,** *8* (5), 2216-29.

112. Maeda, H., SMANCS and polymer-conjugated macromolecular drugs: advantages in cancer chemotherapy. *Advanced Drug Delivery Reviews* **2001,** *46* (1-3), 169-85.

113. Park, K., Facing the Truth about Nanotechnology in Drug Delivery. *ACS Nano* **2013,** *7* (9), 7442-7447.

114. Nichols, J. W.; Bae, Y. H., Nanotechnology for Cancer Treatment: Possibilities and Limitations. In *Cancer Targeted Drug Delivery: An Elusive Dream*, Bae, Y. H.; Mrsny, R. J.; Park, K., Eds. Springer New York: New York, NY, 2013; pp 37-56.

115. Matsumura, Y.; Maeda, H., A New Concept for Macromolecular Therapeutics in Cancer Chemotherapy: Mechanism of Tumoritropic Accumulation of Proteins and the Antitumor Agent Smancs. *Cancer research* **1986,** *46* (12 Part 1), 6387-6392.

116. Danhier, F., To exploit the tumor microenvironment: Since the EPR effect fails in the clinic, what is the future of nanomedicine? *Journal of Controlled Release* **2016,** *244*, 108-121.

117. Greish, K.; Iyer, A.; Fang, J.; Kawasuji, M.; Maeda, H., Enhanced permeability and retention (EPR) effect and tumor-selective delivery of anticancer drugs. *Delivery of protein and peptide drugs in cancer* **2006,** *10*, 14.

118. Clond, M. A.; Lee, B.-S.; Jeffrey, J. Y.; Singer, M. B.; Amano, T.; Lamb, A. W.; Drazin, D.; Kateb, B.; Ley, E. J.; John, S. Y., Reactive oxygen species-activated nanoprodrug of Ibuprofen for targeting traumatic brain injury in mice. *PLoS One* **2013,** *8* (4), e61819.

119. Sun, T.; Zhang, Y. S.; Pang, B.; Hyun, D. C.; Yang, M.; Xia, Y., Engineered nanoparticles for drug delivery in cancer therapy. *Angewandte Chemie (International ed. in English)* **2014,** *53* (46), 12320-64.

120. Gaumet, M.; Vargas, A.; Gurny, R.; Delie, F., Nanoparticles for drug delivery: The need for precision in reporting particle size parameters. *European Journal of Pharmaceutics and Biopharmaceutics* **2008,** *69* (1), 1-9.

121. Wilhelm, S.; Tavares, A. J.; Dai, Q.; Ohta, S.; Audet, J.; Dvorak, H. F.; Chan, W. C. W., Analysis of nanoparticle delivery to tumours. *Nature Reviews Materials* **2016,** *1* (5), 16014.

122. Anchordoquy, T. J.; Barenholz, Y.; Boraschi, D.; Chorny, M.; Decuzzi, P.; Dobrovolskaia, M. A.; Farhangrazi, Z. S.; Farrell, D.; Gabizon, A.; Ghandehari, H.; Godin, B.; La-Beck, N. M.; Ljubimova, J.; Moghimi, S. M.; Pagliaro, L.; Park, J.-H.; Peer, D.; Ruoslahti, E.; Serkova, N. J.; Simberg, D., Mechanisms and Barriers in Cancer Nanomedicine: Addressing Challenges, Looking for Solutions. *ACS Nano* **2017,** *11* (1), 12-18.

123. Moghimi, S. M.; Farhangrazi, Z. S., Just so stories: The random acts of anti-cancer nanomedicine performance. *Nanomedicine: Nanotechnology, Biology and Medicine* **2014,** *10* (8), 1661-1666.

124. Wicki, A.; Witzigmann, D.; Balasubramanian, V.; Huwyler, J., Nanomedicine in cancer therapy: challenges, opportunities, and clinical applications. *Journal of Controlled Release* **2015,** *200*, 138-57.

125. Zeisberger, S. M.; Odermatt, B.; Marty, C.; Zehnder-Fjällman, A. H. M.; Ballmer-Hofer, K.; Schwendener, R. A., Clodronate-liposome-mediated depletion of tumour-associated macrophages: a new and highly effective antiangiogenic therapy approach. *British Journal of Cancer* **2006,** *95* (3), 272-281.

126. Au, K. M.; Wang, A. Z.; Park, S. I., Pretargeted delivery of PI3K/mTOR small-molecule inhibitor–loaded nanoparticles for treatment of non-Hodgkin's lymphoma. *Science Advances* **2020,** *6* (14), eaaz9798.

127. Yang, W.; Wu, G.; Barth, R. F.; Swindall, M. R.; Bandyopadhyaya, A. K.; Tjarks, W.; Tordoff, K.; Moeschberger, M.; Sferra, T. J.; Binns, P. J.; Riley, K. J.; Ciesielski, M. J.; Fenstermaker, R. A.; Wikstrand, C. J., Molecular Targeting and Treatment of Composite EGFR and EGFRvIII-Positive Gliomas Using Boronated Monoclonal Antibodies. *Clinical Cancer Research* **2008,** *14* (3), 883.

128. Wu, G.; Yang, W.; Barth, R. F.; Kawabata, S.; Swindall, M.; Bandyopadhyaya, A. K.; Tjarks, W.; Khorsandi, B.; Blue, T. E.; Ferketich, A. K.; Yang, M.; Christoforidis, G. A.; Sferra, T. J.; Binns, P. J.; Riley, K. J.; Ciesielski, M. J.; Fenstermaker, R. A., Molecular targeting and treatment of an epidermal growth factor receptor-positive glioma using boronated cetuximab. *Clinical Cancer Research* **2007,** *13* (4), 1260-8.

129. Barth, R. F.; Wu, G.; Yang, W.; Binns, P. J.; Riley, K. J.; Patel, H.; Coderre, J. A.; Tjarks, W.; Bandyopadhyaya, A. K.; Thirumamagal, B. T. S.; Ciesielski, M. J.; Fenstermaker, R. A., Neutron capture therapy of epidermal growth factor (+) gliomas using boronated cetuximab (IMC-C225) as a delivery agent. *Applied Radiation and Isotopes* **2004,** *61* (5), 899-903.

130. Brignole, C.; Pastorino, F.; Marimpietri, D.; Pagnan, G.; Pistorio, A.; Allen, T. M.; Pistoia, V.; Ponzoni, M., Immune cell-mediated antitumor activities of GD2-targeted liposomal c-myb antisense oligonucleotides containing CpG motifs. *Journal of the National Cancer Institute* **2004,** *96* (15), 1171-80.

131. Wang, X.; Zhao, Y.; Dong, S.; Lee, R. J.; Yang, D.; Zhang, H.; Teng, L., Cell-Penetrating Peptide and Transferrin Co-Modified Liposomes for Targeted Therapy of Glioma. *Molecules* **2019,** *24* (19).

132. Fan, K.; Jia, X.; Zhou, M.; Wang, K.; Conde, J.; He, J.; Tian, J.; Yan, X., Ferritin Nanocarrier Traverses the Blood Brain Barrier and Kills Glioma. *ACS Nano* **2018,** *12* (5), 4105-4115.

133. Markovsky, E.; Vax, E.; Ben-Shushan, D.; Eldar-Boock, A.; Shukrun, R.; Yeini, E.; Barshack, I.; Caspi, R.; Harari-Steinberg, O.; Pode-Shakked, N.; Dekel, B.; Satchi-Fainaro, R., Wilms Tumor NCAM-Expressing Cancer Stem Cells as Potential Therapeutic Target for Polymeric Nanomedicine. *Molecular Cancer Therapeutics* **2017,** *16* (11), 2462-2472.

134. Luo, M.; Lewik, G.; Ratcliffe, J. C.; Choi, C. H. J.; Mäkilä, E.; Tong, W. Y.; Voelcker, N. H., Systematic Evaluation of Transferrin-Modified Porous Silicon Nanoparticles for Targeted Delivery of Doxorubicin to Glioblastoma. *ACS Applied Materials & Interfaces* **2019,** *11* (37), 33637-33649.

135. Song, C.; Zhong, Y.; Jiang, X.; Peng, F.; Lu, Y.; Ji, X.; Su, Y.; He, Y., Peptide-Conjugated Fluorescent Silicon Nanoparticles Enabling Simultaneous Tracking and Specific Destruction of Cancer Cells. *Analytical Chemistry* **2015,** *87* (13), 6718-6723.

136. Zaritski, A.; Castillo-Ecija, H.; Kumarasamy, M.; Peled, E.; Sverdlov Arzi, R.; Carcaboso, Á. M.; Sosnik, A., Selective Accumulation of Galactomannan Amphiphilic Nanomaterials in Pediatric Solid Tumor Xenografts Correlates with GLUT1 Gene Expression. *ACS Applied Materials & Interfaces* **2019,** *11* (42), 38483-38496.

137. Xu, Y.; Shi, W.; Li, H.; Li, X.; Ma, H., H2O2-Responsive Organosilica-Doxorubicin Nanoparticles for Targeted Imaging and Killing of Cancer Cells Based on a Synthesized Silane-Borate Precursor. *ChemMedChem* **2019,** *14* (11), 1079-1085.

138. Chaix, A.; El Cheikh, K.; Bouffard, E.; Maynadier, M.; Aggad, D.; Stojanovic, V.; Knezevic, N.; Garcia, M.; Maillard, P.; Morère, A.; Gary-Bobo, M.; Raehm, L.; Richeter, S.; Durand, J.-O.; Cunin, F., Mesoporous silicon nanoparticles for targeted two-photon theranostics of prostate cancer. *Journal of Materials Chemistry B* **2016,** *4* (21), 3639-3642.

139. Bouffard, E.; Mauriello Jimenez, C.; El Cheikh, K.; Maynadier, M.; Basile, I.; Raehm, L.; Nguyen, C.; Gary-Bobo, M.; Garcia, M.; Durand, J. O.; Morere, A., Efficient Photodynamic Therapy of Prostate Cancer Cells through an Improved Targeting of the Cation-Independent Mannose 6-Phosphate Receptor. *International Journal of Molecular Sciences* **2019,** *20* (11).

140. Vaillant, O.; El Cheikh, K.; Warther, D.; Brevet, D.; Maynadier, M.; Bouffard, E.; Salgues, F.; Jeanjean, A.; Puche, P.; Mazerolles, C.; Maillard, P.; Mongin, O.; Blanchard-Desce, M.; Raehm, L.; Rebillard, X.; Durand, J. O.; Gary-Bobo, M.; Morere, A.; Garcia, M., Mannose-6-phosphate receptor: a target for theranostics of prostate cancer. *Angewandte Chemie (International ed. in English)* **2015,** *54* (20), 5952-6.

141. Perrier, M.; Gary-Bobo, M.; Lartigue, L.; Brevet, D.; Morère, A.; Garcia, M.; Maillard, P.; Raehm, L.; Guari, Y.; Larionova, J.; Durand, J.-O.; Mongin, O.; Blanchard-Desce, M., Mannose-functionalized porous silica-coated magnetic nanoparticles for two-photon imaging or PDT of cancer cells. *Journal of Nanoparticle Research* **2013,** *15* (5), 1602.

142. Brevet, D.; Gary-Bobo, M.; Raehm, L.; Richeter, S.; Hocine, O.; Amro, K.; Loock, B.; Couleaud, P.; Frochot, C.; Morere, A.; Maillard, P.; Garcia, M.; Durand, J. O., Mannose-targeted mesoporous silica nanoparticles for photodynamic therapy. *Chemical Communications (Camb)* **2009,** (12), 1475-7.

143. Warther, D.; Jimenez, C. M.; Raehm, L.; Gérardin, C.; Durand, J.-O.; Morère, A.; El Cheikh, K.; Gallud, A.; Gary-Bobo, M.; Maynadier, M.; Garcia, M., Small sized mesoporous silica nanoparticles functionalized with mannose for retinoblastoma cell imaging. *RSC Advances* **2014,** *4* (70).

144. Gary-Bobo, M.; Mir, Y.; Rouxel, C.; Brevet, D.; Basile, I.; Maynadier, M.; Vaillant, O.; Mongin, O.; Blanchard-Desce, M.; Morere, A.; Garcia, M.; Durand, J. O.; Raehm, L., Mannose-functionalized mesoporous silica nanoparticles for efficient two-photon photodynamic therapy of solid tumors. *Angewandte Chemie (International ed. in English)* **2011,** *50* (48), 11425-9.

145. Wu, C.; Xu, Q.; Chen, X.; Liu, J., Delivery luteolin with folacin-modified nanoparticle for glioma therapy. *International Journal of Nanomedicine* **2019,** *14*, 7515-7531.

146. Kim, J.; Dey, A.; Malhotra, A.; Liu, J.; Ahn, S. I.; Sei, Y. J.; Kenney, A. M.; MacDonald, T. J.; Kim, Y., Engineered biomimetic nanoparticle for dual targeting of the cancer stem-like cell population in sonic hedgehog medulloblastoma. *Proceedings of the National Academy of Sciences* **2020,** *117* (39), 24205.

147. Katchinskiy, N.; Godbout, R.; Hatef, A.; Elezzabi, A. Y., Anti-EpCAM Gold Nanorods and Femtosecond Laser Pulses for Targeted Lysis of Retinoblastoma. *Advanced Therapeutics* **2018,** *1* (1), 1800009.

148. Venditto, V. J.; Szoka, F. C., Cancer nanomedicines: So many papers and so few drugs! *Advanced Drug Delivery Reviews* **2013,** *65* (1), 80-88.

149. Harries, M.; Smith, I., The development and clinical use of trastuzumab (Herceptin). *Endocrine-related Cancer* **2002,** *9* (2), 75-85.

150. Jen, E. Y.; Ko, C.-W.; Lee, J. E.; Del Valle, P. L.; Aydanian, A.; Jewell, C.; Norsworthy, K. J.; Przepiorka, D.; Nie, L.; Liu, J.; Sheth, C. M.; Shapiro, M.; Farrell, A. T.; Pazdur, R., FDA Approval: Gemtuzumab Ozogamicin for the Treatment of Adults with Newly Diagnosed CD33-Positive Acute Myeloid Leukemia. *Clinical Cancer Research* **2018,** *24* (14), 3242.

151. Stewart, E.; McEvoy, J.; Wang, H.; Chen, X.; Honnell, V.; Ocarz, M.; Gordon, B.; Dapper, J.; Blankenship, K.; Yang, Y.; Li, Y.; Shaw, T. I.; Cho, J.-H.; Wang, X.; Xu, B.; Gupta, P.; Fan, Y.; Liu, Y.; Rusch, M.; Griffiths, L.; Jeon, J.; Freeman, B. B.; Clay, M. R.; Pappo, A.; Easton, J.; Shurtleff, S.; Shelat, A.; Zhou, X.; Boggs, K.; Mulder, H.; Yergeau, D.; Bahrami, A.; Mardis, E. R.; Wilson, R. K.; Zhang, J.; Peng, J.; Downing, J. R.; Dyer, M. A., Identification of Therapeutic Targets in Rhabdomyosarcoma through Integrated Genomic, Epigenomic, and Proteomic Analyses. *Cancer Cell* **2018,** *34* (3), 411-426.e19.

152. Scherzinger-Laude, K.; Schönherr, C.; Lewrick, F.; Süss, R.; Francese, G.; Rössler, J., Treatment of neuroblastoma and rhabdomyosarcoma using RGD-modified liposomal formulations of patupilone (EPO906). *International Journal of Nanomedicine* **2013,** *8*, 2197-211.

153. Gattenlöehner, S.; Vincent, A.; Leuschner, I.; Tzartos, S.; Müller-Hermelink, H. K.; Kirchner, T.; Marx, A., The fetal form of the acetylcholine receptor distinguishes rhabdomyosarcomas from other childhood tumors. *Am J Pathol* **1998,** *152* (2), 437-444.

154. Gattenlöehner, S.; Dockhorn-Dworniczak, B.; Leuschner, I.; Vincent, A.; Müller-Hermelink, H. K.; Marx, A., A comparison of MyoD1 and fetal acetylcholine receptor expression in childhood tumors and normal tissues: implications for the molecular diagnosis of minimal disease in rhabdomyosarcomas. *The Journal of Molecular Diagnostics* **1999,** *1* (1), 23-31.

155. Gattenlöhner, S.; Marx, A.; Markfort, B.; Pscherer, S.; Landmeier, S.; Juergens, H.; Müller-Hermelink, H.-K.; Matthews, I.; Beeson, D.; Vincent, A.; Rossig, C., Rhabdomyosarcoma Lysis by T Cells Expressing a Human Autoantibody-Based Chimeric Receptor Targeting the Fetal Acetylcholine Receptor. *Cancer research* **2006,** *66* (1), 24.

156. Teichert, R. W.; Rivier, J.; Torres, J.; Dykert, J.; Miller, C.; Olivera, B. M., A uniquely selective inhibitor of the mammalian fetal neuromuscular nicotinic acetylcholine receptor. *The Journal of Neuroscience* **2005,** *25* (3), 732-6.

157. Sahagian, G. G.; Steer, C. J., Transmembrane orientation of the mannose 6-phosphate receptor in isolated clathrin-coated vesicles. *The Journal of biological chemistry* **1985,** *260* (17), 9838-42.

158. Kornfeld, S.; Mellman, I., The biogenesis of lysosomes. *Annual review of cell biology* **1989,** *5*, 483-525.

159. Ghosh, P.; Dahms, N. M.; Kornfeld, S., Mannose 6-phosphate receptors: new twists in the tale. *Nature Reviews Molecular Cell Biology* **2003,** *4* (3), 202-213.

160. Bohnsack, R. N.; Song, X.; Olson, L. J.; Kudo, M.; Gotschall, R. R.; Canfield, W. M.; Cummings, R. D.; Smith, D. F.; Dahms, N. M., Cation-independent mannose 6-phosphate receptor: a composite of distinct phosphomannosyl binding sites. *The Journal of biological chemistry* **2009,** *284* (50), 35215-35226.

161. Dalle Vedove, E.; Costabile, G.; Merkel, O. M., Mannose and Mannose-6-Phosphate Receptor-Targeted Drug Delivery Systems and Their Application in Cancer Therapy. *Advanced healthcare materials* **2018,** *7* (14), e1701398-e1701398.

162. Berthe, M. L.; Esslimani Sahla, M.; Roger, P.; Gleizes, M.; Lemamy, G. J.; Brouillet, J. P.; Rochefort, H., Mannose-6-phosphate/insulin-like growth factor-II receptor expression levels during the progression from normal human mammary tissue to invasive breast carcinomas. *European Journal of Cancer* **2003,** *39* (5), 635-642.

163. Hébert, E.; Herbelin, C.; Bougnoux, P., Analysis of the IGF-II receptor gene copy number in breast carcinoma. *British Journal of Cancer* **1994,** *69* (1), 120-124.

164. Pavesi, L.; Fauchet, P. M., *Advanced Photodynamic Therapy*. Berlin, Heidelberg: Springer Berlin Heidelberg: Berlin, Heidelberg, 2008; p 315-334.

165. v. Tappeiner, H., Die photodynamische Erscheinung (Sensibilisierung durch fluoreszierende Stoffe). *Ergebnisse der Physiologie* **1909,** *8* (1), 698-741.

166. Von Tappeiner, H., Therapeutische Versuche mit fluoreszierenden Stoffen. *Munch Med Wochenschr* **1903,** *1*, 2042-2044.

167. Grossweiner, L. I.; Grossweiner, J. B.; Gerald Rogers, B. H., *Photodynamic Therapy: Science and Technology*. Dordrecht: Springer Netherlands: Dordrecht, 2005; p 243-273.

168. Dougherty, T. J., A Brief History of Clinical Photodynamic Therapy Development at Roswell Park Cancer Institute. *Journal of Clinical Laser Medicine & Surgery* **1996,** *14* (5), 219-221.

169. Daniell, M. D.; Hill, J. S., A HISTORY OF PHOTODYNAMIC THERAPY. *Australian and New Zealand Journal of Surgery* **1991,** *61* (5), 340-348.

170. Kuo, W.-S.; Shao, Y.-T.; Huang, K.-S.; Chou, T.-M.; Yang, C.-H., Antimicrobial Amino-Functionalized Nitrogen-Doped Graphene Quantum Dots for Eliminating Multidrug-Resistant Species in Dual-Modality Photodynamic Therapy and Bioimaging under Two-Photon Excitation. *ACS Applied Materials & Interfaces* **2018,** *10* (17), 14438-14446.

171. Gold, M. H., Acne and PDT: new techniques with lasers and light sources. *Lasers in Medical Science* **2007,** *22* (2), 67-72.

172. Wang, J.; Zheng, M.; Xie, Z., Carrier-free core–shell nanodrugs for synergistic two-photon photodynamic therapy of cervical cancer. *Journal of Colloid and Interface Science* **2019,** *535*, 84-91.

173. Gary-Bobo, M.; Mir, Y.; Rouxel, C.; Brevet, D.; Hocine, O.; Maynadier, M.; Gallud, A.; Da Silva, A.; Mongin, O.; Blanchard-Desce, M.; Richeter, S.; Loock, B.; Maillard, P.; Morere, A.; Garcia, M.; Raehm, L.; Durand, J. O., Multifunctionalized mesoporous silica nanoparticles for the in vitro treatment of retinoblastoma: Drug delivery, one and two-photon photodynamic therapy. *International Journal of Pharmaceutics* **2012,** *432* (1-2), 99-104.

174. Bressler, N. M. e. a., Photodynamic Therapy of Subfoveal Choroidal Neovascularization in Age-Related Macular Degeneration With Verteporfin: Two-Year Results of 2 Randomized Clinical Trials—TAP Report 2. *Archives of Ophthalmology* **2001,** *119* (2), 198-207.

175. Tschen, E.; Wong, D.; Pariser, D.; Dunlap, F.; Houlihan, A.; Ferdon, M.; Group, P. I. A. P. A. K. S., Photodynamic therapy using aminolaevulinic acid for patients with nonhyperkeratotic actinic keratoses of the face and scalp: phase IV multicentre clinical trial with 12-month follow up. *British Journal of Dermatology* **2006,** *155* (6), 1262-1269.

176. Smits, T.; Kleinpenning, M. M.; Van Erp, P. E. J.; Van De Kerkhof, P. C. M.; Gerritsen, M.-J. P., A placebo-controlled randomized study on the clinical effectiveness, immunohistochemical changes and protoporphyrin IX accumulation in fractionated 5-aminolaevulinic acid-photodynamic therapy in patients with psoriasis. *British Journal of Dermatology* **2006,** *155* (2), 429-436.

177. Bolze, F.; Jenni, S.; Sour, A.; Heitz, V., Molecular photosensitisers for two-photon photodynamic therapy. *Chemical Communications (Camb)* **2017,** *53* (96), 12857-12877.

178. Croissant, J. G.; Zink, J. I.; Raehm, L.; Durand, J.-O., Two-Photon-Excited Silica and Organosilica Nanoparticles for Spatiotemporal Cancer Treatment. *Advanced Healthcare Materials* **2018,** *7* (7), 1701248.

179. Wang, S.; Wu, W.; Manghnani, P.; Xu, S.; Wang, Y.; Goh, C. C.; Ng, L. G.; Liu, B., Polymerization-Enhanced Two-Photon Photosensitization for Precise Photodynamic Therapy. *ACS Nano* **2019,** *13* (3), 3095-3105.

180. Zheng, Z.; Liu, H.; Zhai, S.; Zhang, H.; Shan, G.; Kwok, R. T. K.; Ma, C.; Sung, H. H. Y.; Williams, I. D.; Lam, J. W. Y.; Wong, K. S.; Hu, X.; Tang, B. Z., Highly efficient singlet oxygen generation, two-photon photodynamic therapy and melanoma ablation by rationally designed mitochondria-specific near-infrared AIEgens. *Chemical Science* **2020,** *11* (9), 2494-2503.

181. de Freitas, L. F.; Hamblin, M. R., Chapter 1 - Antimicrobial photoinactivation with functionalized fullerenes. In *Nanobiomaterials in Antimicrobial Therapy*, Grumezescu, A. M., Ed. William Andrew Publishing: 2016; pp 1-27.

182. Felsher, D. W., Cancer revoked: oncogenes as therapeutic targets. *Nature Reviews Cancer* **2003,** *3* (5), 375-80.

183. Henderson, B. W.; Dougherty, T. J., HOW DOES PHOTODYNAMIC THERAPY WORK? *Photochemistry and Photobiology* **1992,** *55* (1), 145-157.

184. Dougherty, T. J.; Gomer, C. J.; Henderson, B. W.; Jori, G.; Kessel, D.; Korbelik, M.; Moan, J.; Peng, Q., Photodynamic Therapy. *JNCI: Journal of the National Cancer Institute* **1998,** *90* (12), 889-905.

185. Shen, Y.; Shuhendler, A. J.; Ye, D.; Xu, J. J.; Chen, H. Y., Two-photon excitation nanoparticles for photodynamic therapy. *Chemical Society Reviews* **2016,** *45* (24), 6725-6741.

186. Wilson, B. C.; Patterson, M. S., The physics, biophysics and technology of photodynamic therapy. *Physics in Medicine and Biology* **2008,** *53* (9), R61-109.

187. Master, A.; Livingston, M.; Sen Gupta, A., Photodynamic nanomedicine in the treatment of solid tumors: Perspectives and challenges. *Journal of Controlled Release* **2013,** *168* (1), 88-102.

188. dos Santos, A. F.; de Almeida, D. R. Q.; Terra, L. F.; Baptista, M. S.; Labriola, L., Photodynamic therapy in cancer treatment - an update review. *Journal of Cancer Metastasis and Treatment* **2019,** *5*, 25.

189. Fakhar-e-Alam, M.; Aseer, M.; Rana, M. S.; Hammad Aziz, M.; Atif, M.; Yaqub, N.; Farooq, W. A., Spectroscopic features of PHOTOGEM® in human Rhabdomyosarcoma (RD) cellular model. *Journal of King Saud University - Science* **2020,** *32* (7), 3131-3137.

190. Ocker, L.; Adamus, A.; Hempfling, L.; Wagner, B.; Vahdad, R.; Verburg, F. A.; Luster, M.; Schurrat, T.; Bier, D.; Frank, M.; Lisec, J.; Engel, N.; Seitz, G., Hypericin and its radio iodinated derivatives – A novel combined approach for the treatment of pediatric alveolar rhabdomyosarcoma cells in vitro. *Photodiagnosis and Photodynamic Therapy* **2020,** *29*, 101588.

191. Atif, M.; Malik, A. R.; Fakhar-e-Alam, M.; Hayat, S. S.; Zaidi, S. S. Z.; Suleman, R.; Ikram, M., In vitro studies of Photofrin® mediated photodynamic therapy on human rhabdomyosarcoma cell line (RD). *Laser Physics* **2012,** *22* (1), 286-293.

192. Longevial, J.-F.; Yamaji, A.; Aggad, D.; Kim, G.; Chia, W. X.; Nishimura, T.; Miyake, Y.; Clément, S.; Oh, J.; Daurat, M.; Nguyen, C.; Kim, D.; Gary-Bobo, M.; Richeter, S.; Shinokubo, H., Diazachlorin and diazabacteriochlorin for one- and two-photon photodynamic therapy. *Chemical Communications* **2018,** *54* (98), 13829-13832.

193. Li, L.; Fourkas, J. T., Multiphoton polymerization. *Materials Today* **2007,** *10* (6), 30-37.

194. Garofalakis, A.; Kruglik, S.; Mansuryan, T.; Gillibert, A.; Thiberville, L.; Louradour, F.; Vever-Bizet, C.; Bourg-Heckly, G., Characterization of a multicore fiber image guide for nonlinear endoscopic imaging using two-photon fluorescence and second-harmonic generation. *Journal of Biomedical Optics* **2019,** *24* (10), 106004.

195. Mhashilkar, A.; Chada, S.; Roth, J. A.; Ramesh, R., Gene therapy. Therapeutic approaches and implications. *Biotechnology advances* **2001,** *19* (4), 279-97.

196. Wirth, T.; Parker, N.; Ylä-Herttuala, S., History of gene therapy. *Gene* **2013,** *525* (2), 162-169.

197. Rosenberg, S. A.; Aebersold, P.; Cornetta, K.; Kasid, A.; Morgan, R. A.; Moen, R.; Karson, E. M.; Lotze, M. T.; Yang, J. C.; Topalian, S. L.; Merino, M. J.; Culver, K.; Miller, A. D.; Blaese, R. M.; Anderson, W. F., Gene Transfer into Humans — Immunotherapy of Patients with Advanced Melanoma, Using Tumor-Infiltrating Lymphocytes Modified by Retroviral Gene Transduction. *New England Journal of Medicine* **1990,** *323* (9), 570-578.

198. Blaese, R. M.; Culver, K. W.; Miller, A. D.; Carter, C. S.; Fleisher, T.; Clerici, M.; Shearer, G.; Chang, L.; Chiang, Y.; Tolstoshev, P.; Greenblatt, J. J.; Rosenberg, S. A.; Klein, H.; Berger, M.; Mullen, C. A.; Ramsey, W. J.; Muul, L.; Morgan, R. A.; Anderson, W. F., T lymphocyte-directed gene therapy for ADA- SCID: initial trial results after 4 years. *Science* **1995,** *270* (5235), 475-80.

199. Raul, O.; Consolacion, M.; Jose, P.; Pablo, J. A.; Octavio, C.; Fernando, R.-S.; Fidel, H.; Antonia, A., New Gene Therapy Strategies for Cancer Treatment: A Review of Recent Patents. *Recent Patents on Anti-Cancer Drug Discovery* **2012,** *7* (3), 297-312.

200. Escors, D.; Breckpot, K., Lentiviral vectors in gene therapy: their current status and future potential. *Archivum immunologiae et therapiae experimentalis* **2010,** *58* (2), 107-19.

201. Mulligan, R. C., The basic science of gene therapy. *Science* **1993,** *260* (5110), 926-32.

202. Mountain, A., Gene therapy: the first decade. *Trends in Biotechnology* **2000,** *18* (3), 119-128.

203. Dizaj, S. M.; Jafari, S.; Khosroushahi, A. Y., A sight on the current nanoparticle-based gene delivery vectors. *Nanoscale research letters* **2014,** *9* (1), 252.

204. Rengaswamy, V.; Zimmer, D.; Süss, R.; Rössler, J., RGD liposome-protamine-siRNA (LPR) nanoparticles targeting PAX3-FOXO1 for alveolar rhabdomyosarcoma therapy. *Journal of Controlled Release* **2016,** *235*, 319-327.

205. Schiffelers, R. M.; Ansari, A.; Xu, J.; Zhou, Q.; Tang, Q.; Storm, G.; Molema, G.; Lu, P. Y.; Scaria, P. V.; Woodle, M. C. Cancer siRNA therapy by tumor selective delivery with ligand-targeted sterically stabilized nanoparticle *Nucleic Acids Res* [Online], 2004, p. e149. PubMed. (accessed 2004/11//).

206. Toub, N.; Bertrand, J.-R.; Tamaddon, A.; Elhamess, H.; Hillaireau, H.; Maksimenko, A.; Maccario, J.; Malvy, C.; Fattal, E.; Couvreur, P., Efficacy of siRNA Nanocapsules Targeted Against the EWS–Fli1 Oncogene in Ewing Sarcoma. *Pharmaceutical Research* **2006,** *23* (5), 892-900.

207. Di Paolo, D.; Brignole, C.; Pastorino, F.; Carosio, R.; Zorzoli, A.; Rossi, M.; Loi, M.; Pagnan, G.; Emionite, L.; Cilli, M.; Bruno, S.; Chiarle, R.; Allen, T. M.; Ponzoni, M.; Perri, P., Neuroblastoma-targeted nanoparticles entrapping siRNA specifically knockdown ALK. *Molecular Therapy* **2011,** *19* (6), 1131-1140.

208. Roveri, M.; Pfohl, A.; Jaaks, P.; Alijaj, N.; Leroux, J.-C.; Luciani, P.; Bernasconi, M., Prolonged circulation and increased tumor accumulation of liposomal vincristine in a mouse model of rhabdomyosarcoma. *Nanomedicine* **2017,** *12* (10), 1135-1151.

209. Krukemeyer, M. G.; Krenn, V.; Jakobs, M.; Wagner, W., Magnetic drug targeting in a rhabdomyosarcoma rat model using magnetite-dextran composite nanoparticle-bound mitoxantrone and 0.6 tesla extracorporeal magnets− sarcoma treatment in progress. *Journal of drug targeting* **2012,** *20* (2), 185-193.

210. Wang, S.-L.; Yao, H.-H.; Guo, L.-L.; Dong, L.; Li, S.-G.; Gu, Y.-P.; Qin, Z.-H., Selection of optimal sites for TGFB1 gene silencing by chitosan–TPP nanoparticle-mediated delivery of shRNA. *Cancer genetics and cytogenetics* **2009,** *190* (1), 8-14.

211. Huang, X.; Townley, H., Knock-down of ELMO1 in Paediatric Rhabdomyosarcoma Cells by Nanoparticle Mediated siRNA Delivery. *Nanobiomedicine* **2016,** *3*, 4.

212. Taha, A. A.; AL-Jawad, S. M.; AL-Barram, L. F., Improvement of cancer therapy by TAT peptide conjugated gold nanoparticles. *Journal of Cluster Science* **2019,** *30* (2), 403-414.

213. Biswas, S.; Ahn, H.-Y.; Bondar, M. V.; Belfield, K. D., Two-photon absorption enhancement of polymer-templated porphyrin-based J-aggregates. *Langmuir* **2012,** *28* (2), 1515-1522.

214. Starkey, J. R.; Rebane, A. K.; Drobizhev, M. A.; Meng, F.; Gong, A.; Elliott, A.; McInnerney, K.; Spangler, C. W., New two-photon activated photodynamic therapy sensitizers induce xenograft tumor regressions after near-IR laser treatment through the body of the host mouse. *Clinical Cancer Research* **2008,** *14* (20), 6564-6573.

215. Fathalla, M.; Li, S.-C.; Diebold, U.; Alb, A.; Jayawickramarajah, J., Water-soluble nanorods self-assembled via pristine C60 and porphyrin moieties. *Chemical Communications* **2009,** (28), 4209-4211.

216. Lin, P. H.; Selinfreund, R.; Wakshull, E.; Wharton, W., Rapid and efficient purification of plasma membrane from cultured cells: characterization of epidermal growth factor binding. *Biochemistry* **1987,** *26* (3), 731-736.

217. Braga-Lagache, S.; Buchs, N.; Iacovache, M.-I.; Zuber, B.; Jackson, C. B.; Heller, M., Robust label-free, quantitative profiling of circulating plasma microparticle (MP) associated proteins. *Molecular & cellular proteomics* **2016,** *15* (12), 3640-3652.

218. Cox, J.; Hein, M. Y.; Luber, C. A.; Paron, I.; Nagaraj, N.; Mann, M., Accurate proteome-wide label-free quantification by delayed normalization and maximal peptide ratio extraction, termed MaxLFQ. *Molecular & cellular proteomics* **2014,** *13* (9), 2513-2526.

219. Ahrné, E.; Molzahn, L.; Glatter, T.; Schmidt, A., Critical assessment of proteome-wide label-free absolute abundance estimation strategies. *Proteomics* **2013,** *13* (17), 2567-2578.

220. Tyanova, S.; Temu, T.; Cox, J., The MaxQuant computational platform for mass spectrometry-based shotgun proteomics. *Nature protocols* **2016,** *11* (12), 2301.

221. Lazar, C.; Gatto, L.; Ferro, M.; Bruley, C.; Burger, T., Accounting for the multiple natures of missing values in label-free quantitative proteomics data sets to compare imputation strategies. *Journal of proteome research* **2016,** *15* (4), 1116-1125.

222. Distler, J. J.; Guo, J. F.; Jourdian, G. W.; Srivastava, O. P.; Hindsgaul, O., The binding specificity of high and low molecular weight phosphomannosyl receptors from bovine testes. Inhibition studies with chemically synthesized 6-O-phosphorylated oligomannosides. *Journal of Biological Chemistry* **1991,** *266* (32), 21687-21692.

223. Redberry, G. W., *Gene silencing: new research*. Nova Publishers: 2006.

224. Leuschner, P. J. F.; Ameres, S. L.; Kueng, S.; Martinez, J., Cleavage of the siRNA passenger strand during RISC assembly in human cells. *EMBO Rep* **2006,** *7* (3), 314-320.

225. Wilson, R. C.; Doudna, J. A., Molecular Mechanisms of RNA Interference. *Annual Review of Biophysics* **2013,** *42* (1), 217-239.

226. Fire, A.; Xu, S.; Montgomery, M. K.; Kostas, S. A.; Driver, S. E.; Mello, C. C., Potent and specific genetic interference by double-stranded RNA in Caenorhabditis elegans. *Nature* **1998,** *391* (6669), 806-11.

227. Elbashir, S. M.; Harborth, J.; Lendeckel, W.; Yalcin, A.; Weber, K.; Tuschl, T., Duplexes of 21-nucleotide RNAs mediate RNA interference in cultured mammalian cells. *Nature* **2001,** *411* (6836), 494-498.

228. Kim, B.; Park, J. H.; Sailor, M. J., Rekindling RNAi Therapy: Materials Design Requirements for In Vivo siRNA Delivery. *Advanced Materials* **2019,** *31* (49), e1903637.

229. Lin, G.; Li, L.; Panwar, N.; Wang, J.; Tjin, S. C.; Wang, X.; Yong, K.-T., Non-viral gene therapy using multifunctional nanoparticles: Status, challenges, and opportunities. *Coordination Chemistry Reviews* **2018,** *374*, 133-152.

230. Wojnilowicz, M.; Glab, A.; Bertucci, A.; Caruso, F.; Cavalieri, F., Super-resolution Imaging of Proton Sponge-Triggered Rupture of Endosomes and Cytosolic Release of Small Interfering RNA. *ACS Nano* **2019,** *13* (1), 187-202.

231. Hoffmann, M.; Hersch, N.; Merkel, R.; Csiszar, A.; Hoffmann, B., Changing the way of entrance: Highly efficient transfer of mRNA and siRNA via fusogenic nano-carriers. *Journal of biomedical nanotechnology* **2019,** *15* (1), 170-183.

232. Bøe, S. L.; Hovig, E., Enhancing nucleic acid delivery by photochemical internalization. *Therapeutic delivery* **2013,** *4* (9), 1125-1140.

233. Berg, K.; Weyergang, A.; Prasmickaite, L.; Bonsted, A.; Høgset, A.; Strand, M. T.; Wagner, E.; Selbo, P. K., Photochemical internalization (PCI): a technology for drug delivery. *Methods in Molecular Biology* **2010,** *635*, 133-45.

234. Berg, K.; Folini, M.; Prasmickaite, L.; Selbo, P. K.; Bonsted, A.; Engesaeter, B.; Zaffaroni, N.; Weyergang, A.; Dietze, A.; Maelandsmo, G. M.; Wagner, E.; Norum, O. J.;

Høgset, A., Photochemical internalization: a new tool for drug delivery. *Current pharmaceutical biotechnology* **2007,** *8* (6), 362-72.

235. Hartono, S. B.; Gu, W.; Kleitz, F.; Liu, J.; He, L.; Middelberg, A. P. J.; Yu, C.; Lu, G. Q.; Qiao, S. Z., Poly-l-lysine Functionalized Large Pore Cubic Mesostructured Silica Nanoparticles as Biocompatible Carriers for Gene Delivery. *ACS Nano* **2012,** *6* (3), 2104-2117.

236. Ekineker, G.; Nguyen, C.; Bayir, S.; Dominguez Gil, S.; Isci, U.; Daurat, M.; Godefroy, A.; Raehm, L.; Charnay, C.; Oliviero, E.; Ahsen, V.; Gary-Bobo, M.; Durand, J. O.; Dumoulin, F., Phthalocyanine-based mesoporous organosilica nanoparticles: NIR photodynamic efficiency and siRNA photochemical internalization. *Chemical Communications (Camb)* **2019,** *55* (77), 11619-11622.

237. Salekdeh, P. R.; Ma'mani, L.; Tavakkoly-Bazzaz, J.; Mousavi, H.; Modarressi, M. H.; Salekdeh, G. H., Bi-functionalized aminoguanidine-PEGylated periodic mesoporous organosilica nanoparticles: a promising nanocarrier for delivery of Cas9-sgRNA ribonucleoproteine. *Journal of Nanobiotechnology* **2021,** *19* (1), 95.

238. Choo, J. R.; Nielsen, T. O., Biomarkers for Basal-like Breast Cancer. *Cancers* **2010,** *2* (2), 1040-1065.

239. Liu, W.; Chaix, A.; Gary-Bobo, M.; Angeletti, B.; Masion, A.; Da Silva, A.; Daurat, M.; Lichon, L.; Garcia, M.; Morère, A.; El Cheikh, K.; Durand, J.-O.; Cunin, F.; Auffan, M., Stealth Biocompatible Si-Based Nanoparticles for Biomedical Applications. *Nanomaterials (Basel)* **2017,** *7* (10), 288.

240. Yohe, M. E.; Heske, C. M.; Stewart, E.; Adamson, P. C.; Ahmed, N.; Antonescu, C. R.; Chen, E.; Collins, N.; Ehrlich, A.; Galindo, R. L.; Gryder, B. E.; Hahn, H.; Hammond, S.; Hatley, M. E.; Hawkins, D. S.; Hayes, M. N.; Hayes-Jordan, A.; Helman, L. J.; Hettmer, S.; Ignatius, M. S.; Keller, C.; Khan, J.; Kirsch, D. G.; Linardic, C. M.; Lupo, P. J.; Rota, R.; Shern, J. F.; Shipley, J.; Sindiri, S.; Tapscott, S. J.; Vakoc, C. R.; Wexler, L. H.; Langenau, D. M., Insights into pediatric rhabdomyosarcoma research: Challenges and goals. *Pediatric Blood & Cancer* **2019,** *66* (10), e27869.

241. Dagher, R.; Helman, L., Rhabdomyosarcoma: an overview. *The oncologist* **1999,** *4* (1), 34-44.

242. Bisogno, G.; Ferrari, A.; Bergeron, C.; Scagnellato, A.; Prete, A.; Alaggio, R.; Casanova, M.; D'Angelo, P.; Di Cataldo, A.; Carli, M., The IVADo regimen—A pilot study with ifosfamide, vincristine, actinomycin D, and doxorubicin in children with metastatic soft tissue sarcoma. *Cancer* **2005,** *103* (8), 1719-1724.

243. Loi, M.; Di Paolo, D.; Soster, M.; Brignole, C.; Bartolini, A.; Emionite, L.; Sun, J.; Becherini, P.; Curnis, F.; Petretto, A.; Sani, M.; Gori, A.; Milanese, M.; Gambini, C.; Longhi, R.; Cilli, M.; Allen, T. M.; Bussolino, F.; Arap, W.; Pasqualini, R.; Corti, A.; Ponzoni, M.; Marchiò, S.; Pastorino, F., Novel phage display-derived neuroblastoma-targeting peptides potentiate the effect of drug nanocarriers in preclinical settings. *Journal of Controlled Release* **2013,** *170* (2), 233-41.

244. Pastorino, F.; Brignole, C.; Marimpietri, D.; Sapra, P.; Moase, E. H.; Allen, T. M.; Ponzoni, M., Doxorubicin-loaded Fab' fragments of anti-disialoganglioside immunoliposomes selectively inhibit the growth and dissemination of human neuroblastoma in nude mice. *Cancer research* **2003,** *63* (1), 86-92.

245. Taylor, J. G. t.; Cheuk, A. T.; Tsang, P. S.; Chung, J. Y.; Song, Y. K.; Desai, K.; Yu, Y.; Chen, Q. R.; Shah, K.; Youngblood, V.; Fang, J.; Kim, S. Y.; Yeung, C.; Helman, L. J.; Mendoza, A.; Ngo, V.; Staudt, L. M.; Wei, J. S.; Khanna, C.; Catchpoole, D.; Qualman, S. J.; Hewitt, S. M.; Merlino, G.; Chanock, S. J.; Khan, J., Identification of FGFR4-activating mutations in human rhabdomyosarcomas that promote metastasis in xenotransplanted models. *Journal of Clinical Investigation* **2009,** *119* (11), 3395-407.

246. Wang, L.; Reipa, V.; Blasic, J., Silicon Nanoparticles as a Luminescent Label to DNA. *Bioconjugate Chemistry* **2004,** *15* (2), 409-412.

247. Li, Z.; Ruckenstein, E., Water-Soluble Poly(acrylic acid) Grafted Luminescent Silicon Nanoparticles and Their Use as Fluorescent Biological Staining Labels. *Nano Letters* **2004,** *4*, 1463-1467.

248. Anderson, S. H. C.; Elliott, H.; Wallis, D. J.; Canham, L. T.; Powell, J. J., Dissolution of different forms of partially porous silicon wafers under simulated physiological conditions. *physica status solidi (a)* **2003,** *197* (2), 331-335.

249. Zhang, X. G., Morphology and Formation Mechanisms of Porous Silicon. *Journal of The Electrochemical Society* **2004,** *151* (1), C69.

250. Ollivier, N.; Desmet, R.; Drobecq, H.; Blanpain, A.; Boll, E.; Leclercq, B.; Mougel, A.; Vicogne, J.; Melnyk, O., A simple and traceless solid phase method simplifies the assembly of large peptides and the access to challenging proteins. *Chemical Science* **2017,** *8* (8), 5362-5370.

251. Boll, E.; Ebran, J.-P.; Drobecq, H.; El-Mahdi, O.; Raibaut, L.; Ollivier, N.; Melnyk, O., Access to Large Cyclic Peptides by a One-Pot Two-Peptide Segment Ligation/Cyclization Process. *Organic Letters* **2015,** *17* (1), 130-133.

252. J.M. Sutton, O. J. C., N. Fernandez, R.W. Boyle, Porphyrin, Chlorin, and Bacteriochlorin Isothiocyanates: Useful Reagents for the Synthesis of Photoactive Bioconjugates *Bioconjugate Chemistry* **2002,** *13* (2), 249-263.

253. Teichert, R. W.; López-Vera, E.; Gulyas, J.; Watkins, M.; Rivier, J.; Olivera, B. M., Definition and Characterization of the Short αA-Conotoxins: A Single Residue Determines Dissociation Kinetics from the Fetal Muscle Nicotinic Acetylcholine Receptor. *Biochemistry* **2006,** *45* (4), 1304-13012.

254. Robertson, C. A.; Evans, D. H.; Abrahamse, H., Photodynamic therapy (PDT): a short review on cellular mechanisms and cancer research applications for PDT. *Journal of photochemistry and photobiology. B* **2009,** *96* (1), 1-8.

255. Lucky, S. S.; Soo, K. C.; Zhang, Y., Nanoparticles in Photodynamic Therapy. *Chemical Reviews* **2015,** *115* (4), 1990-2042.

256. Derfus, A. M.; Chan, W. C. W.; Bhatia, S. N., Probing the Cytotoxicity of Semiconductor Quantum Dots. *Nano Letters* **2004,** *4* (1), 11-18.

257. Fang, M.; Peng, C.-W.; Pang, D.-W.; Li, Y., Quantum dots for cancer research: current status, remaining issues, and future perspectives. *Cancer Biol Med* **2012,** *9* (3), 151-163.

258. Soenen, S. J.; Rivera-Gil, P.; Montenegro, J.-M.; Parak, W. J.; De Smedt, S. C.; Braeckmans, K., Cellular toxicity of inorganic nanoparticles: Common aspects and guidelines for improved nanotoxicity evaluation. *Nano Today* **2011,** *6* (5), 446-465.

259. Ehlerding, E. B.; Chen, F.; Cai, W., Biodegradable and Renal Clearable Inorganic Nanoparticles. *Advanced Science* **2016,** *3* (2), 1500223.

260. Cheng, L.; Anglin, E.; Cunin, F.; Kim, D.; Sailor, M. J.; Falkenstein, I.; Tammewar, A.; Freeman, W. R., Intravitreal properties of porous silicon photonic crystals: a potential self-reporting intraocular drug-delivery vehicle. *British Journal of Ophthalmology* **2008,** *92* (5), 705-711.

261. Xiao, L.; Gu, L.; Howell, S. B.; Sailor, M. J., Porous silicon nanoparticle photosensitizers for singlet oxygen and their phototoxicity against cancer cells. *ACS Nano* **2011,** *5* (5), 3651-9.

262. Secret, E.; Maynadier, M.; Gallud, A.; Chaix, A.; Bouffard, E.; Gary-Bobo, M.; Marcotte, N.; Mongin, O.; El Cheikh, K.; Hugues, V.; Auffan, M.; Frochot, C.; Morère, A.; Maillard, P.; Blanchard-Desce, M.; Sailor, M. J.; Garcia, M.; Durand, J.-O.; Cunin, F., Two-Photon Excitation of Porphyrin-Functionalized Porous Silicon Nanoparticles for Photodynamic Therapy. *Advanced Materials* **2014,** *26* (45), 7643-8.

263. Huang, S.; Kamihira, M., Development of hybrid viral vectors for gene therapy. *Biotechnology advances* **2013,** *31* (2), 208-223.

264. Foldvari, M.; Chen, D. W.; Nafissi, N.; Calderon, D.; Narsineni, L.; Rafiee, A., Non-viral gene therapy: Gains and challenges of non-invasive administration methods. *Journal of Controlled Release* **2016,** *240*, 165-190.

265. Garcia-Guerra, A.; Dunwell, T. L.; Trigueros, S., Nano-Scale Gene Delivery Systems: Current Technology, Obstacles, and Future Directions. *Current medicinal chemistry* **2018,** *25* (21), 2448-2464.

266. Na, H. K.; Kim, M. H.; Park, K.; Ryoo, S. R.; Lee, K. E.; Jeon, H.; Ryoo, R.; Hyeon, C.; Min, D. H., Efficient functional delivery of siRNA using mesoporous silica nanoparticles with ultralarge pores. *Small* **2012,** *8* (11), 1752-61.

267. Joo, J.; Kwon, E. J.; Kang, J.; Skalak, M.; Anglin, E. J.; Mann, A. P.; Ruoslahti, E.; Bhatia, S. N.; Sailor, M. J., Porous silicon-graphene oxide core-shell nanoparticles for targeted delivery of siRNA to the injured brain. *Nanoscale Horizons* **2016,** *1* (5), 407-414.

268. Mann, A. P.; Scodeller, P.; Hussain, S.; Joo, J.; Kwon, E.; Braun, G. B.; Mölder, T.; She, Z. G.; Kotamraju, V. R.; Ranscht, B.; Krajewski, S.; Teesalu, T.; Bhatia, S.; Sailor, M. J.;

Ruoslahti, E., A peptide for targeted, systemic delivery of imaging and therapeutic compounds into acute brain injuries. *Nature communications* **2016,** *7*, 11980.

269. Tong, W. Y.; Alnakhli, M.; Bhardwaj, R.; Apostolou, S.; Sinha, S.; Fraser, C.; Kuchel, T.; Kuss, B.; Voelcker, N. H., Delivery of siRNA in vitro and in vivo using PEI-capped porous silicon nanoparticles to silence MRP1 and inhibit proliferation in glioblastoma. *Journal of Nanobiotechnology* **2018,** *16* (1), 38.

270. Hasanzadeh Kafshgari, M.; Alnakhli, M.; Delalat, B.; Apostolou, S.; Harding, F. J.; Mäkilä, E.; Salonen, J. J.; Kuss, B. J.; Voelcker, N. H., Small interfering RNA delivery by polyethylenimine-functionalised porous silicon nanoparticles. *Biomaterials Science* **2015,** *3* (12), 1555-1565.

271. Laroui, N.; Coste, M.; Lichon, L.; Bessin, Y.; Gary-Bobo, M.; Pratviel, G.; Bonduelle, C.; Bettache, N.; Ulrich, S., Combination of photodynamic therapy and gene silencing achieved through the hierarchical self-assembly of porphyrin-siRNA complexes. *International Journal of Pharmaceutics (Amsterdam, Neth.)* **2019,** *569*, 118585.

272. Yu, L.; Liang, D.; Chen, C.; Tang, X., Caged siRNAs with Single cRGD Modification for Photoregulation of Exogenous and Endogenous Gene Expression in Cells and Mice. *Biomacromolecules* **2018,** *19* (7), 2526-2534.

273. Wang, J.; Xie, L.; Wang, T.; Wu, F.; Meng, J.; Liu, J.; Xu, H., Visible light-switched cytosol release of siRNA by amphiphilic fullerene derivative to enhance RNAi efficacy in vitro and in vivo. *Acta Biomaterialia* **2017,** *59*, 158-169.

274. Patil, S.; Moosa, B.; Alsaiari, S.; Alamoudi, K.; Alshamsan, A.; Almailk, A.; Adil, K.; Eddaoudi, M.; Khashab, N. M., Supramolecular Self-Assembly of Histidine-Capped-Dialkoxy-Anthracene: A Visible Light Triggered Platform for facile siRNA Delivery. *Chemistry: A European Journal* **2016,** *22* (39), 13789-13793.

275. Foster, A. A.; Greco, C. T.; Green, M. D.; Epps, T. H., 3rd; Sullivan, M. O., Light-mediated activation of siRNA Release in diblock copolymer assemblies for controlled gene silencing. *Advanced Healthcare Materials* **2015,** *4* (5), 760-70.

276. Buhr, F.; Kohl-Landgraf, J.; tom Dieck, S.; Hanus, C.; Chatterjee, D.; Hegelein, A.; Schuman, E. M.; Wachtveitl, J.; Schwalbe, H., Design of photocaged puromycin for nascent polypeptide release and spatiotemporal monitoring of translation. *Angewandte Chemie (International ed. in English)* **2015,** *54* (12), 3717-3721.

277. Zheng, J.; Nie, Y.; Yang, S.; Xiao, Y.; Li, J.; Li, Y.; Yang, R., Remote-controlled release of DNA in living cells via simultaneous light and host-guest mediations. *Analytical Chemistry* **2014,** *86* (20), 10208-14.

278. Li, H.-J.; Wang, H.-X.; Sun, C.-Y.; Du, J.-Z.; Wang, J., Shell-detachable nanoparticles based on a light-responsive amphiphile for enhanced siRNA delivery. *RSC Advances* **2014,** *4* (4), 1961-1964.

279. Green, M. D.; Foster, A. A.; Greco, C. T.; Roy, R.; Lehr, R. M.; Epps, I. I. I. T. H.; Sullivan, M. O., Catch and release: photocleavable cationic diblock copolymers as a potential platform for nucleic acid delivery. *Polymer Chemistry* **2014,** *5* (19), 5535-5541.

280. Yin, L.; Tang, H.; Kim, K. H.; Zheng, N.; Song, Z.; Gabrielson, N. P.; Lu, H.; Cheng, J., Light-responsive helical polypeptides capable of reducing toxicity and unpacking DNA: toward nonviral gene delivery. *Angewandte Chemie (International ed. in English)* **2013,** *52* (35), 9182-9186.

281. Li, Y.; Yang, J.; Sun, L.; Wang, W.; Liu, W., UV light-triggered unpacking of DNA to enhance gene transfection of azobenzene-containing polycations. *Journal of Materials Chemistry B* **2014,** *2* (24), 3868-3878.

282. Rudiuk, S.; Saito, H.; Hara, T.; Inoue, T.; Yoshikawa, K.; Baigl, D., Light-Regulated mRNA Condensation by a Photosensitive Surfactant Works as a Series Photoswitch of Translation Activity in the Presence of Small RNAs. *Biomacromolecules* **2011,** *12* (11), 3945-3951.

283. Estévez-Torres, A.; Crozatier, C.; Diguet, A.; Hara, T.; Saito, H.; Yoshikawa, K.; Baigl, D., Sequence-independent and reversible photocontrol of transcription/expression systems using a photosensitive nucleic acid binder. *Proc Natl Acad Sci U S A* **2009,** *106* (30), 12219-12223.

284. Li, J.; Leung, C. W. T.; Wong, D. S. H.; Xu, J.; Li, R.; Zhao, Y.; Yung, C. Y. Y.; Zhao, E.; Tang, B. Z.; Bian, L., Photocontrolled SiRNA Delivery and Biomarker-Triggered Luminogens of Aggregation-Induced Emission by Up-Conversion NaYF(4):Yb(3+)Tm(3+)@SiO(2) Nanoparticles for Inducing and Monitoring Stem-Cell Differentiation. *ACS Applied Materials & Interfaces* **2019,** *11* (25), 22074-22084.

285. Jayakumar, M. K. G.; Bansal, A.; Huang, K.; Yao, R.; Li, B. N.; Zhang, Y., Near-Infrared-Light-Based Nano-Platform Boosts Endosomal Escape and Controls Gene Knockdown in Vivo. *ACS Nano* **2014,** *8* (5), 4848-4858.

286. Yang, Y.; Liu, F.; Liu, X.; Xing, B., NIR light controlled photorelease of siRNA and its targeted intracellular delivery based on upconversion nanoparticles. *Nanoscale* **2013,** *5* (1), 231-238.

287. Jayakumar, M. K.; Idris, N. M.; Zhang, Y., Remote activation of biomolecules in deep tissues using near-infrared-to-UV upconversion nanotransducers. *Proc Natl Acad Sci U S A* **2012,** *109* (22), 8483-8.

288. Chen, G.; Ma, B.; Xie, R.; Wang, Y.; Dou, K.; Gong, S., NIR-induced spatiotemporally controlled gene silencing by upconversion nanoparticle-based siRNA nanocarrier. *Journal of Controlled Release* **2018,** *282*, 148-155.

289. Morgan, E.; Wupperfeld, D.; Morales, D.; Reich, N., Shape Matters: Gold Nanoparticle Shape Impacts the Biological Activity of siRNA Delivery. *Bioconjugate Chemistry* **2019,** *30* (3), 853-860.

290. Riley, R. S.; Dang, M. N.; Billingsley, M. M.; Abraham, B.; Gundlach, L.; Day, E. S., Evaluating the Mechanisms of Light-Triggered siRNA Release from Nanoshells for Temporal Control Over Gene Regulation. *Nano letters* **2018,** *18* (6), 3565-3570.

291. Yin, F.; Yang, C.; Wang, Q.; Zeng, S.; Hu, R.; Lin, G.; Tian, J.; Hu, S.; Lan, R. F.; Yoon, H. S.; Lu, F.; Wang, K.; Yong, K.-T., A Light-Driven Therapy of Pancreatic Adenocarcinoma Using Gold Nanorods-Based Nanocarriers for Co-Delivery of Doxorubicin and siRNA. *Theranostics* **2015,** *5* (8), 818-833.

292. Huang, X.; Hu, Q.; Braun, G. B.; Pallaoro, A.; Morales, D. P.; Zasadzinski, J.; Clegg, D. O.; Reich, N. O., Light-activated RNA interference in human embryonic stem cells. *Biomaterials* **2015,** *63*, 70-9.

293. Huang, X.; Pallaoro, A.; Braun, G. B.; Morales, D. P.; Ogunyankin, M. O.; Zasadzinski, J.; Reich, N. O., Modular Plasmonic Nanocarriers for Efficient and Targeted Delivery of Cancer-Therapeutic siRNA. *Nano Letters* **2014,** *14* (4), 2046-2051.

294. Huschka, R.; Barhoumi, A.; Liu, Q.; Roth, J. A.; Ji, L.; Halas, N. J., Gene silencing by gold nanoshell-mediated delivery and laser-triggered release of antisense oligonucleotide and siRNA. *ACS Nano* **2012,** *6* (9), 7681-91.

295. Chang, Y. T.; Liao, P. Y.; Sheu, H. S.; Tseng, Y. J.; Cheng, F. Y.; Yeh, C. S., Near-infrared light-responsive intracellular drug and siRNA release using au nanoensembles with oligonucleotide-capped silica shell. *Advanced materials* **2012,** *24* (25), 3309-14.

296. Yang, Y.; Yang, Y.; Xie, X.; Wang, Z.; Gong, W.; Zhang, H.; Li, Y.; Yu, F.; Li, Z.; Mei, X., Dual-modified liposomes with a two-photon-sensitive cell penetrating peptide and NGR ligand for siRNA targeting delivery. *Biomaterials* **2015,** *48*, 84-96.

297. Cueto Díaz, E. J.; Picard, S.; Chevasson, V.; Daniel, J.; Hugues, V.; Mongin, O.; Genin, E.; Blanchard-Desce, M., Cooperative Dyads for Two-Photon Uncaging. *Organic Letters* **2015,** *17* (1), 102-105.

298. Rahim, M. K. A.; Fukaminato, T.; Kamei, T.; Tamaoki, N., Dynamic Photocontrol of the Gliding Motility of a Microtubule Driven by Kinesin on a Photoisomerizable Monolayer Surface. *Langmuir* **2011,** *27* (17), 10347-10350.

299. Xue, M.; Zhong, X.; Shaposhnik, Z.; Qu, Y.; Tamanoi, F.; Duan, X.; Zink, J. I., pH-Operated Mechanized Porous Silicon Nanoparticles. *Journal of the American Chemical Society* **2011,** *133* (23), 8798-8801.

300. Wu, J.; Sailor, M. J., Chitosan Hydrogel-Capped Porous SiO2 as a pH Responsive Nano-Valve for Triggered Release of Insulin. *Advanced Functional Materials* **2009,** *19* (5), 733-741.

Résumé

Les rhabdomyosarcomes (RMS) sont les sarcomes des tissus mous les plus fréquents chez les enfants. Malgré l'amélioration des traitements multimodaux, la survie globale des populations à haut risque reste maintenue entre 5 et 20 % au cours des dernières décennies. Les traitements actuels doivent être conçus pour répondre plus spécifiquement aux besoins des patients pédiatriques, en tenant compte des différences entre enfants et adultes, et particulièrement destinés aux enfants. Pour atteindre cet objectif, nous avons développé deux nanomatériaux multifonctionnels différents et complémentaires : des nanoparticules d'organosilice mésoporeuse à base de porphyrines (PMOsPOR-NPs) et des nanoparticules de silicium poreux (pSiNPs), modifiées en greffant des molécules thérapeutiques sur leurs surfaces.

La structure particulière des PMOsPOR-NPs, avec une grande mésoporosité (5-80 nm) et un framework constituée d'agrégats J de porphyrines, permet leur chargement avec différentes molécules et leur utilisation en excitation biphotonique (TPE). Les pSiNPs ont été utilisés comme photosensibilisateurs dans la thérapie photodynamique par excitation à deux photons car ils sont capables d'absorber la lumière dans le proche infrarouge générant $^1O_2$, et en raison de leur grande surface spécifique, ils pourraient charger différentes molécules à l'intérieur de leurs pores ainsi qu'à leur surface. Nous utilisons une triple approche basée sur la combinaison de ces nanomatériaux avec des molécules de ciblage et la thérapie photodynamique ou/et la délivrance de gènes. Le ciblage actif utilisant deux molécules thérapeutiques peut avoir de multiples avantages pour la thérapie du cancer, conduisant à de nouvelles formulations permettant d'effectuer de l’imagerie, de la thérapie photodynamique par excitation à deux photons et de la délivrance de siRNA induite par TPE.

Mots-clés : Cancer pédiatrique, thérapies ciblées, nanoparticules.

Abstract

Rhabdomyosarcomas (RMS) are the most common soft tissue sarcomas of childhood. Despite intensified, multimodality treatments, the overall survival for high-risk populations has remained at 5% to 20% over the last decades. Current treatments must be designed to answer the needs of pediatric patients, taking into account the differences between kids and adults, and particularly intended for children. In order to do accomplished this goal, we have developed two different and complementary multifunctional nanomaterials, namely porphyrin-based mesoporous organosilica nanoparticles (PMOsPOR-NPs) and porous silicon nanoparticles (pSiNPs), which have been modified by grafting therapeutic molecules on their surfaces.

The particular structure of PMOsPOR-NPs, with a large mesoporosity (5-80 nm) and a framework consisting of J aggregates of porphyrins, allows their loading with different cargoes and their use in two-photon excitation (TPE). pSiNPs have been used as photosensitizer in two-photon excitation photodynamic therapy because they are capable of absorbing light in the near-infrared generating $^1O_2$, and due to their large specific surface, they could load different molecules inside their pores as well as on their surface. We use a triple approach based on the combination of these nanomaterials with targeting ligands and photodynamic therapy or/and gene delivery. The active targeting using two therapeutic molecules may have multiple benefits for cancer therapy, leading to novel formulations that have been capable of performing imaging, two-photon excitation photodynamic therapy (TPE-PDT), and TPE-induced siRNA delivery.

Keywords: Pediatric cancer, target therapies, nanoparticles.